UNIVERSITÀ DEGLI STUDI DI TRIESTE

XXXVI CICLO DEL DOTTORATO DI RICERCA IN FISICA

Quantitative material characterization in spectral X-ray computed tomography

Settore scientifico-disciplinare: **FIS-07**

DOTTORANDO / A
STEVAN VRBAŠKI

COORDINATORE
PROF. FRANCESCO LONGO Francesco Longo

SUPERVISORE DI TESI
PROF. RENATA LONGO

CO-SUPERVISORE DI TESI
Dott. Ric. ADRIANO CONTILLO

ANNO ACCADEMICO 2022/2023

Abstract

This doctoral thesis embarks on a comprehensive journey of exploring the potential of spectral X-ray imaging in medicine, employing advanced techniques and cutting-edge technologies to harness the full potential of X-ray interactions with matter. The study is divided into several chapters, each contributing to our understanding of how spectral imaging, particularly through photon-counting detectors and synchrotron radiation X-ray setups, can revolutionize medical diagnostics and material characterization. The research begins by describing the physics of X-ray interaction with matter through X-ray attenuation and phase shift. It lays the foundation for the subsequent exploration of X-ray detection methodologies, focusing on photon-counting detectors and addressing challenges like charge sharing and pulse pile-up. A central theme of this work is quantitative imaging, focusing on material decomposition as an intermediary process for computing material characteristics - material density and effective atomic number. These quantities are derived through a mathematical framework that encapsulates their connection to decomposed material maps. Innovative material decomposition techniques such as singular value material decomposition were formulated and addressed through a comprehensive theoretical framework. The concept of effective atomic number as the material property was evaluated by comparing the methods published in several papers. The exploration extends to spectral data acquisition techniques, spanning dual-energy imaging systems available on earlier-generation clinical CT scanners, multi-energy photon-counting CT scanners, and pre-clinical spectral imaging using synchrotron radiation CT systems, discussing the advantages and disadvantages of each technology. The photon-counting detectors as a state-of-the-art technology for clinical spectral imaging were addressed in the framework of a virtual imaging platform developed at Duke University. The work consisted of modeling a realistic spatio-energetic detector response including non-idealities like charge sharing and pulse pile-up. The model was validated against real measurements and special attention was focused on the influence of these non-idealities on the accuracy of spectral information, and thus the correctness of quantitative information obtained from such datasets. Besides virtual investigation, the thesis highlights the potential of the first clinical photon-counting CT scanner through the comparative assessment with dual-energy CT, demonstrating the superiority of photon-counting CT in iodine quantification at lower radiation doses. The investigation extends to synchrotron spectral CT, with a specific focus on estimating the density and effective atomic number of adipose, fibro-glandular, and cancer tissue. Synchrotron breast CT imaging was carried out at the SYRMEP beamline of Elettra, an Italian synchrotron light source in Trieste, in the framework of SYRMA-3D (SYnchrotron Radiation for MAmmography) collaboration. The research shows the potential to differentiate various breast tissues based on their quantitative characteristics and lays the groundwork for other various spectral synchrotron-based X-ray imaging setups.

Acknowledgement

I'd like to seize this moment to express my profound gratitude to several individuals who have played instrumental roles in my journey. Firstly, my heartfelt thanks go to my girlfriend, Manja, who has stood by my side from a time predating my discovery of physics as my passion. She not only supported my travels to Lithuania, Italy, and the United States in my pursuit of the frontiers of medical imaging research but also offered unwavering encouragement and love. A special acknowledgment is due to my family and dear friends, particularly my mother, Ljiljana, whose influence has profoundly shaped my curiosity and self-confidence, enabling me to persist in my work even when challenges seemed unconquerable. From a professional standpoint, I extend my sincere appreciation to my mentor, Dr Adriano Contillo. Our countless hours of discussion on the technical and scientific aspects of my work have been invaluable. His brilliant mind and caring soul have made my journey as a PhD student significantly smoother. I also wish to express my gratitude to my mentor, Prof. Renata Longo, who has been instrumental in honing my scientific reasoning and pushing me to become the best version of myself. Her unwavering support has been a cornerstone of my growth. Last but not least, I owe immense thanks to Prof. Ehsan Samei, who provided invaluable guidance and direction to my scientific curiosity. His contribution to my work is immeasurable, and I sincerely appreciate his mentorship.

Contents

Introduction

In the context of medical imaging, quantitative measurement refers to the use of numerical data and analysis to obtain information about the structure and composition of biological tissue or other materials being imaged. This approach differs from qualitative imaging, which simply provides visual information (i.e., morphology) about the appearance of the tissue or material. Quantitative measurement allows for the precise and accurate characterization of tissue properties, such as density, composition, and possibly molecular structure, which can be valuable for various medical applications, including diagnosis, treatment planning, and monitoring of disease progression. Until today, imaging modalities based on different physical interaction mechanisms, such as X-ray, ultrasound, and magnetic resonance imaging, were designed to probe, directly or indirectly, some of the tissue properties. For example, in magnetic resonance imaging (MRI), the body's hydrogen atoms are excited by the magnetic field and emit radio waves that are detected and used to generate images of the tissue. One of the main research focuses in the MRI community is developing sequences for precise and standardized measurements of tissue characteristic relaxation times T_1 and T_2 [1] for quantitative MRI (qMRI). New studies suggest that mean scan-rescan variations in measurements are 1.23 % [1], where T_2 sequences are useful for quantitatively assessing musculoskeletal tissues such as articular hyaline cartilage and muscle composition [2] while measuring T_1 time provides valuable insights for pathology detection, contrast agent uptake, iron overload, blood perfusion, and disease progression in brain imaging [3]. Ultrasound (US) imaging is mostly qualitative technique that probes the resistance of tissues to the flow of an acoustic wave and forms the signal as a difference in the acoustic impedance of tissues inside the patient. More quantitative information using US waves can be obtained with US elastography, which provides tissue stiffness or elasticity information to detect liver fibrosis, breast lesions, thyroid nodules, and prostate abnormalities [4]. Another example is Doppler-US imaging which measures the frequency shift of sound waves reflected off moving red blood cells, which is used to estimate blood flow velocity, direction, and pressure gradients. Since their discovery in 1895, X-rays have been used to produce opacity maps of the human body to visualize internal structures and detect abnormalities, revolutionizing the field of medical diagnostics and significantly improving our ability to diagnose a wide range of medical conditions and injuries. The revolution of X-ray imaging has come with Hounsfield's development of the computed tomography (CT) technique that enabled 3D volume reconstructions in 1971 [2]. The potential for quantitative imaging using X-ray interaction was realized very early, most notably in the work of Alvarez and Mackovski [5] in 1976, who theoretically elaborated how exploring

---

[1] Longitudinal relaxation time (T_1), refers to the time it takes for the hydrogen nuclei to return to their original magnetic alignment after being excited by a magnetic field. Transverse relaxation time (T_2), refers to the time it takes for the magnetic alignment of the hydrogen nuclei to lose coherence due to molecular motion and other interactions.

[2] The first successful clinical scan of a cerebral cyst patient at Atkinson Morley Hospital in Wimbledon, London, UK.

the energy dependence of X-ray-tissue interaction can be used to estimate the physical contributions to image formation such as photo-electric effect and Compton scattering. It was 30 years later that the first clinical spectral scanners reached the clinics and later provided the first iodine quantification, virtual monochromatic images, and estimation of density and effective atomic numbers based on their principles. Iodine quantification is routinely used in clinical practice as a contrast agent to enhance the visualization of blood vessels, organs, and lesions. Virtual monochromatic imaging is a post-processing technique that allows the reconstruction of CT images at a specific energy level, which is referred to as a virtual monochromatic image. In conventional CT scans, the X-ray beam contains a range of energies, resulting in polyenergetic images. Virtual monochromatic imaging aims to simulate what an image would look like if it were generated using a single energy X-ray beam. Virtual monochromatic images are beneficial in a wide range of clinical applications, including bone imaging, metal artifact reduction, and better visualization of iodine contrast in blood vessels. In this thesis, we aim to push the boundaries of traditional CT imaging by leveraging spectral information to quantitatively assess tissue properties like density and effective atomic number. While some clinical scanners can provide such data, the associated algorithms are still in their early stages, often lacking accuracy for broad clinical use and leaving untapped potential. This thesis explores hardware and algorithmic aspects of tissue characterization through spectral CT, and it presents both clinical and preclinical findings using cutting-edge technology. More broadly, this thesis contributes to efforts to make medical imaging more objective and standardized, improving early detection, enabling cross-comparison, and consistent tracking of disease progression and treatment response.

The research performed in this thesis will be structured into several chapters as follows:

1. In the opening chapter, we will begin by examining the physics of X-ray interactions with matter, shedding light on the effects of these interactions, such as X-ray attenuation and phase shift. Next, our attention will shift to the technology behind detectors and the methods used to capture signal variations caused by objects. Finally, we'll wrap up the chapter by delving into the principles of computed tomography and the technical approaches for extracting three-dimensional data from a series of projection measurements. Although technical, this chapter is an overview of common knowledge in the X-ray imaging community and will serve as a basis for a more advanced approach to X-ray imaging.

2. In the upcoming second chapter, we will explore the notion of quantitative imaging. Our primary focus will be on material decomposition, a fundamental aspect of clinical quantitative imaging that serves as the basis for deriving other quantitative material maps. We will introduce the novel solutions for material decomposition researched and developed in this thesis project, offering comprehensive theoretical explanations. Additionally, we will delve into the idea of the effective

atomic number, and provide a mathematical framework for calculating material density and effective atomic number values based on the material decomposition process. It will become clear that spectral measurements are essential [3] for material decomposition in clinical scanners.

3. The third chapter will focus on technical solutions for spectral data acquisition, such as dual or multi-energy imaging systems. The spectral separation can be source-based and detector-based, or a combination of the two, and we will discuss some of the commercially available methods. The state-of-the-art photon-counting CT and synchrotron radiation CT to exploit phase-contrast benefits will be introduced in more detail as results presented in this thesis were obtained using such technology.

4. Next chapter will dive into a virtual (in-silico) framework for the realistic modeling of CT scanners. We will discuss detector modeling as an important part of virtual simulation. The focus will be on modeling photon-counting detectors in terms of spatial-energetic response including noise model and all of the non-idealities such as charge sharing and pulse pileup effect. Validation of the model against physical measurements will be presented and we will show how virtual study can aid the development of state-of-the-art photon-counting detectors.

5. The fifth chapter contains results obtained from a first-ever clinical photon-counting CT model produced by Siemens Healthineers and installed at Duke Health clinic in Durham, NC, USA. In particular, we compared the performance of dual-energy SOMATOM Force and NAEOTOM Alpha photon-counting CT scanners in generating more quantitative information from obtained spectral measurements, such as iodine quantification and virtual monochromatic imaging (VMI).

6. In the sixth chapter an experimental work toward spectral imaging using synchrotron CT at SYRMEP beamline at the Italian national synchrotron facility in Trieste, Elettra Sincrotrone Trieste will be presented. The work will specifically focus on breast imaging, with the goal of extracting tissue density and effective atomic number to better differentiate soft tissues within the breast and cancer tissue.

7. In the final chapter, the potential for optimization of spectral synchrotron breast CT will be explored. This work is particularly valuable for a transition of synchrotron spectral imaging in clinical practice where radiation dose and efficiency play crucial roles.

---

[3] Simultaneous measurements of attenuation and phase at single energy can also be used to perform material decomposition (see [6]), but technical solutions are not yet available for clinical practice and won't be discussed in this thesis.

1 Physics of X-ray interaction and detection in tomography

1.1 X-ray attenuation and phase shift in matter

X-ray interaction with matter is governed by the intricate principles of physics that operate on the atomic scale. However, when it comes to the practical application of X-rays in medical imaging, the focus shifts from the individual atoms to the local averaged response of matter as a whole. Starting from the microscopic scale, when diagnostic X-rays interact with an atom, they are scattered by bound electrons. The amplitude of X-ray scattering caused by a single atom is called the atomic form factor. The atomic form factor is a function of a scattering vector $q(r)$ as given in equation 1.

$$f(q, \hbar\omega) = f_0(q) + f'(q, \hbar\omega) + if''(q, \hbar\omega) \tag{1}$$

The first term

$$f_0(q) = \int \rho_e(r) e^{iq \cdot r} d^3 r = \begin{cases} Z, & |q| \to 0 \\ 0, & |q| \to \infty \end{cases} \tag{2}$$

of equation 1 represents the Fourier transform of the electron density distribution ρ_e of the atom. Notably, for forward scattering ($q \to 0$), $f_0(q)$ approaches atomic number Z for nonionized atoms or $Z - I$ for ions with ionization state I [7]. The real and imaginary corrections, f' and f'', respectively, depend not only on q but also on $\hbar\omega$, capturing the resonance properties of atomic orbitals, particularly at absorption edges where the magnitude is maximum. The real part of the atomic scattering factor f' describes the dispersion or phase shift of the scattered radiation due to the interaction of the X-rays with the electrons. The imaginary part f'' accounts for the absorption of the radiation by the electrons. Form factors are tabulated in international databases which are used for wide-angle diffraction experiments such as crystallography. However, for forward-directed beam propagation and small angle diffraction conditions which are met in medical X-ray imaging, the optics are insensitive to the interatomic distances, and matter is probed only in the form of its local averaged response. On the macroscopic scale, X-ray interaction with matter is described by the refractive index n defined as a complex quantity:

$$n = 1 - (\delta - i\beta) \tag{3}$$

Thus, the X-ray index of refraction is a continuous property of matter, rooted in atomic properties such as elastic scattering of bound electrons within the medium. The imaginary part f'' accounts for the absorption of the radiation by the electrons. The dispersion term δ of the X-ray refractive index is related to the atomic form factor and the number density of atoms ρ_a (atoms per volume) as:

$$\delta = \frac{r_0\lambda^2}{4\pi}\rho_a(r)[Z + f'(\omega)] \tag{4}$$

Here, $r_0 = 2.82 \times 10^{-15}$ m is the Thomson scattering length, and $f'(\omega)$ is the real part of the atomic form factor. Using relation $\rho_a = \rho\frac{N_A}{A}$ and assuming the condition where X-ray energy is far above any absorption edges of biological tissues (dominated by light elements C, H, O, N, S, P), the equation can be approximated as:

$$\delta \simeq \frac{r_0\lambda^2 N_A}{2\pi A}\rho \tag{5}$$

where ρ is mass density and N$_A$ is an Avogardo number, because A $\approx 2Z$. Similarly, the imaginary component β of the index of refraction is given by:

$$\beta = \frac{r_0\lambda^2}{2\pi}\rho_a(r)f''(\omega) \tag{6}$$

As an X-ray described as a plane wave e^{ikL} with a wavenumber $k = \frac{2\pi}{\lambda}$ transitions to a homogeneous medium with index n, the transmitted plane wave $e^{ikL(1-\delta+i\beta)}$ undergoes changes in amplitude and phase as given in equation 7

$$e^{ikL(1-\delta+i\beta)} = e^{ikL}\, e^{-ik\delta L}\, e^{-k\beta L}\,, \tag{7}$$

where the phase retardation $\Delta\phi$, proportional to the material's traversed length L and δ, is expressed as $e^{-ik\delta L} \equiv e^{-i\Delta\phi}$. The decrease in amplitude is governed by the factor $e^{-k\beta L}$, leading to an intensity decrease given by:

$$I/I_0 = |e^{-k\beta L}|^2 = e^{-2k\beta L} = e^{-\mu L} \tag{8}$$

This equation establishes the relationship between the linear attenuation coefficient μ and β as:

$$\beta = \frac{\mu}{2k} = \frac{\mu\lambda}{4\pi}. \tag{9}$$

The wavelength of diagnostic X-rays varies roughly from 0.1 nm to 0.01 nm, roughly corresponding to an energy range from below 20 keV to about 150 keV. Although X-rays with a much shorter wavelength are highly penetrating, they provide little low-contrast information and therefore are of little interest to diagnostic imaging [8]. For soft tissues, the dissimilarity in β is most pronounced within the lower energy X-rays (below 40 keV), but, the significant absorption of low-energy X-rays within the human body imposes limitations on signal-to-noise ratios requiring increased radiation doses. Consequently, higher average X-ray energies are used in clinical imaging, hampering the capacity to discern small attenuation differences between soft tissues. The differences between soft tissues are better observed by measuring the phase perturbations by an object, but the acquisition setups required to detect this change using a conventional X-ray source are far more complicated and have not yet been implemented in clinical practice. We will discuss the application of synchrotron X-ray imaging which provides sufficient characteristics of the beam for measuring phase contrast in section 3.3.

1.2 X-ray detection in medicine

Most clinical X-ray machines use tubes that produce continuous spectrum and energy-integrating detectors. As a result, the opacity maps obtained this way are a weighted average of X-ray spectral shape and detector response curve. Energy-integrating detectors in medical imaging operate based on the principle of integrating the total energy of incident X-ray photons [9]. The detector bulk typically consists of a scintillator that converts X-rays into visible light, which is then captured by a photodetector. The scintillator emits light in proportion to the energy of the incoming X-rays. A photodetector, often a photodiode or photomultiplier tube, then converts this light into an electrical signal. These types of detectors are referred to as indirect conversion detectors. Direct conversion detectors mostly consist of an amorphous selenium-based sensor that directly converts X-rays to charge. Independently of signal generation, the energy-integrating detector systems integrate the electrical signal over a certain time period, effectively summing up the energy of all the X-ray photons that strike the detector during that interval. The resulting signal is proportional to the total energy deposited in the sensor and is used to create a grayscale image, with pixel intensities representing the radiation dose received at each point in the imaged object. Since higher-energy photons deposit more energy and generate a stronger signal, they contribute more to the integrated signal. It is to say, energy-integrating detectors weigh more X-rays of higher energy which carry less contrast information compared to low-energy X-ray photons. In the aftermath of the detection process, measured signals between tissues are very similar except for the case of very different tissues or administered contrast agents, and differentiation between soft tissues becomes a very difficult task.

1.2.1 Photon-counting detectors

Photon-counting detectors (PCDs) operate inherently differently from energy-integrating detectors. Instead of integrating multiple X-rays arriving at the detector in a given time frame, in photon-counting detectors each photon is counted as soon as it creates enough electrical signal to surpass the predetermined threshold. Thus, photon-counting detectors alleviate the problem of the elevated contribution of high-energy X-rays existing in energy-integrating detectors and provide a more uniform detector energy response by counting photons one by one. The energy threshold can be placed at a desired energy level by adjusting the pre-determined voltage. Targeting the energy range just above the region where electronic noise dominates over the signal removes the electronic noise [9]. Due to the direct conversion of X-rays to electric signals that eliminates the need for a scattering scintillation layer often used in energy-integrating detectors, the cross-talk between adjacent pixels in PCDs can be reduced, allowing for smaller pixel sizes and improved resolution. Noise cancellation and smaller pixel sizes are two other big advantages of PCDs over energy-integrating detectors. The scheme of a photon-counting detector system shown in Fig. 1 comprises several key components that work collaboratively to detect and quantify incident photons. The scheme describes Application Specific Integrated Circuit (ASIC) which performs signal collection and processing [10].

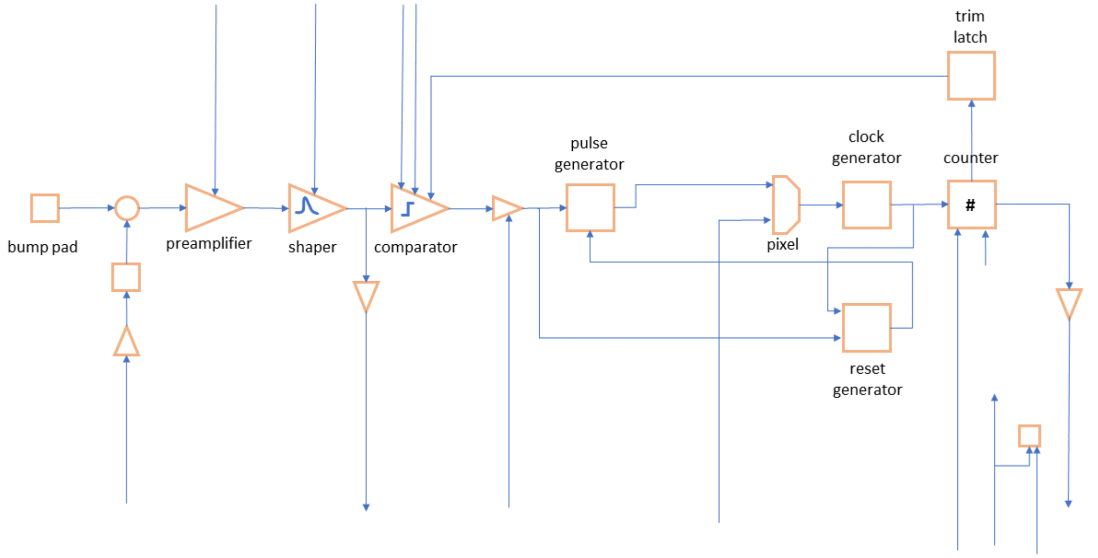

Figure 1: The photon-counting detector ASIC's analog component includes a preamplifier that amplifies the charge signal generated by an X-ray and gathered via a bump pad. It also incorporates a shaper to adjust the signal's waveform, as well as a comparator. Following the analog stage, the signal undergoes digitalization through a pulse generator, a clock, a reset generator, and a digital counter.

The system begins with a sensor usually made of Cadmium-Telluride (CdTe) or similarly Cadmium-Zinc-Telluride (CdZnTe) (sometimes thick Silicon (Si) as well) which converts incident photons into measurable electrical signals. High-Z semiconductors are usually preferable due to excellent detection efficiency even with thin sensors, which is of paramount importance for medical imaging where the radiation dose is always kept as low as possible. The weak electrical signal generated by charge collection from the sensor bulk is collected to pixel electronics through a bump pad and amplified by a pre-amplifier. The bias voltage applied over the detector bulk creates an electric field that has to be strong enough to collect charges before they drift from the center of interaction, but at the same time, it can't be very strong so that charges create secondary particles due to the acceleration by the field and spoil proportionality between deposited energy and electric signal. The drift of the charges away from the area covered by a single pixel results in charge collection by surrounding pixels in the phenomena known as charge sharing. Pre-amplifier proportionally amplifies the signal to enhance the signal-to-noise ratio and prepare the signal for further processing. The amplified signal is then fed into a shaping amplifier. The shaping amplifier conditions the signal by modifying its pulse shape, typically transforming the sharp, short signal pulse from the pre-amplifier into a Gaussian-shaped pulse. This shaping process further optimizes the signal-to-noise ratio and prepares the signal for digitization. The shaped signal is compared to one or more predetermined threshold levels in a threshold comparator. The threshold comparator categorizes the pulses into two groups: those below the threshold (rejected) and those above the threshold (accepted). This step helps filter out the noise and unwanted signals, and also inherently encodes spectral information about the object. The number of spectral channels in photon-counting detectors thus depends on the number of threshold comparators attached to each detector pixel. The advantages of inherent spectral separation of signal through energy thresholds will be discussed in section 3.2. The comparator ends the analog part of signal processing and the signal enters the digital part of the counting circuit. The pulse generator detects edges of a predetermined polarity at its input and generates a signal pulse of a predetermined width at its output whenever an active edge occurs. Subsequently, the clock generator provides regular and synchronized signals to the input of the counter in order to register one count per signal. The reset generator communicates with the pulse and clock generator and resets the pulse generator once both, the pulse generator input signal and the clock generator output signals have ended after the registration of a count. This type of counting circuit is called paralyzable because counting is triggered by the active edges at the input of the pulse generator and in case no edges occur, the pulse generator remains locked. Edges won't occur in conditions of high photon flux, where during the predetermined pulse width set by the pulse generator other photons are arriving and keeping photon-detection generated voltage higher than the edge voltage set on the comparator for a given threshold. In such a condition, the circuit is kept in the loop of waiting for the signal to drop below the predetermined edge so that the count can be registered. What happens is that the circuit registers two or more photons as one photon of the higher energy, losing the spectral information, and worsening the signal-to-noise ratio (SNR) and contrast-to-noise ratio (CNR). In case photon flux is low, there is a low probability that two or more photons will hit the same detector pixel during the predetermined time set on the pulse generator. In this case, the detector can count photons one by one, correctly separating them into different energy thresholds. The effect in which two or more photons impinging the same detector pixel are processed as a single event, leading to counting loss and spectral distortion of the signal is called pulse pileup. Pulse pileup effect and charge sharing effects as one of the main limitations of photon-counting detectors will be discussed in the following sections.

1.2.2 Charge sharing

When a photon interacts with the detector, it generates electron-hole pairs within the semiconductor bulk. In photon-counting detectors, each interaction is ideally registered as a separate event within a single detector element. However, charge sharing can occur due to the finite size of the detector elements and the spread of charge carriers during their drift toward the readout electrodes. If the photon interaction point is near the boundary between two adjacent detector pixels, the generated charge can be shared between them. Fig. 2 illustrates the charge-sharing phenomena. This results in a single photon being detected as two or more simultaneous events, affecting the accuracy of both spatial and spectral measurements. Spectral information is corrupted because the information from one single photon is registered by the detector as if it was created by two or more photons of lower energy. From this, we can see that charge-sharing effects limit the pixel size of photon-counting detectors, and in case pixel size is comparable to the mean free path of created charge in sensor bulk, some form of charge-sharing correction needs to be applied.

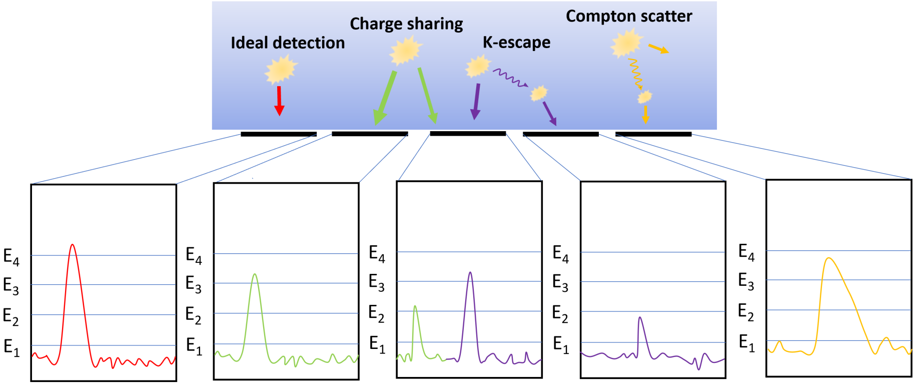

Figure 2: Interaction mechanisms occurring in high-Z sensors leading to an incorrect spectral energy response of photon-counting detectors. An ideal detection of a signal is given for reference.

The high-Z sensors can be as thin as 1.5 mm because of the large interaction cross-section for diagnostic X-rays but they are limited by the fluorescence effects. Fluorescence is a process by which incoming X-ray photons interact with the sensor material and create secondary X-ray photons of lower energy. These secondary X-ray photons, which mainly result from X-ray interaction with electrons sitting in the K shell, interfere with the accurate detection and measurement of the original X-ray photons, leading to distortion in the spectral response and decreased image quality. Fluorescence introduces K-escape peaks at the original energy minus the fluorescence energy in the detector energy response. They are called escape peaks as they occur when a fluorescence photon leaves (escapes) the pixel area of primary detection and is detected in another pixel. The fluorescence photons and ”original minus fluorescence” photons illustrated in Fig. 2 can have energies that overlap with the energies of the incident X-ray photons, leading to confusion in distinguishing them from the original X-ray photons. As such they contribute to the measured X-ray spectrum, altering the apparent energy distribution of the incoming X-rays. This effect is particularly important for CdTe sensors where the K shell ($E_{K\ (Cd)} = 26.7$ keV and telluride $E_{K\ (Te)} = 31.8$ keV) occurs in the energy range of the interest. Silicon K-edge is very low (1.84 keV), outside of the energy range used in diagnostic radiology, so fluorescence effects do not have an influence on detector energy response. However, Si sensors exhibit a significant fraction of Compton interactions at low energies and must be thick for good detection efficiency.

1.2.3 Pulse pile up

In the realm of X-ray imaging, and nuclear and particle detection, the pulse pileup effect is a critical phenomenon that arises when the incoming radiation events occur in rapid succession, leading to a distorted output signal due to the inability of the detection system to resolve individual pulses. This phenomenon becomes particularly significant at high count rates and can introduce distortions in both the amplitude and timing of detected signals. Pulse pileup manifests as count loss, where several lower energy photons are processed together and registered as one higher energy photon. The pulse shape produced at the shaper can be described with an asymmetric Gaussian-like function which can also contain a negative tail representing signal recovery time to the base level. The two realistic pulse shapes are given in Fig. 3.

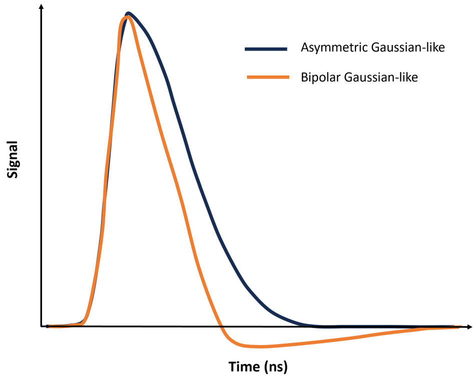

Figure 3: An asymmetric Gaussian-like shape (blue) and bipolar pulse shape (orange) signals produced by shaper electronics in PCD ASIC.

The undershoot tail of the preceding pulse can overlap with the peak of the next pulse leading to tail pulse pileup effects and reducing the effective height of the recorded pulse. Since the tail time duration is usually longer than the peak time duration, statistically, there is a higher probability of a tail pulse pile-up effect. More detail on the bipolar pulse pileup is given in [11]. One of the major challenges to the application of photon-counting detectors to medical CT imaging was the inability of technology to meet the high demands of medical CT in terms of photon flux. The high flux is needed to reduce motion artifacts and scanning times in a clinical environment and photon fluxes in clinical CT can reach up to 10^9 counts $\mathrm{mm}^{-2}\mathrm{s}^{-1}$, imposing significant challenges on the counting speed of photon-counting detectors.

Paralyzable and non-paralyzable detectors are two distinct classes of detectors commonly used to address the challenges posed by the pulse pileup effect. Non-paralyzable detectors are characterized by a pre-determined, hard-coded dead time during which the detector pixel is unresponsive to incoming signals after detecting an event. This inherent dead time allows a non-paralyzable detector to process a single event before the next event is registered. It helps to distinguish between closely spaced events and reduce the impact of pulse pileup. The dead time is selected such that the signal induced by the longest input pulses drops below the lowest energy threshold at the end of the dead time. This approach avoids double counting of a single pulse which would occur by splitting long pulses generated by high-energy X-rays. Paralyzable detectors, on the other hand, lack this recovery time and can register events in rapid succession even if the signal is not processed. Once the voltage generated by the charge cloud reaches a programmable reference voltage supplied to the comparator, the counter is increased for one unit and the paralyzable detector waits for this voltage to drop below the reference voltage. This time is also called dead time since it is the time needed for a signal to drop below a given threshold and enable new detection. The advantage of paralyzable detectors is that deadtime length is signal-dependent and doesn't need to be programmed in advance. In case X-rays of significantly different energies reach the detector, it will take an appropriately shorter time to process X-rays of lower energy and a longer time to process high-energy X-rays. In applications with fluctuating event rates, paralyzable detectors might provide more accurate data by dynamically adjusting their responsiveness based on the event rate at any given time. However, in case of high photon flux, it happens that photons arrive quickly, keeping the voltage on the comparator above the reference voltage for a prolonged period of time. In such a condition, the detector is paralyzed and counts several events as a single event. Under exposure to high photon flux, they are more susceptible to the pulse pileup effect and have a shorter linearity range than that of non-paralyzable. It has been demonstrated that for medical applications, non-paralyzed detectors provide a more accurate spectral response.

Recently, hybrid approaches to X-ray detection have been developed [12, 13]. The "instant-retrigger" technology developed by DECTRIS Ltd. [12] is a hardware-based counting solution designed to improve paralyzable detectors in high-flux conditions. It addresses the pulse pile-up challenge through the implementation of a mechanism to restart counting after an adjustable time period, allowing the detector to operate in a specific non-paralyzable counting mode. Specifically, following a predetermined retrigger time period subsequent to the registration of a count, the counting mechanism within the individual pixels is reactivated. This involves a reassessment of the amplified signal and the re-enabling of the pixel for counting in accordance with the signal's characteristics. After the expiration of the retrigger time interval, a pixel will add one more count if the amplified signal at the discriminator input continues to surpass the predefined threshold level. Notably, the retrigger time interval is customizable and can be generated through circuitry within each pixel. The initiation of the retrigger time interval sequence precisely coincides with the initial surpassing of the threshold level by the amplified signal. The width of the retrigger time can be configured to be shorter, equal to, or longer than the nominal single photon pulse width at either the discriminator input or output. In this context, the nominal single photon pulse signifies the pulse generated by a single incident photon based on the effective processing parameters. A comparison between paralyzable, typical non-paralyzable and specific non-paralyzable (instant-retrigger) modes of signal processing is given in Fig. 4. In conditions where several waveforms are overlapping, a non-paralyzable detector provides a more accurate number

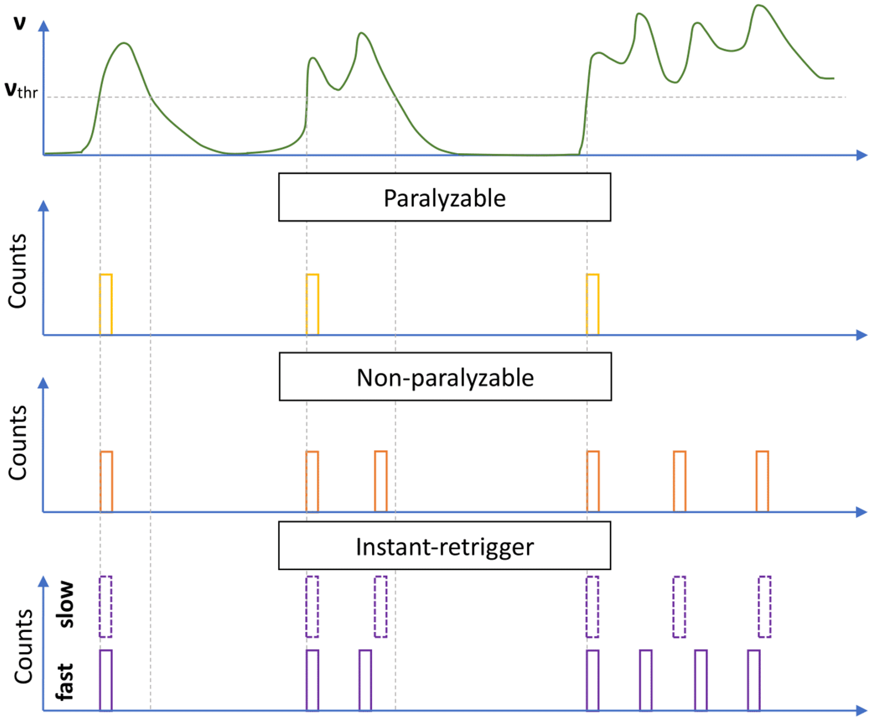

Figure 4: Illustration of paralyzable, non-paralyzable, and instant-retrigger counting mechanisms depending on the incoming signal in high flux conditions.

of counts for a given energy threshold than a paralyzable detector. Instant retrigger technology causes similar behavior to non-paralyzable detector design except retrigger times can be adjusted to provide more accurate counting in high-order pulse pileup - indicated by fast instant retrigger output.

1.3 Computed tomography

Computed tomography (CT) is an imaging technique that uses X-rays and computer processing to produce cross-sectional images of the object's internal structure. In a nutshell, it is a procedure of acquiring a large number of low-dose 2-dimensional (2D) views (projections) of an object from different angles and a follow-up reconstruction procedure to reconstruct the 3-dimensional (3D) structure of the object. The projections contain integrated μ coefficients that can be obtained from equation 8 through the process of flat field correction as:

$$-log(I/I_0) = \int \mu(l)dl \tag{10}$$

where I represents a projection containing a sample and I_0 is air projection. Reconstructing an image from its projections involves a mathematical operation known as the filtered backprojection, although other more robust techniques are being constantly developed. The size of a 2D projection is determined by the number of detector rows in the z direction and the detector columns in the x direction. In situations where a parallel beam geometry is used, each row of a detector provides a 1D projection of a 2D slice $f(x, y)$ of a 3D object $f(x, y, z)$ at a particular z position, so that reconstruction of the 2D object distribution $f(x, y)$ can be treated as an independent problem. The theory that describes the process of reconstruction is called the Fourier slice theorem (FST) and it states that: The Fourier transform of a parallel projection $p(s, \theta)$ of an object $f(x, y)$ acquired at an angle θ equals a line in a 2D Fourier transform of $f(x, y)$ taken at the same angle [8]. The FST simplifies the reconstruction process by connecting the projection data to the Fourier domain, reducing the 2D reconstruction problem to a series of 1D problems. For reconstructing the last dimension z of an object $f(x, y, z)$ using parallel beam geometry, the 2D reconstruction process is performed multiple times, until the entire z dimension is accounted for. Filtered backprojection is an implementation of FST to reconstruct tomographic CT images. To give a straightforward proof of the previous statement, a projection $p(x, \theta = 0)$ of a human chest phantom is obtained at angle $\theta = 0$ in parallel beam geometry and both 2D Fourier transformation and projection following 1D Fourier transformation were obtained. The result of the procedure is given in Fig. 5 and present formal derivation by relating the projection $p(x, \theta = 0)$ with the original object $f(x, y)$ as:

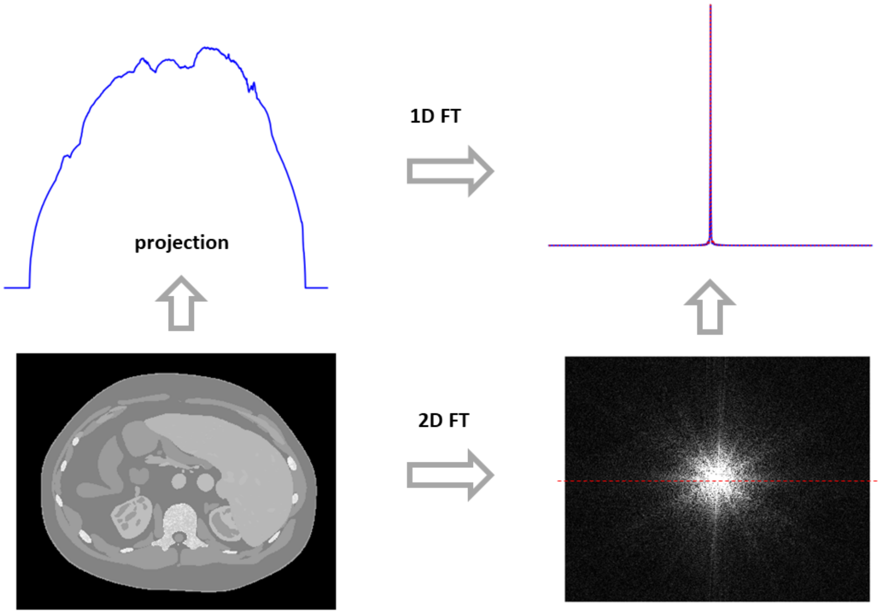

Figure 5: Graphical representation of the Fourier slice theorem used for deriving the concept of image reconstruction in computed tomography.

$$p(x,0) = \int_{-\infty}^{\infty} f(x,y)dy \tag{11}$$

Performing 1D Fourier transformation of projection with respect to x considering the equation 11

$$FT(u) = \int_{-\infty}^{\infty} p(x,0)e^{-2\pi iux}dx = \int_{-\infty}^{\infty}\int_{-\infty}^{\infty} f(x,y)e^{-2\pi iux}dxdy \tag{12}$$

and on the other hand, 2D Fourier transformation with respect to both x and y of object f(x,y) evaluated at $\nu = 0$

$$FT(u,\nu) = \int_{-\infty}^{\infty}\int_{-\infty}^{\infty} f(x,y)e^{-2\pi i(ux+\nu y)}dxdy = \int_{-\infty}^{\infty}\int_{-\infty}^{\infty} f(x,y)e^{-2\pi iux}dxdy \tag{13}$$

the proof is obtained by equating the right-hand sides of equations 12 and 13. From Fig. 5 one can see that if we collect a sufficient number of projections over the range from 0 to π, we can fill the entire Fourier space with a set of 1D Fourier transforms of acquired projections. The tomographic reconstruction can be simply obtained following an inverse path: from Fourier space using inverse 2D Fourier transformation. The procedure can be extended to the last dimension to perform reconstructions at different heights of an object. Although straightforward, the reconstruction technique utilizing Fourier space lacks robustness in practical application. One of the challenges lies in the non-Cartesian sampling pattern it produces in Fourier space. To perform a 2D inverse operation the interpolation or regridding of data must be performed, introducing the errors in the frequency domain that can have a broad impact on the entire image in the spatial domain. The inverse form of 2D forward Fourier transform given in equation 13 is:

$$f(x,y)=\int_{-\infty}^{\infty}\int_{-\infty}^{\infty}FT(u,\nu)e^{2\pi i(ux+\nu y)}dud\nu \tag{14}$$

To express quantity $FT(u,\nu)$ in the form in which data is collected, we switch the coordinate systems using $u=\omega\cos\theta$ and $\nu=\omega\sin\theta$ and $dud\nu=\omega d\omega d\theta$. In the changed reference frame equation 14 becomes:

$$f(x,y)=\int_{0}^{2\pi}d\theta\int_{0}^{\infty}FT(\omega\cos\theta,\omega\sin\theta)e^{2\pi i\omega(x\cos\theta+y\sin\theta)}\omega d\omega \tag{15}$$

Using the FST, $FT(\omega\cos\theta,\omega\sin\theta)$ can be replaced by P(ω,θ), leading to following relationship:

$$\begin{aligned}f(x,y)&=\int_{0}^{2\pi}d\theta\int_{0}^{\infty}P(\omega,\theta)e^{2\pi i\omega(x\cos\theta+y\sin\theta)}\omega d\omega\\&=\int_{0}^{\pi}d\theta\int_{0}^{\infty}P(\omega,\theta)e^{2\pi i\omega(x\cos\theta+y\sin\theta)}\omega d\omega+\int_{0}^{\pi}d\theta\int_{0}^{\infty}P(\omega+\pi,\theta)e^{-2\pi i\omega(x\cos\theta+y\sin\theta)}\omega d\omega\end{aligned} \tag{16}$$

For parallel beam geometry $p(s,\theta+\pi)=p(-s,\theta)$ symmetry holds as projections from the two exactly opposite sides of the object are the same. In Fourier space, this translates to $P(\omega,\theta+\pi)=P(-\omega,\theta)$ and allows rewriting the equation 16 as:

$$f(x,y)=\int_{0}^{\pi}d\theta\int_{-\infty}^{\infty}P(\omega,\theta)|\omega|e^{2\pi i\omega(x\cos\theta+y\sin\theta)}d\omega \tag{17}$$

.

Finally, switching back to the rotated coordinate system, we obtain:

$$f(x,y)=\int_{0}^{\pi}d\theta\int_{-\infty}^{\infty}P(\omega,\theta)|\omega|e^{2\pi i\omega x}d\omega \tag{18}$$

where $P(\omega,\theta)$ is 1D Fourier transformation of projection $p(x,\theta)$ at angle θ and the inside integral $\int_{-\infty}^{\infty}P(\omega,\theta)|\omega|e^{2\pi i\omega x}d\omega$ is the inverse Fourier transform of $P(\omega,\theta)|\omega|$. It is called filtered projection because, in the spatial domain, it represents a projection that is filtered by a function whose frequency domain is $|\omega|$. In the spatial domain, the corresponding function $\xi(x)$ to the filter $|\omega|$ is the inverse Fourier transform of the function:

$$\xi(x)=\int_{-\infty}^{\infty}|\omega|e^{2\pi i\omega x}d\omega \tag{19}$$

When choosing x = 0, $\xi(0)$ represents area under the curve $|\omega|$, and when $|\omega| \to \infty$ also $\xi(0) \to \infty$. Thus, to be able to solve equation 18, one introduces a band-limited filter H(ω) to limit high spatial frequency contribution to the reconstruction, leading to the equation 20:

$$f(x, y) = \int_0^\pi d\theta \int_{-\infty}^{\infty} P(\omega, \theta)|\omega|H(\omega)e^{2\pi i\omega x} d\omega \tag{20}$$

.

The equation 20 cannot be directly implemented in its present form, as Fourier inversion of filter $|\omega|$ doesn't exist. The solution is to assume that Fourier transform is band-limited as

$$g(t, \theta) = \int_{-\Gamma}^{\Gamma} P(\omega, \theta)|\omega|e^{2\pi i\omega x} d\omega \,. \tag{21}$$

This means that all energy is contained inside the interval $(-\Gamma, \Gamma)$. In order to ensure a sampling process devoid of aliasing artifacts, it is imperative that the projection bandwidth Γ adheres to the Nyquist sampling criterion, which is expressed as:

$$\Gamma = \frac{1}{2\delta} \text{ cycles/mm} \,,$$

where δ represents the projection sampling interval, measured in millimeters. Under these sampling conditions, it becomes necessary to introduce a window function $q(\omega)$ to modulate the original ramp function $|\omega|$.

$$H_q(\omega) = |\omega|q(\omega) \,.$$

The window function is defined as:

$$q(\omega) = \begin{cases} \omega, & \text{for } |\omega| < \Gamma \\ 0, & \text{otherwise} \end{cases}$$

The difference between an ideal and band-limited ramp filter is given in Fig. 6.

Reconstructed data is typically expressed in Hounsfield units (HU), named after Sir Godfrey Hounsfield, the inventor of the CT scanner:

$$HU = \frac{\mu - \mu_{\text{water}}}{\mu_{\text{water}}} \times 1000 \tag{22}$$

where μ is the linear attenuation coefficient of the material being measured and μ_{water} is the linear attenuation coefficient of water. Hounsfield units measure radiodensity within the human body; on

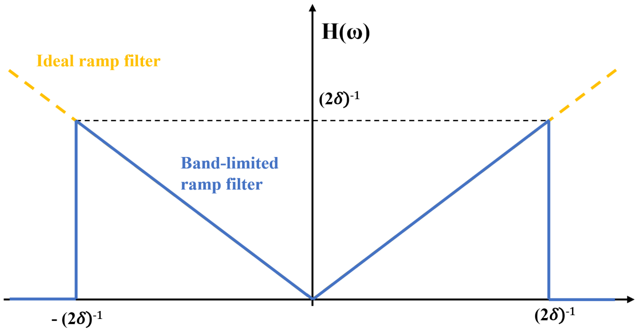

Figure 6: Band-limited ramp filter in the frequency domain.

this scale, water is assigned a value of 0 HU, and other materials are measured relative to water. For example, air has a negative HU value, while dense materials like bone have positive HU values.

2 Quantitative computer tomography

The linear attenuation coefficient of tissues in the human body is very similar within the diagnostic energy range, as shown in Fig. 7.

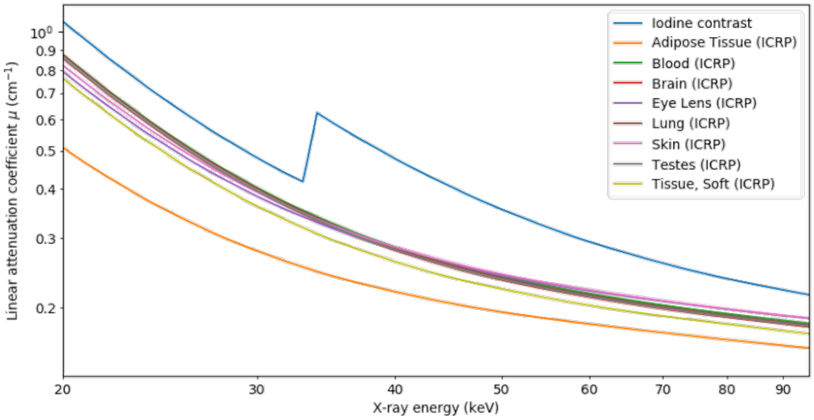

Figure 7: The log-log plot of linear attenuation coefficients of different human tissue and iodine contrast.

The early work of Alvarez and Makovski [5] addressed the limited ability of conventional X-ray imaging to distinguish similar soft tissues. They opened a whole new field dedicated to improved tissue differentiation and quantitative description: spectral X-ray imaging. The primary principle underlying spectral imaging is the capture and analysis of the energy-dependent linear attenuation coefficient $\mu(E)$ within the diagnostic X-ray energy range. Spectral information can be used to estimate the ratio of two dominant contributions to image formation - photoelectric (PE) and Compton effect (CE). Hence, two maps of competing physical contributions, one proportional to PE and the other to CE, are produced with this procedure. Because their functional dependence is empirically related to material density ρ and the effective atomic number Z_{eff}, such decomposition procedure leads to an opportunity for tissue separation based on their quantitative features. Instead of decomposing spectral data in PE/CE space, a more popular approach is representing the content of each voxel as a combination of two known materials. This process is known as material decomposition and represents a cornerstone of clinical spectral CT imaging. In the material decomposition approach, the attenuation coefficient μ of a given material is expressed as a linear combination of the (known) attenuation coefficients of a pair of basis materials, here labeled μ_1 and μ_2

$$\mu = x_1\,\mu_1 + x_2\,\mu_2 \tag{23}$$

where x_1 and x_2 are the coordinates of the material in the reference frame identified by the selected basis. It is used to produce a range of clinical tasks such as iodine quantification, calcium scoring, virtual monochromatic imaging, or density and Z_{eff} maps. Iodine solutions are the most common contrast agent used in medical imaging due to their high atomic number and excellent X-ray attenuation properties, which make them ideal for enhancing the visibility of blood vessels, organs, and other structures. The notable difference in attenuation is shown in Fig. 7. Section 2 is dedicated to a detailed explanation of the material decomposition approach focusing on the contribution of this thesis to the field. The following section 2.2 deepens our understanding of the concept of effective atomic number and provides a mathematical recipe to obtain density and Z_{eff} maps from the material basis set.

2.1 Material decomposition

Until now, many decomposition methods have been developed, and some have been clinically implemented. Among existing approaches, material decomposition could be applied to sinogram space or already reconstructed images. A sinogram is a set of line projections (as one shown in Fig. 5) obtained from different angles θ around the object organized in a matrix form of a size number of projection × number of detector pixels in the horizontal direction. In parallel beam geometry, the reconstruction of one sinogram leads to a single scan slice and the number of slices corresponds to the number of vertical pixels in the detector selected for image reconstruction. The comparison between the raw data domain (sinogram domain) versus image domain material decomposition is illustrated in Fig. 8.

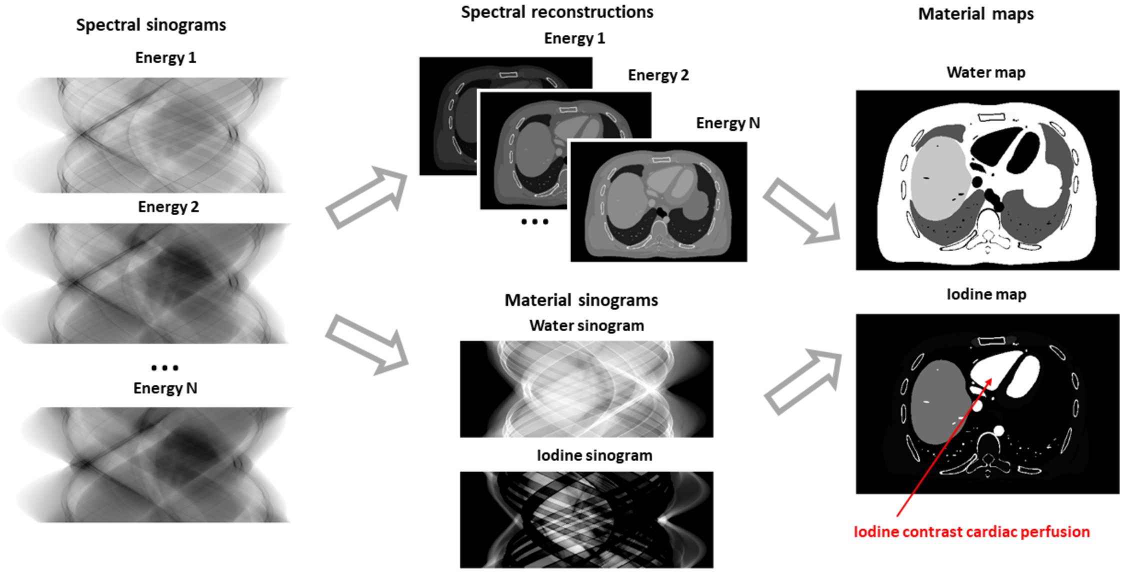

Figure 8: The two most common approaches to material decomposition in clinical CT scanners. In the first case, spectral sinograms are first reconstructed using the procedure described in section 1.3, and material decomposition is applied in reconstructed (tomogram) space, while in the second case, material decomposition is applied in the sinogram space prior to image reconstruction.

The straightforward image-based method can be obtained by rewriting the equation 23 in a matrix form as:

$$\vec{\mu} = A\vec{x} \tag{24}$$

where the 3D material maps $\vec{x}$ are obtained through inversion of linear map A. The $\vec{x}$ and $\vec{\mu}$ are of size 2 × (number of pixels) in an image. More explicitly, equation 24 is given as:

$$\begin{bmatrix} \mu_H \\ \mu_L \end{bmatrix} = \begin{bmatrix} \mu_{1H}\, I & \mu_{2H}\, I \\ \mu_{1L}\, I & \mu_{2L}\, I \end{bmatrix} \begin{bmatrix} x_1 \\ x_2 \end{bmatrix} \tag{25}$$

where I is an identity matrix of size (number of pixels) × (number of pixels). Vectors μ_L and μ_H are concatenated low-energy and high-energy CT slice and x_1 and x_2 decomposition coefficients of the same dimension. The inversion of matrix A leads to:

$$A^{-1} = \frac{1}{\mu_{1H}\mu_{2L} - \mu_{2H}\mu_{1L}} \begin{bmatrix} \mu_{2L}I - \mu_{2H}I & -\mu_{1L}I \\ \mu_H I & \mu_{1H}I \end{bmatrix} \tag{26}$$

Although simple, this approach is limited by the invertibility of matrix A and usually introduces a large amount of decomposition noise [14]. Consider the term $1\,/\,(\mu_{1H}\mu_{2L} - \mu_{2H}\mu_{1L})$ and notice that it can be very large if $\mu_{1H}\mu_{2L} - \mu_{2H}\mu_{1L}$ is very close to zero. The difference between terms $\mu_{1H}\mu_{2L}$ and $\mu_{2H}\mu_{1L}$, in general, will be larger as the ability of the system to collect spectral information improves and there is less overlap between low and high energy collection channel. Furthermore, the ability of a system to collect data with the minimum amount of imaging noise is crucial because noise tends to get amplified during the decomposition process. The noise-cancellation ability of photon-counting detectors obtained by placing one of the energy thresholds just above the noise floor ensures lower fluctuations in spectral datasets.

The pseudo-inverse A^+ (Moore-Penrose inverse) of the matrix A is well-defined even for values $\mu_{1H}\mu_{2L} = \mu_{2H}\mu_{1L}$ in the matrix. In theory, $A^+ = A^{-1}$ when A is invertible, and when A is not invertible, A^+ inverts the invertible portion of A and suppresses the zero-eigenvalue component of A. Every matrix A has singular value decomposition (SVD) given by:

$$A = U\Sigma V^T \tag{27}$$

where U is a set of left-singular vectors in an orthogonal (or unitary) matrix of dimension $m \times m$, m is the number of rows of A, and V^T is the set of right-singular vectors and the transpose of an orthogonal (or unitary) matrix of dimension $n \times n$, where n is the number of columns of A. Σ is a diagonal matrix of dimension $m \times n$ and with non-negative diagonal entries in decreasing order $\sigma_1 \geq \sigma_2 \geq \sigma_3 \geq ... \geq \sigma_n$ where diagonal elements of Σ are the singular values of A. To obtain the pseudoinverse of the diagonal matrix Σ the reciprocal of the non-zero singular values and zeroing out the other entries is performed so that diagonal elements of pseudoinverse Σ^+ satisfy $\sigma_1 \geq \sigma_2 \geq \sigma_3 \geq ... \geq \sigma_k > 0$. The rank of A is k, and when k is less than n, then we can write:

$$A^+ = V\Sigma^+ U^T \,. \tag{28}$$

The pseudoinverse can be shown to solve an inconsistent $A\vec{x} - \vec{\mu}$ by finding the least squares solution that minimizes the L2-norm of $A\vec{x} - \vec{\mu}$.

2.1.1 Least-square fit material decomposition

In some imaging systems, more than two spectral information can be obtained. Instead of using traditional matrix inversion in equation 25 where only two spectral scans can be used as an input, the x_1 and x_2 coefficients can be computed using a least-square fit of the form:

$$\sum_i \left(\mu(E_i) - (x_1\,\mu_1(E_i) + x_2\,\mu_2(E_i))\right)^2 \tag{29}$$

where information from an arbitrary number of spectral channels E_i can be used. The fit procedure consists of a voxel-by-voxel minimization of the sum over the energies E_i of the squared residuals. From such a point of view, including more images of different energies adds further points to the plane, which is expected to increase the accuracy of the decomposition. In case the spectral data is contaminated by outliers (wrong pixel measurements) the least-squares solution can become significantly biased to avoid very high residuals on outliers, because the contribution of each measurement is scaled by the square term. A more robust estimator is the L1-norm estimator, in which the sum of absolute values of the residuals is minimized. Because the L1-norm function is non-differentiable everywhere, the optimization problem is hard, and it is often preferred to stay with differential problems such as least-square fit but incorporate robustness in estimation by introducing a sublinear function $\rho(r)$ and re-formulate the least-squares as an optimization problem:

$$\sum_i \rho\left(\mu(E_i) - (x_1\,\mu_1(E_i) + x_2\,\mu_2(E_i))\right)^2 \tag{30}$$

The problem can be reduced to standard nonlinear least squares as described in detail in [15]. A set of common sublinear functions is given in Fig. 9.

Several approaches to material decomposition exploring multiple constraints and regularization techniques can be found in literature [16, 17, 18].

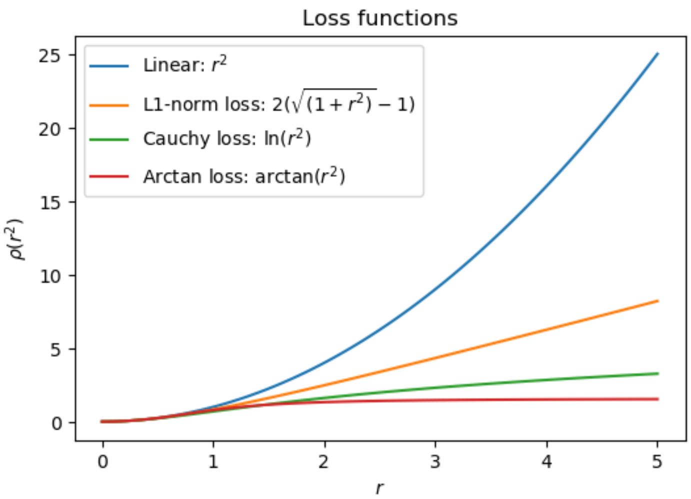

Figure 9: Loss functions useful for regularizing least squares solutions in the presence of outliers.

2.1.2 Singular value material decomposition

The singular value decomposition technique can be employed to decompose a tomographic (or radiographic) image in terms of the spatial distributions of a selected set of basis materials, much like the standard spectral decomposition originally introduced in Alvarez et al. [5] and most recently applied to tomographic images [19]. In this section we derive a mathematically enclosed connection between the values of 1st and 2nd principal components extracted through SVD and material maps PMMA and Al [20].

Fig. 10 illustrate the idea. Fig 10 a) shows a vector of length 100 consisting of a linear combination of 2 single materials (PMMA and Al) so that the first value represents pure PMMA and the last contains pure Al, while all values in between them contain a mixture of PMMA and Al, so that amount of PMMA decreases (blue line) and the amount of Al increases (red line). Using the X-ray attenuation database [21], μ values for PMMA and Al were selected for monochromatic energies of 20,30 and 40 keV and combined in proportions described in Fig. 10 a) to obtain μ values of a given mixture as shown in Fig. 10 b). As expected, the higher the contribution of Al in the mixture, the higher μ values are obtained. Standard SVD procedure is applied to the set of images and principal components are extracted in Fig. 10 c). The third principal component (PC), describing computational noise has a singular value equal to zero. The goal of this paragraph is to derive a mathematical procedure that puts in a linear correspondence the first two principal components extracted through SVD (Fig 10 c)) with the distribution maps of an arbitrary set of basis materials (*e.g.*, PMMA and Al) as shown in Fig. 10 d). The coincidence of constructed t and retrieved t' weight coefficients shown in Fig. 10 a) and Fig. 10 d) proves the concept of material decomposition through SVD.

The starting point is the consideration that a tomographic image F acquired at X-ray energy E

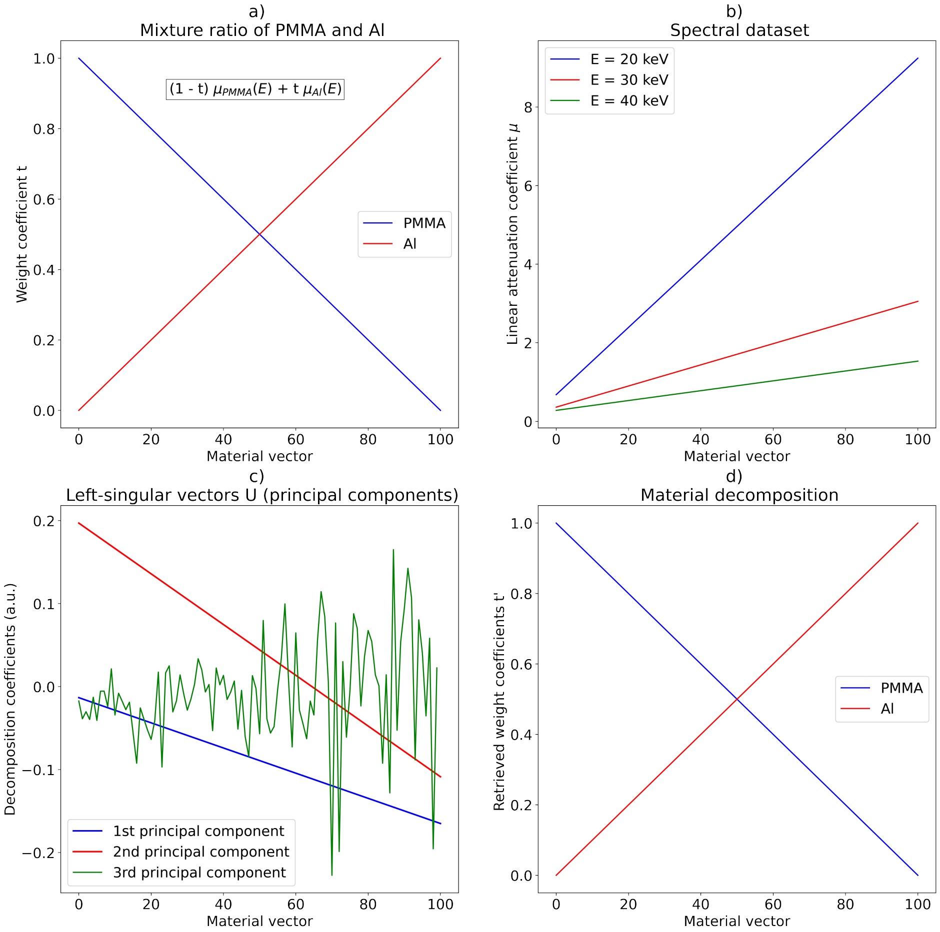

Figure 10: Scheme explaining the role of SVD in material decomposition. From left to right, a) an ideal dataset made as a mixture of PMMA and Al in various ratios and b) attenuation profiles at monochromatic energies of 20,30 and 40 keV. The decomposition with SVD is given in c) and the ratio of the two basis materials t' retrieved using the first two principal components is given in d). The scheme shows that $t = t'$ when there is no noise in the data.

can be described as a composition of the distribution maps x_a of a given set of basis materials

$$F_i(E) = \sum_a x_{ai}\, \mu_a(E) \tag{31}$$

where the index a labels the basis material, $\mu_a(E)$ is the corresponding attenuation coefficient at energy E and the index i identifies the pixel of an image flattened into a vector. A set of images acquired at energies E_p is therefore described as

$$F_{ip} = \sum_a x_{ai}\, \mu_{ap} \tag{32}$$

p being the index spanning the set of X-ray energies and $\mu_{ap} = \mu_a(E_p)$.

The matrix F defined in equation 32 is rectangular, of dimensions (number of pixels) × (number of energies). Applying SVD to such an object returns a set of left singular vectors u_n, right singular vectors v_n, and singular values σ_n (as shown in equation 27) such that

$$\sigma_n \, u_{ni} = \sum_p F_{ip} \, v_{np} \tag{33}$$

where the index n labels the singular value/vector. A notion that will prove useful in the future is that the left and right singular vectors are the eigenvectors of the matrices

$$\mathcal{U}_{ij} = \sum_p F_{ip} F^{\top}_{pj} \tag{34a}$$

$$\mathcal{V}_{pq} = \sum_i F^{\top}_{pi} F_{iq} \tag{34b}$$

respectively, both with eigenvalues $\lambda_n = \sigma_n^2$.

Substituting equation 32 into 34a gives

$$\mathcal{U}_{ij} = \sum_p \sum_a x_{ai} \, \mu_{ap} \sum_b x_{bj} \, \mu_{bp} = \sum_a \sum_b \mathcal{S}_{ab} \, x_{ai} \, x_{bj} \tag{35}$$

where the definition $\mathcal{S}_{ab} = \sum_p \mu_{ap} \, \mu_{bp}$ was used. Equivalently, substituting equation 32 into (34b) gives

$$\mathcal{V}_{pq} = \sum_a \sum_b \mathcal{I}_{ab} \, \mu_{ap} \, \mu_{bq} \tag{36}$$

with $\mathcal{I}_{ab} = \sum_i x_{ai} \, x_{bi}$.

Knowing the explicit form of matrices $\mathcal{U}$ and $\mathcal{V}$, it is possible to derive explicit expressions for their eigenvectors. It is possible to prove that the eigenvectors u_{ni} must be linear combinations of the basis material distribution maps x_a

$$u_{ni} = \sum_a \alpha_{na} \, x_{ai} \tag{37}$$

the α being the linear coefficients. An equivalent proof holds for the eigenvectors

$$v_{np} = \sum_a \beta_{na} \, \mu_{ap} \tag{38}$$

As a consequence of equations 37 and 38, the number of nontrivial solutions of the eigenvalue problems for matrix $\mathcal{U}$ (that is, $\mathcal{U} \, u = \lambda \, u$) and matrix $\mathcal{V}$ ($\mathcal{V} \, v = \lambda \, v$) cannot exceed the number of basis materials considered in the description.

Replacing equations 37 and 34a into the eigenvalue problem for matrix $\mathcal{U}$, and equations 38 and 34b into the one for matrix $\mathcal{V}$, leads to the compact relationships

$$\sum_a \left(\sum_b \Big(\mathcal{M}_{ab} - \lambda_n \, \delta_{ab} \Big) \, \alpha_{nb} \right) x_{ai} = 0 \tag{39a}$$

$$\sum_a \left(\sum_b \Big(\mathcal{M}_{ba} - \lambda_n \, \delta_{ab} \Big) \, \beta_{nb} \right) \mu_{ap} = 0 \tag{39b}$$

where $\mathcal{M}_{ab} = \sum_c \mathcal{S}_{ac} \, \mathcal{I}_{cb}$ and δ_{ab} is the Kronecker delta. Since the basis material distribution maps x_a (as well as their attenuation coefficients μ_a) are independent vectors in their respective spaces, the only way for equations 39 to hold is for each element of the sum to vanish separately, namely

$$\sum_b \Big(\mathcal{M}_{ab} - \lambda_n \, \delta_{ab} \Big) \, \alpha_{nb} = 0 \tag{40a}$$

$$\sum_b \Big(\mathcal{M}_{ba} - \lambda_n \, \delta_{ab} \Big) \, \beta_{nb} = 0 \tag{40b}$$

Equation 40a can be seen as the eigenvalue problem for the matrix $\mathcal{M}$, a square matrix whose dimensions are equal to the number N of basis materials considered in the decomposition. The literature [5, 19] is quite unanimous in defining such a number to be equal to 2 within the diagnostic imaging energy range. It is now worth noting that the coefficients α, as defined in equation 37, provide the desired relationship between the singular vectors u_n (output of the SVD algorithm) and the basis material distribution maps x_a (outcome of the procedure being defined here). Computing them is therefore the aim of the following discussion.

The first step in such direction is noticing that both v_n and μ_a of equation 38 are known quantities: the latter are tabulated in dedicated databases [21], while the former are outputs of the SVD algorithm. The coefficients β can therefore be computed, for example through a nonlinear fitting routine. Equation 40b is composed of $N \times N$ independent equations, one for each a and each n, in which the coefficients β are known from the previous step and the λ_n can be computed from the singular values σ_n (also outputs of SVD). In the case of $N = 2$, as assumed above, the matrix $\mathcal{M}$ can therefore be expressed as

$$\begin{aligned} \mathcal{M}_{11} &= \frac{\beta_{-2}\,\beta_{+1}\,\sigma_+^2 - \beta_{-1}\,\beta_{+2}\,\sigma_-^2}{\beta_{-1}\,\beta_{+2} - \beta_{-2}\,\beta_{+1}} & \qquad \mathcal{M}_{12} &= \frac{\beta_{-2}\,\beta_{+2}(\sigma_+^2 - \sigma_-^2)}{\beta_{-1}\,\beta_{+2} - \beta_{-2}\,\beta_{+1}} \\ \mathcal{M}_{21} &= \frac{\beta_{-1}\,\beta_{+1}(\sigma_-^2 - \sigma_+^2)}{\beta_{-1}\,\beta_{+2} - \beta_{-2}\,\beta_{+1}} & \qquad \mathcal{M}_{12} &= \frac{\beta_{-2}\,\beta_{+1}\,\sigma_-^2 - \beta_{-1}\,\beta_{+2}\,\sigma_+^2}{\beta_{-1}\,\beta_{+2} - \beta_{-2}\,\beta_{+1}} \end{aligned} \tag{41}$$

with the indices a and b spanning values $\{1, 2\}$ and the index n spanning values $\pm$. From the definition of $\mathcal{M}$ in terms of $\mathcal{I}$ and $\mathcal{S}$ (which is easily computable from the tabulated μ values), it is now possible to compute the former, which by definition obeys the symmetry $\mathcal{I}_{12} = \mathcal{I}_{21}$. Their analytical expressions are too complex to be reported explicitly here, but the numerical computation from known $\mathcal{M}$ and $\mathcal{S}$ values is straightforward.

At this point it is finally possible to solve the eigenvalue problem for α_n, as stated in equation 40a. With $N = 2$ the resulting constraints for the eigenvectors are easily written as

$$\frac{\alpha_{\pm 1}}{\alpha_{\pm 2}} = \frac{\mathcal{M}_{11} - \mathcal{M}_{22} \pm \sqrt{(\mathcal{M}_{11} - \mathcal{M}_{22})^2 + 4\mathcal{M}_{12}\mathcal{M}_{21}}}{2\mathcal{M}_{21}} \tag{42}$$

while the remaining degrees of freedom can be reduced through the unitarity of the singular vectors $u_\pm$, that is

$$1 = \sum_i (u_{\pm i})^2 = \mathcal{I}_{11}\ (\alpha_{\pm 1})^2 + 2\,\mathcal{I}_{12}\ (\alpha_{\pm 1}\,\alpha_{\pm 2}) + \mathcal{I}_{22}\ (\alpha_{\pm 2})^2 \tag{43}$$

Equations 42 and 43 allow a solution in terms of the coefficients α, which was the aim of the whole derivation. In fact, due to the quadratic nature of equation 43, they allow two distinct solutions for each value of n, for a total of four viable solutions. In fact, such degeneracy is intrinsic in the SVD algorithm: each set of singular values/vectors pertains to four distinct rectangular "set of images" matrices F. Luckily, such a feature does not pose an insurmountable obstacle towards the retrieval of the basis material distribution maps, as it is always possible to re-derive the matrix F from each of the four solutions, and then select the one that matches the original set of images.

2.2 Decomposition to density and effective atomic number

As we just showed, given two (or more) scans at different energies, the material decomposition approach can be used to describe the content of each voxel as a linear combination of the attenuation of two basis materials. Decomposition to two basis materials is the most common approach because two physical effects contribute to image formation in the diagnostic energy range: the photoelectric effect (PE) and the Compton scattering effect (CE). The photoelectric-Compton basis itself is very convenient because of the well-defined dependencies of these effects on density and atomic number. The photoelectric effect can be described by the following empirical relationship, taking into account material properties such as atomic number (Z), atomic mass (A), and density (ρ):

$$\mu_{\mathrm{PE}} \propto \frac{Z^n}{A\,\rho}\, f_{\mathrm{PE}}\,, \tag{44}$$

where f_{PE} describes the photoelectric effect dependence on the X-ray energy and is given as $f_{\mathrm{PE}} = 1/E^3$. The Compton contribution to the X-ray attenuation is empirically described as:

$$\mu_{\mathrm{CE}} \propto \frac{Z}{A\,\rho}\, f_{\mathrm{KN}}\,, \tag{45}$$

where energy dependence is given by the Klein-Nishina formula:

$$f_{\mathrm{KN}} = \frac{1+\alpha}{\alpha^2}\left(\frac{2(1+\alpha)}{1+2\alpha} - \frac{1}{\alpha}\ln(1+2\alpha)\right) + \frac{1}{2\alpha}\ln(1+2\alpha) - \frac{1+3\alpha}{(1+2\alpha)^2}\,, \tag{46}$$

and $\alpha = 1/510.975$ keV. From this point of view, one can rewrite the material decomposition in equation 24 as a linear combination of PE and CE contributions to material attenuation as:

$$\mu = \frac{Z^n}{A\,\rho}\,K_1\,f_{\mathrm{PE}} + \frac{Z}{A\,\rho}\,K_2\,f_{\mathrm{KN}} \tag{47}$$

where n, K_1, and K_2 are constants that can be obtained using a least-square calibration procedure as described in [5]. In principle, it is worth noting that these coefficients will depend on the energy range and the elements chosen for the calibration purpose. From there, one can see that solving the equation 47, which also can be solved only when spectral information is available, leads to an estimation of coefficients carrying the coupled information about element density, atomic number, and mass number. However, these coefficients will be quantitatively correct as long as the measurements (spectral image acquisition) are performed under the same conditions, the same energy and elements range, as the least-square calibration procedure. This restriction is encapsulated in coefficients n, K_1, and K_2. The same restrictions will hold true for the material decomposition approach, *e.g.,* the mixing ratios of water x_{water} and iodine x_{iodine} that describe an unknown material can be assumed to be constant only over energy range within which the said decomposition has been performed.

As we saw before, for elements composing biological tissue one can assume A = 2 Z, so that decomposition coefficients can be rewritten as:

$$x_{\mathrm{PE}} = \frac{K_1}{2}\rho\, Z^{n-1} \tag{48a}$$

$$x_{\mathrm{CE}} = \frac{K_2}{2}\rho\, Z \tag{48b}$$

Later in Sec. 6.1.1 we will focus on practical considerations of equations 48, discussing an experimental design as well as providing a mathematical recipe to decouple the density and atomic number information. However, before that, we need to focus on defining an equivalent of the atomic number of an element for materials consisting of several elements, such as compounds and mixtures.

2.2.1 The concept of effective atomic number

The atomic number is a physical property of an element, but the same concept cannot be trivially defined in compounds. An effective atomic number Z_{eff} is a concept derived to quantify the chemical composition of a material with a single quantity. Since it is a quantity to be defined, many different approaches to calculating Z_{eff} exist in the literature, well summarized in [22]. There, definitions of Z_{eff} are classified into two categories *i)* the ones that involve calculating Z_{eff} as some combination of atomic numbers Z_i of i_{th} atom constituting given compound [23, 24, 25, 26, 27] and *ii)* methods that compute Z_{eff} based on the mass attenuation coefficient of a compound [28, 29, 30] where Z_{eff} of a compound is ”an equivalent to an element of atomic number Z”. We included most of the published definitions in open-source GUI software ”Z*comp*ARE” [31]. Part of the software is built on top of the python library (xraylib 4.1.0 package, Python 3.10) of the xraylib database [32, 33] and can be used to compare approaches for computing atomic numbers of compounds from this database or list of user-defined materials can be provided.

Table 1: The comparison between several proposed methods to compute Z_{eff} which have been implemented inside ”Z*comp*ARE” software.

Tissues	Method A	Method B	Method C	Method D	Method E	Method F	Method G	Density ($\mathrm{g\,cm^{-3}}$)
Adipose Tissue	6.23	7.01	2.99	6.27	2.99	5.59	6.30	0.92
Blood	7.51	8.35	3.46	7.56	3.46	6.95	7.57	1.06
Bone, Compact	11.61	14.69	4.41	11.82	4.41	11.39	11.74	1.85
Bone, Cortical	12.97	15.73	5.29	13.16	5.29	12.92	13.13	1.85
Brain	7.46	8.40	3.31	7.51	3.31	6.82	7.53	1.03
Lung	7.27	8.38	3.47	7.30	3.43	6.67	7.31	1.05
Skin	7.17	7.95	3.42	7.21	3.42	6.57	7.23	1.10
Tissue, Soft	7.18	8.08	3.36	7.22	3.35	6.56	7.25	1.00

Method A: Spiers et al. 1946 [23], Method B: Glasser et al. 1947 [24], Method C: Hine et al. 1952 [25],
Method D: Tsai and Cho 1976 ($E < 150$ keV) [26], Method E: Puumalainen et al. 1977 [27],
Method F: Gowda et al. 2004 (also Direct-Zeff 2014) [28], Method G: Champley et al. 2019 (SIRZ-2)[30].

Decomposition to density ρ and the effective atomic number Z_{eff} is a step further toward extracting the physical information about tissue composition from spectral measurements. While material decomposition describes the attenuation of one material as a linear combination of the attenuations of other known materials, ρ/Z_{eff} decomposition exploits the underlying physics of X-rays interaction with materials to extract information about their physical and chemical properties. Several works have been published exploring this approach [34, 35, 36, 29, 30, 37, 20]. Density and Z_{eff} are intuitive units that can be easily interpreted and correspond to physical properties that can be measured by other techniques, allowing for easy comparison. Previous work showed the benefits of ρ/Z_{eff} for tissue differentiation [38], radiotherapy planning [39, 40, 41], and interventional radiology [42].

3 Spectral computed tomography

Since its introduction in 1917 and the pioneer works in the '60s and '70s of the last century [43], computed tomography quickly gained its popularity and became a valuable diagnostic modality not just in clinics, but also in industry. To this date, it is under constant development, improving detector technology, radiation sources, and computing power which allowed for more advanced reconstruction algorithms than the one introduced in section 1.3, leading to improved image quality at lower radiation doses. However, despite technological advances, the fact that several materials could share the same or very similar linear attenuation coefficient μ under the same source energy spectrum remains the major limitation of conventional CT. This is particularly true in medical imaging for similar soft tissues and some tumors that share imaging features with their surroundings.

3.1 Dual-energy CT systems

Dual-energy CT systems are readily present in clinical environments and different vendors came up with diverse technical solutions to obtain spectral information during a CT scan [44]. The most common approach is scanning with two different X-ray tube potentials to obtain on average lower and higher energy images. An example of different spectra generated from clinical CT X-ray tubes is given in Fig. 11.

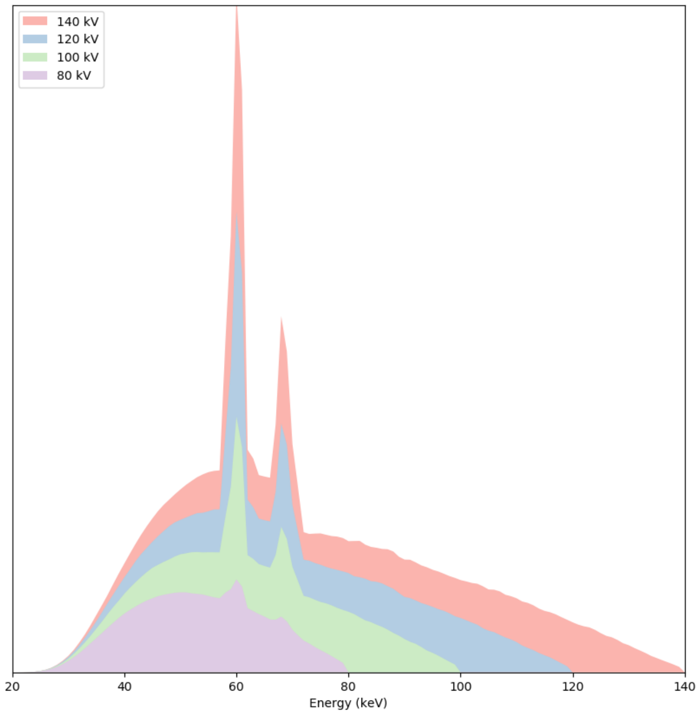

Figure 11: The set of spectral shapes for tube potentials of 80, 100, 120, and 140 keV. In clinical CT scanners, no more than two different tube potentials can be used simultaneously.

Canon Medical Systems has a series of models (Aquilion One family) that combine rapid kVp switching and/or rotate-rotate axial technology, offering the flexibility of both axial and helical scanning modes. In helical CT, the source continuously rotates around the patient while the patient table moves through the scanner, resulting in a spiral path of data acquisition. On the other hand, in axial mode, one full rotation is performed before the table is moved to a new position. Rotate-rotate axial mode refers to the acquisition of dual-energy data by rotating the gantry to different angles for each energy level. In this mode, the gantry is rotated to a specific angle to acquire high-energy data, and then it is rotated again to a different angle to acquire low-energy data. This process is repeated to obtain multiple views at each energy level, allowing for the reconstruction of dual-energy images. The main advantage of the rotate-rotate axial mode is the ability to acquire high- and low-energy data with a larger coverage area, as the gantry can be positioned at various angles during the scan. On the other hand, the helical kVp switch mode involves the acquisition of dual-energy data during a continuous helical scan. In this mode, the X-ray tube rapidly switches between high and low energy levels as the patient is moved through the rotating gantry during the helical scan. This allows for the acquisition of dual-energy data along the entire length of the scanned region. Helical kVp switch mode offers the advantage of faster scanning times and improved workflow. Models developed by GE Healthcare (Revolution GSI, Frontier, and ES models) utilize similar kVp switching technology - ultrafast kVp switching. Ultra-fast kVp-switching involves quick switching between 80 kVp and 140 kVp to ensure adequate energy separation between spectra. This process occurs in just 0.5 ms on the Revolution GSI and 0.25 ms on other systems. Siemens Healthineers employs two distinct dual-energy CT platforms for obtaining two-photon spectra during acquisition: Dual-Source CT (DSCT) platform (Somatom family) and split filter CT platform (Edge+, Xcite, Xceed, GoTop). The DSCT platform utilizes two X-ray tube/detector pairs with a 95° dephasing for the Somatom Force and Somatom Drive. One tube operates at low kVp (70 - 100 kVp), while the other employs high kVp, potentially with a tin (Sn) filter (140 kVp or Sn150 kVp) to enhance spectral separation. This platform offers various kVp pairs adaptable to patient morphology and clinical needs. The use of two tubes enables cardiac gating CT scans with temporal resolutions of 66 to 75 ms. However, the second tube's detector array is narrower (33 or 35 cm) than the first tube's (50 cm), resulting in a limited acquisition and reconstruction FOV. In the split filter CT platform, a single X-ray tube/detector pair with a 120 kVp (or 140 kVp) tube voltage is coupled with two filters to split energy spectra into low- and high-energy components. Philips Healthcare employs a different approach from its competitors as it uses detector-generated (dual-layer) detector technology for obtaining simultaneous dual-photon spectra in its IQon Spectral CT scanners. This technology enables spectral imaging without additional constraints and the decision whether spectral reconstructions will be needed doesn't need to be determined prior to acquisition.

However, low tube potentials of 80 and 100 kVp are not suitable for spectral imaging presumably because the average energy is too low to yield sufficient photon statistics in the second layer of the detector. Material decomposition is executed in the sinogram domain instead of image domain material decomposition preferred by other vendors.

3.2 Photon-counting CT systems

In the previous paragraph, we saw that most spectral scanners on the market (with the exception of the dual-layer approach) generate spectral separation by modifying the X-ray spectrum. This is because conventional CT detectors are energy-integrating detectors: they integrate the energy of incoming photons over some period of time to form the signal. Overlap of the energy spectrum in spectral sinograms obtained using multiple source potentials or multi-layer detectors is still significant. Besides the advantages of lower imaging noise, smaller pixel size, and more uniform spectral weighting related to photon-counting detection introduced in section 1.2.1, PCDs also provide inherent spectral separation of recorded X-ray photons [45, 46]. The first photon-counting CT (PC-CT) scanner available in clinics, NAEOTOM Alpha produced by Siemens Healthineers, is a dual-source CT scanner with two PCDs made of CdTe sensors with up to 4 energy thresholds available. Spectral separation is obtained through multiple threshold comparators attached to a single pixel element, which can be supplied with different external voltages and act as energy thresholds. Comparators compare photon-generated voltage signals against predetermined voltage levels. If the photon-generated voltage exceeds the set energy threshold, the photon is counted and assigned energy higher than the energy of the predetermined threshold. In photon-counting detectors each pixel contains several comparators, so this process is also repeated for other predetermined energy thresholds and final spectral information is obtained by threshold subtraction to obtain multiple energy bins. An ideal photon-counting detector would be able to separate photons from an X-ray tube in precisely defined energy bins as shown in Fig. 12.

Such spectral information would significantly improve the quality of the material decomposition approach and the quantitative imaging performance of spectral CT systems. However, as we saw before, PCDs suffer charge sharing and pulse pile-up effects. Charge sharing causes multiple counts at lower energies and blurring of the image, while pulse pileup leads to the count loss, in lower energy bins and potential increase of counts in high energy bins. Spectral distortions introduced by charge sharing and pulse pile-up have a significant impact on the accuracy of quantitative imaging tasks and could lead to misdiagnosis [13].

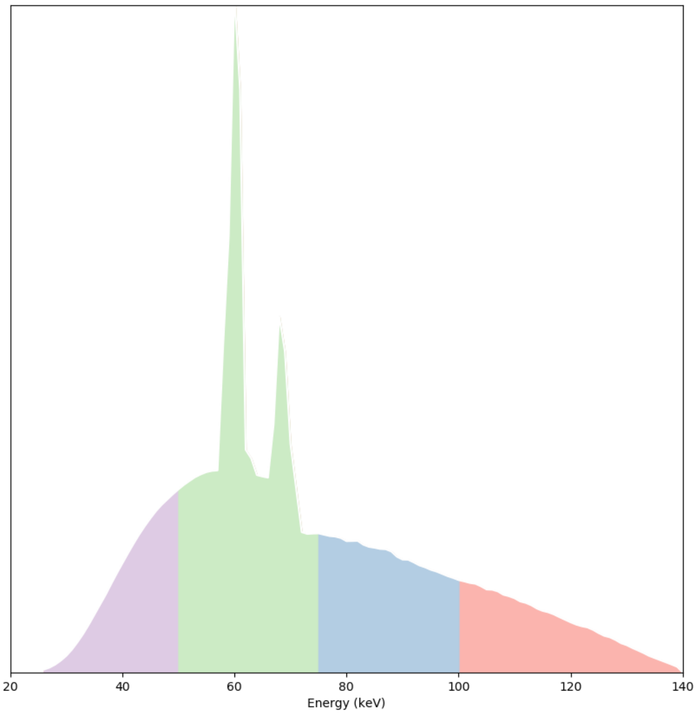

Figure 12: An ideal spectral response of photon-counting detection unit containing 4 comparators for an input polychromatic spectrum of 120 kVp.

3.3 Synchrotron computed tomography

Synchrotrons are state-of-the-art facilities designed to accelerate charged particles (*i.e.,* electrons) along curved trajectories through a magnetic field. Synchronous modifications of electric fields accelerate electrons to relativistic speeds, while the circular trajectory of the electron beam is ensured by a set of magnets, known as bending magnets. Bending magnets cause the energy emission of X-rays in the kV energy range as a byproduct of the bent trajectories, often called the synchrotron "white" beam. The white synchrotron beam contains an abundance of X-ray photons, a photon flux several orders of magnitude higher than in conventional anode sources. The synchrotron radiation beamline for medical applications (SYRMEP) at the Italian national synchrotron in Trieste, Italy obtains the maximum flux of 1.94×10^10 20-keV X-ray photons/mm^2/s at 2.0 GeV electron energy and typical ring current of 300 mA, while at 2.4 GeV and current of 100 mA it reaches 9×10^10 photons/mm^2/s of the same energy. Due to the characteristic emission spectrum of the bending magnet in the Elettra electron storage ring, the intensity drops as the energy of X-rays increases. Both spectral shapes for 2.0 and 2.4 GeV are given in Fig. 13.

The critical energy, which represents the energy at which the intensity of synchrotron radiation emitted by electrons is maximized (with the emitted power per unit energy interval reaching its peak), depends on factors such as the energy of the storage ring and the strength of the magnetic field. For

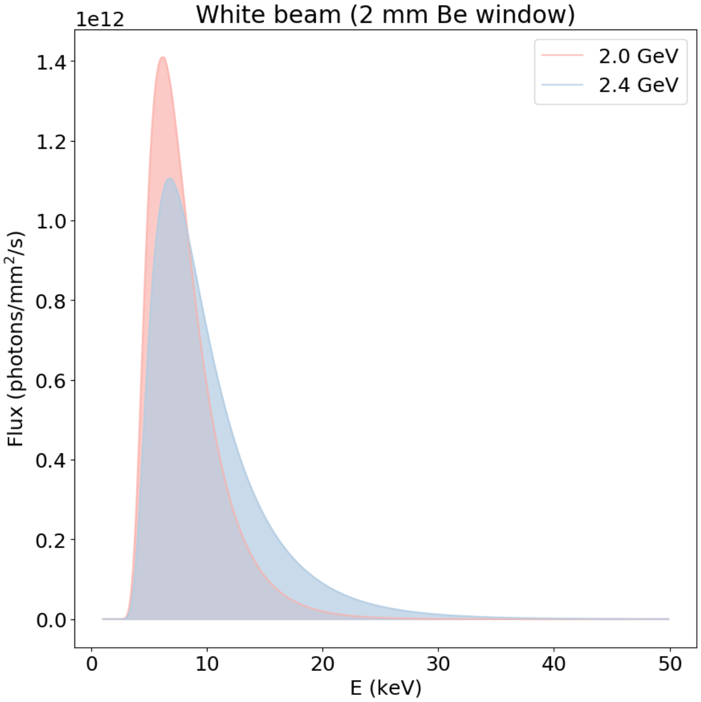

Figure 13: The shape of spectra ("white beam") obtained from bending magnet at SYRMEP beamline after 2mm Beryllium window at an electron beam energy of 2.0 and 2.4 GeV.

the specific configuration mentioned, the critical energy is 6.9 keV (at 2.0 GeV and 1.2T) and 8 keV (at 2.4 GeV and 1.45T). Because X-rays of energy below 20 keV are dominantly absorbed in biological samples such as breast, human or porcine heart, bones, etc. the beam is often filtered with different attenuators (*e.g.*, aluminum).

Without going into too much detail, we should note that besides bending magnets synchrotron radiation can be produced, even more effectively, at specialized magnetic configurations known as wigglers and undulators. These are called insertion devices because they are placed (inserted) in straight sections between the bending magnets without perturbing normal operation. The magnetic field is set up to have a sinusoidal variation along the trajectory of the charged particles which causes the electrons to undergo a sinusoidal motion, leading to the emission of synchrotron radiation. A simplified scheme of synchrotron operation containing bending magnets is given in Fig. 14.

The standout feature of synchrotron-generated X-rays is their high temporal and spatial coherence. Temporal coherence refers to the X-rays' ability to maintain a consistent phase relationship over time, while spatial coherence pertains to their ability to maintain a consistent phase relationship across space. Such characteristics are obtained from the synchronized motion of high-energy electrons within the accelerator resulting in an emission of an X-ray beam that is both coherent and intense. These properties allow almost exact energy selection of X-rays through monochromators usually made of a pair of silicon crystals because of their well-defined crystal lattice structures. When X-rays strike the

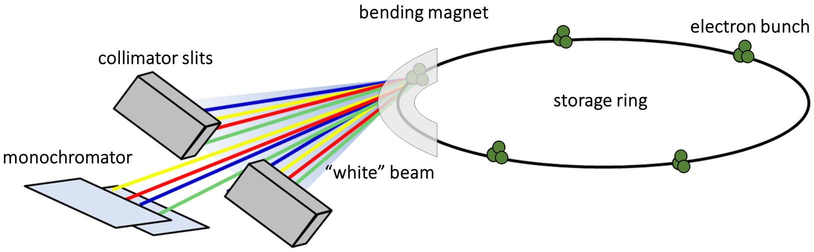

Figure 14: Simplified view of monochromatic X-ray generation using synchrotron beam. Electrons accelerated in the electron ring follow circular trajectories due to the banding magnets and emit bremsstrahlung X-ray radiation, here called the ”white” beam to emphasize its polychromatic nature. The beam is collimated with a set of collimator slits and monochromatic energy is selected using a double-crystal monochromator.

crystal at a particular angle, they are reflected (or diffracted) off the crystal planes in a way that constructive interference enhances certain wavelengths of X-rays while suppressing others. The energy of X-rays depends on the crystal lattice spacing and the angle of incidence which is adjusted by rotating the crystal in the X-ray beam. The relationship between these parameters is given by the Bragg law in equation 49

$$2d\sin\theta = n\lambda \tag{49}$$

where θ is the angle of incidence, λ is the wavelength of X-rays, d is the spacing between crystal lattice planes, and n is the diffraction order. The second crystal reflects the beam in a parallel direction to the incident beam on the first crystal and further refines the selection to a specific, narrow peak of wavelengths. Because the incoming beam is very intense, monochromatic beams with an effective energy resolution of $\Delta E/E \sim 0.1\%$ could be still more intense than conventional X-ray sources.

3.3.1 Phase-contrast

The coherent nature of a monochromatic synchrotron beam can be exploited for imaging biological tissues through phase contrast. Theoretically speaking, the phase-related δ values dominate the absorption β values of the refractive index, but experimental setups required to detect phase perturbations by an object using a conventional X-ray source are far more complicated and have not yet been implemented in clinical practice.

Figs. 15a and 15b show how both imaginary component β and real component δ of the refractive index n are characteristic quantities of a given material. For water, the substance that makes up around 60 % of the human body, the real component related to phase shift is $\delta_{H_2O} = 5.78 \times 10^{-7}$ and the imaginary component related to attenuation $\beta_{H_2O} = 3.47 \times 10^{-10}$ at 20 keV X-ray energy. The

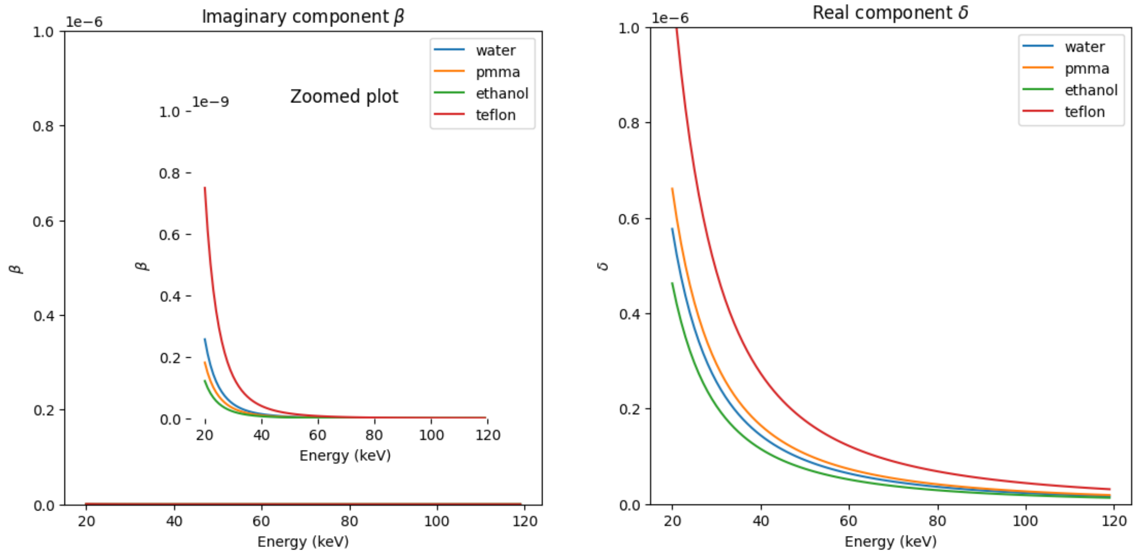

(a) (b)

Figure 15: Energy dependence of (a) imaginary component β and (b) real component δ of the refractive index n for diagnostic X-ray imaging for materials mimicking soft biological tissues. The scale is kept the same for both quantities (maximum value 10^{-6}), while the plot (b) containing δ values also shows a rescaled (”zoomed plot”) graph with the maximum value set to 10^{-9}.

large factor of $\sim 10^3$ in favor of phase shift suggests the opportunity for much better contrast and resolution using phase contrast imaging for a given dose.

Phase-contrast imaging is defined as any form of X-ray imaging that exploits the refractive properties of a sample to visualize it radiographically. Various techniques for X-ray phase contrast imaging are available, including the Bonse-Hart interferometer [47], analyzer-based phase-contrast imaging [48], and grating-based methods [49]. All of these methods need specialized optical components, in addition to an X-ray source and detector. A method that distinguishes itself by not requiring any specialized optical elements beyond the conventional detector and a coherent source is called the propagation-based X-ray imaging method. In a nutshell, the propagation-based technique simply allows for the propagation of phase-shifted X-rays by placing a detector at an increased distance z' from a sample. To understand the benefit of phase propagation we re-consider the X-ray propagation equation 7 laid out in Sec. 1.1 from the perspective of wave optics. As pointed out before δ is related to phase shift $\Delta\phi$ as $k\delta L$. In equation 7 one assumes that the perturbation of a wavefield is entirely determined by phase and amplitude shifts, in literature known as projection approximation. The phase-shift term ϕ is understood as a local distortion of the wavefront. At a specific point on the object plane, this distortion causes a slight alteration in the propagation direction concerning the incident planar wave. To calculate the outgoing propagation direction at each point, we assume that deviations from the initial direction (z) are small, which can be expressed formally as the paraxial approximation. In other words, the absolute values of the spatial derivatives $\frac{\partial\phi(x,y)}{\partial x}$ and $\frac{\partial\phi(x,y)}{\partial y}$ are much smaller than the wave number (k). Consequently, the outgoing wave vector can be represented as follows:

$$\mathbf{k}_{\mathrm{out}}(x,y) = \frac{\partial \phi(x,y)}{\partial x}\mathbf{x} + \frac{\partial \phi(x,y)}{\partial y}\mathbf{y} + k\mathbf{z} \tag{50}$$

Here, $\mathbf{x}$, $\mathbf{y}$, and $\mathbf{z}$ are unit vectors pointing along the x, y, and z directions, respectively. The deviation from the original direction ($\mathbf{z}$) imposed on the beam by the refractive object is expressed as a position-dependent refraction angle ($\alpha(x,y)$), which can be written as:

$$\alpha(x,y) \approx \frac{1}{k}\left(\left(\frac{\partial \phi(x,y)}{\partial x}\right)^2 + \left(\frac{\partial \phi(x,y)}{\partial y}\right)^2\right) = \frac{1}{k}\left|\nabla_{xy}\phi(x,y)\right| \tag{51}$$

Here, ∇_{xy} represents the gradient operator in the object plane. The small angle deviation causes the X-rays to impinge on the detector at the position (x', y'), given by:

$$\begin{aligned} x' &= x + z'\alpha_x(x,y) \\ y' &= y + z'\alpha_y(x,y) \end{aligned} \tag{52}$$

where α_x and α_y represent the projections of α in the planes xz and yz, respectively. Equation 52 straightforwardly expresses the coordinate transformation that maps each ray from the object plane to the detector plane [50]. These projections are calculated as:

$$\begin{aligned} \alpha_x &= \frac{1}{k}\frac{\partial}{\partial x}\phi(x,y) \\ \alpha_y &= \frac{1}{k}\frac{\partial}{\partial y}\phi(x,y) \end{aligned} \tag{53}$$

By calculating the transformation Jacobian, one can express the intensity detected in the image plane as follows:

$$\begin{aligned} I(x',y') = I(x,y)\left|\frac{\partial(x',y')}{\partial(x,y)}\right|^{-1} \\ = I(x,y)\begin{vmatrix} 1 + z'\frac{\partial \alpha_x}{\partial x} & z'\frac{\partial \alpha_x}{\partial y} \\ z'\frac{\partial \alpha_y}{\partial x} & 1 + z'\frac{\partial \alpha_y}{\partial y} \end{vmatrix}^{-1} \\ \approx I(x,y)\left(1 - \frac{z'}{k}\nabla^2\phi(x,y)\right) \end{aligned} \tag{54}$$

Equation 54 involves the Laplacian operator ∇^2 in the object plane, where the approximation is obtained by neglecting terms of $O(z'^2/\lambda^2)$. This approximation is reasonable because, in a typical phase-contrast imaging setup, z' is on the order of meters while λ is around 10^{-10} meters. When $z'k\nabla^2\phi(x,y) \ll 1$, meaning that the phase contrast is weak [50], equation 54 can be further simplified as:

$$I(x', y') \approx I_0 e^{-2k\beta(x,y)\Delta} \left(1 - \frac{z'}{k} \nabla^2 \phi(x, y)\right) \tag{55}$$

Here, I_0 represents the X-ray intensity incident on the object and $\nabla^2 \phi(x, y)$ represents the Laplacian of the phase term $\phi(x, y)$, which characterizes the phase change of the X-rays as they pass through the object. The equation 55 is called the transport of intensity equation (TIE) [51] and is essential for understanding the effects of phase propagation on image formation. In the case of a very small detector-sample distance $z' \to 0$ the image registered would be a result of pure attenuation contrast in the sample. On the contrary, as we increase z', phase contrast becomes significant as it is directly proportional to the Laplacian of the phase shift. When dealing with a planar impinging wavefront, phase contrast increases in a linear fashion as the propagation distance grows and becomes more pronounced at the boundaries or sharp interfaces of the refractive object. At these locations, where the phase shift changes abruptly, it results in what is known as the "edge enhancement effect". Obtaining the contrast from phase shift effects involves a TIE-based phase retrieval approach. In its simplest form, it implies the inversion of equation 55 to compute ϕ from $I(x', y')$. The mathematical formalism of phase-retrieval using TIE is beyond the scope of this thesis and interested readers are referred to [51]. However, it should be noted that images acquired in the free space propagation regime provide significant improvement in the CNR which can reach up to 10-fold improvement compared to pure attenuation contrast for an optimal propagation distance as reported by Gureyev et al. [52] on carbon sphere objects, and explained thoroughly in a follow-up publication [50].

SYRMEP beamline has been specifically designed to exploit the free space propagation technique for the imaging of breast cancer. Brombal et. al [53] performed a study specifically designed to measure the improvement of SNR in breast specimens, reporting up to a 20-fold improved SNR for the largest propagation distance compared to a conventional CT setup. Breast cancer imaging is particularly challenging due to the small differences in the composition compared to fibrous, glandular, fat, and cancer tissue. It is a task where phase-induced contrast can significantly help to improve tissue differentiation at multiple monochromatic energy levels. We will show later in Sec. 6.4.2 how the pre-clinical setup at SYRMEP exploits the joint contribution of synchrotron-based monochromatic X-ray imaging in phase propagation mode and a spectral photon-counting detector to compute density and effective atomic numbers of breast tissues. Because the synchrotron source is stationary, the tomographic acquisition is performed through the rotation of the patient table instead of the source.

4 Virtual (in-silico) computed tomography

Computed tomography (CT) has become a pivotal imaging modality for patient screening, diagnosis, and treatment planning, leading to continuous advancements in CT systems to enhance diagnostic accuracy and minimize radiation exposure. Traditionally, the evaluation of new advancements is performed in the act of clinical trials which involve imaging physical phantoms or actual patients. Imaging studies on physical phantoms are easy to set up and repeatable with a high degree of control but lack the complexity required for task-based or patient-specific assessments, while patient imaging is lengthy and expensive, with a series of ethical considerations. Practically, it happens that tested advancements are already overcome with other ones before conclusive evidence is collected. Furthermore, traditional clinical trials are ground truth limited, which makes comparing new technology to objective ground truth impossible and becomes a significant limitation for the interpretability of artificial intelligence solutions. To address these challenges, virtual imaging trials (VITs) or in-silico imaging trials have emerged as promising solutions, enabling clinical experiments to be conducted through computer simulations. In a virtual platform, complete X-ray physics is modeled using analytical simulations or Monte Carlo methods, eliminating the need for physical scanners. Virtual patients are created by segmentations of scans obtained from prior acquisitions on different diagnostic imaging modalities such as CT or MRI, enabling anthropomorphic phantom geometry without ethical concerns about radiation exposure. This approach results in faster and more cost-effective trials. The effectiveness of VITs heavily relies on the realism of two critical components: patient modeling and modeling of the image acquisition chain. Extensive efforts have been made to develop populations of anthropomorphic phantoms that accurately represent detailed organ anatomies, including intra-organ heterogeneities in organs such as the breast, lungs, liver, and bones. On the acquisition side, several CT simulators based on Monte Carlo (MC) methods have been developed [54]. While MC-based simulators accurately capture the X-ray interaction process, their slow computation speeds limit their application for generating high-resolution CT images necessary for realistic image quality assessments, especially when simulating imaging of a large population of phantoms. To overcome these challenges, alternative approaches such as GPU-accelerated MC, ray-tracing, and hybrid simulators combining ray-tracing and MC techniques have been introduced. These methods provide faster image generation and are suitable for realistic image quality assessments. DukeSim CT simulator is a hybrid simulation platform [55] developed to rapidly generate scanner-specific CT images of voxelized computational phantoms. The simulator consists of a primary signal generator using X-ray propagation and a Monte Carlo module for estimating X-ray scatter contribution to image formation. By combining these two signals and accounting for the physics of the detector elements, DukeSim computes projection images with realistic characteristics. A detailed description of the DukeSim CT simulator is given in [55]. Similar open-source CT simulators, such as XCIST or VICTRE, have emerged as valuable tools in the field. All of these platforms offer a powerful avenue for developing, evaluating, and optimizing scanner-specific technologies in the clinical context. What differentiates DukeSim software from others is the high computation speed and presence of state-of-the-art features such as a photon-counting detector model.

In the following sections, the work on modeling photon-counting detectors for CT image acquisition with details of modeling several physical effects occurring in the process of detection will be presented. On one side, parameters of this model can be adapted to model CT scanners already on the market (*e.g.,* NAEOTOM Alpha by Siemens Healthineers) with an idea to test and optimize the available technology, or to develop and predict the potential of new technology in the initial phase of development, yet to enter the clinical environment. An example of such a project will be given in the section 4.1.4, where the potential of instant-retrigger technology designed by Dectris LTD to improve the capability of photon-counting detectors in high-flux conditions was tested using DukeSim CT simulator. These attempts illustrate how virtual simulations can be used beyond clinical trials for the development of new technology, reducing the time and cost of testing new ideas.

4.1 Photon-counting detector modeling

To accurately model the physics of image acquisition in photon-counting computed tomography, it is crucial to incorporate realistic models of the signal generation process in photon-counting detectors, considering factors such as X-ray crosstalk due to the fluorescence effects in the sensor, charge sharing, and pulse pileup. Previous studies have proposed various models to describe the detection process in PCDs, including cascaded parallel system models [56] and simulation frameworks combining Monte Carlo and analytical techniques [11, 57, 13, 58]. Analytical models have also been developed to account for the probability distributions of photon energies, inter-arrival times, and pulse shapes, thereby estimating both spatial distribution effects resulting in charge sharing among the neighboring pixels and spectral distortion effects of pulse pileup. While these studies have enhanced our understanding of PCDs and their impact on image quality in PCCT, their utility for realistic VITs is limited due to several factors. These include the lack of comprehensive models considering the combined effects of X-ray crosstalk, charge sharing, and pulse pileup across various detector designs, limited or no validation against physical measurements, and the absence of an established methodology for efficient simulation of scanner-specific images in clinical PCCT systems. The work on the development and validation of a modular detector response model that incorporates the combined effects of X-ray crosstalk, charge sharing, and pulse pileup on the image formation process in CdTe-based photon-counting detectors is described here. The developed methodology integrates these detector response models with the DukeSim CT imaging simulation platform, enabling the flexible and efficient simulation of scanner-specific images for both existing and upcoming clinical PCCT systems. By addressing these challenges, this research contributes to the advancement of PCCT imaging and its potential for realistic and comprehensive VITs in a clinical setting.

4.1.1 Stochastic interactions model

A Monte Carlo simulation code developed in Geant4 (v.10.6) was utilized to model the stochastic interactions between incident X-ray photons and the bulk of the detector. The simulation geometry consisted of a rectangular X-ray source (S) emitting a uniform beam of monochromatic X-rays, directed towards the central pixel (C) of the detector, as shown in Fig. 16. The distance between the source and detector was arbitrary, as the choice did not impact the simulation outcomes, considering the vacuum environment defined for the simulation. The detector was represented as a 100 × 100-pixel array with detector-specific dimensions (d_x, d_y, and d_z). To minimize boundary effects, a large pixel array was selected for simulating X-ray photon transport. The Livermore physics list [59] in Geant4 was employed, which accounts for interaction processes within the energy range relevant to diagnostic imaging, including photoelectric absorption, Compton and Rayleigh scattering, fluorescence, Bremsstrahlung, and ionization. Each simulation was performed with 10^5 histories (or events) per run, and the coordinates (x_i, y_i, z_i) and energy (E_i) of all photon interactions resulting in energy depositions within the detector were recorded.

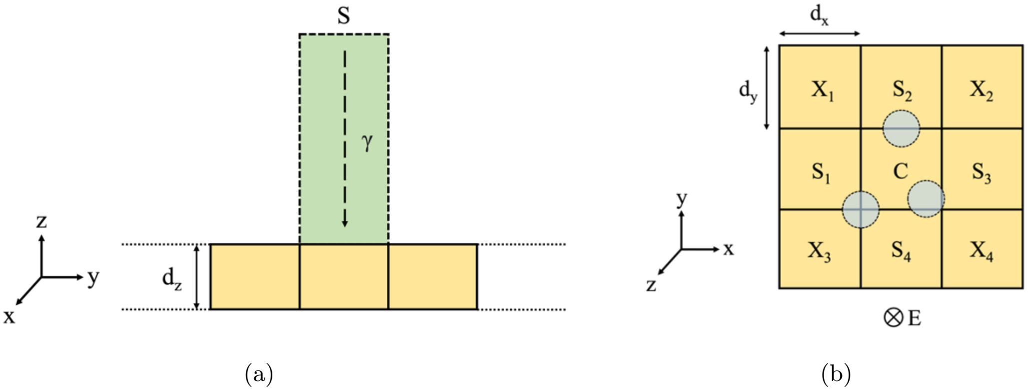

Figure 16: An overview of the geometry employed in Monte Carlo simulations to model the probabilistic interactions between incoming X-ray photons and the detector. Panel (a) shows a side view and panel (b) shows a 3x3 pixel (C, S, X) neighborhood with a possibility of 2, 3, or 4 pixels involved in charge sharing.

4.1.2 Charge sharing model

An analytical simulation was developed in MATLAB (Mathworks, Natick, MA) to model pixel crosstalk arising from charge sharing. This simulation utilized the list of photon interactions obtained from the Monte Carlo simulation as input. Sequentially selecting interactions within a single event, the analytical simulation binned them into pixels based on location and pixel size. Charge clouds were then modeled at the location of these interactions. The spatial density of charge within the charge cloud was determined to follow a 2D isotropic Gaussian distribution with a standard deviation (σ) given by the equation:

$$\sigma = \sqrt{\frac{2(d_{iz}kT)}{eV} + \frac{(d_{iz}dN_e)}{10\pi\epsilon V}\frac{1}{\sqrt{5}\sigma_i} + \sigma_i^2} \tag{56}$$

Here, d_{iz} represents the distance of the interaction location from the collection surface along the direction of the electric field, d is the thickness of the detector, k is the Boltzmann constant, T is the absolute temperature, e is the electron charge, V is the bias voltage, N_e is the number of electron-hole pairs liberated, ϵ is the permittivity, and σ_i is the initial size of the charge cloud. This formulation takes into account both charge diffusion in the direction of the electric field and charge repulsion perpendicular to the electric field. The initial width of the charge cloud was assumed to be 5 μm. For computing N_e, the energies for liberating a single electron-hole pair and the Fano factors were 4.43 eV and 0.12 for CdTe, respectively.

To estimate the energy deposited in the surrounding neighborhood of a 3×3 pixel array (C, S, X) centered around the pixel C assigned to the interaction location in Fig. 16b, the method assumes that the energy shared is proportional to the projection areas of the charge cloud onto the anodes of those pixels. The projection areas were computed by numerically integrating the 3D Gaussian charge cloud projections onto the collection surface, with the limits defined by the pixel boundaries. The maximum number of neighboring pixels simultaneously sharing the charge cloud was 6 pixels for CdTe as it was determined that considering a larger neighborhood does not change simulation output and increases computation time. The combined shared energy within the 3×3 pixel array for all interactions within an event was then converted to photon counts using multiple energy thresholds, with the selectable parameter of electronic noise (σ_e). The electronic noise refers to noise in the detector electronics with thermal noise in the passive resistive elements of the ASIC being the dominant contributor. This analytical charge-sharing simulation was performed for all simulated photon transport events, and the resulting photon counts across all energy thresholds were normalized using the total number of simulated events (10^5).

4.1.3 Non-paralyzable detector model

To address the influence of pulse pileup on the recorded spectral data from detector pixels, only counting logics belonging to the non-paralyzable family were considered, as paralyzable detectors underperform in high flux conditions. A general non-paralyzable analytical model was adopted from a previously established method [11]. The model calculates the average number of photons $m(E)$

recorded by a detector pixel at energy bin E while accounting for pulse pileup effects. The calculation incorporates the true count rate (a), which would be the rate of photon counts in an ideal detector, and the probability of photons being recorded, denoted as $\frac{a_R}{a}$ (where a_R signifies the recorded count rate). The influence of pulse pileup is encapsulated by a summation over all possible orders of pileup (i). Each term in this sum is weighted by the probability of the i-th order pulse pileup occurrence $Pr(E|i)$.

Mathematically, the $m(E)$ is expressed as a combination of probabilities:

$$m(E) = a \times \Delta t \times Pr(rec|a\tau) \times \sum_{i=0}^{\infty} \left[Pr(i|rec) \times Pr(E|i)\right] \ , \tag{57}$$

where $Pr(rec|a\tau)$ Poisson probability of events being recorded, $Pr(i|rec)$ probability of the pulse pileup order i given the events-of-interest being recorded, $Pr(E|i)$ probability of counts recorded at an energy E with pulse pileup order i, and τ corresponds to the detector deadtime. Replacing the probabilities with

$$Pr(rec|a\tau) \quad = \tfrac{1}{1+a\tau} \ , \tag{58}$$

$$Pr(i|rec) \quad = \tfrac{(a\tau)^i e^{-a\tau}}{i\,!} \tag{59}$$

$$\tag{60}$$

the final analytical model can be defined as

$$m(E) = a \times \frac{1}{1+a\tau} \times \sum_{i=0}^{\infty} \left[\frac{(a\tau)^i e^{-a\tau}}{i\,!} \times Pr(E|i)\right] \ . \tag{61}$$

To calculate $Pr(E|i)$ efficiently, we established lookup tables based on the premise that photons reaching the detector generate energy-proportional delta pulses. This approach deviates from the original model where the bipolar pulse is represented with a triangular shape. The cumulative recorded energy is obtained by summing the energies of pulses within a defined integration window. It's worth noting that, for practical purposes, the highest order of pileup considered when computing $m(E)$ was limited to $i = 3$, as subsequent increases in accuracy were found to be negligible.

4.1.4 Instant-retrigger detector model

The "instant-retrigger" pulse pile-up model was implemented using a previously published [60] analytical method incorporating retrigger capability in a paralyzable detector counting model. The model is based on assumptions that the arrival of events follows a Poisson distribution with an average true incoming rate q, the signals exhibit rectangular shapes with width τ_P, the retrigger time τ_R exceeds the pulse width τ_P, and the amplitudes of signals are mutually independent stochastic variables, distributed according to a probability function corresponding to the energy spectrum $S_E(\epsilon)$. The recorded count rate m above a certain threshold E$_{th}$ is given as:

$$m(E > E_{th}) = \frac{a - \frac{B}{\tau_P}}{a\tau_R + e^{-a\tau_P} + 2A + \frac{\tau_R}{\tau_P}B}\,, \tag{62}$$

where

$$A = \sum_{i=1}^{\infty} \Pr(i|\tau_P) S_{E_i}(E_{th})\,, \tag{63}$$

and

$$B = \sum_{i=1}^{\infty} i\Pr(i|\tau_P) S_{E_i}(E_{th})\,. \tag{64}$$

Term $\Pr(i|\tau_P)$ represents Possion probability given as:

$$\Pr(i|\tau_P) = \frac{(-a\tau_P)^i e^{-a\tau_P}}{i!}\,, \tag{65}$$

while $S_{E_i}(E_{th})$ is a cumulative distribution function for i pulse pile-up events. For this study, the sum was safely terminated at $i = 3$ representing 3rd-order pulse pile-up events as shown in Fig. 17.

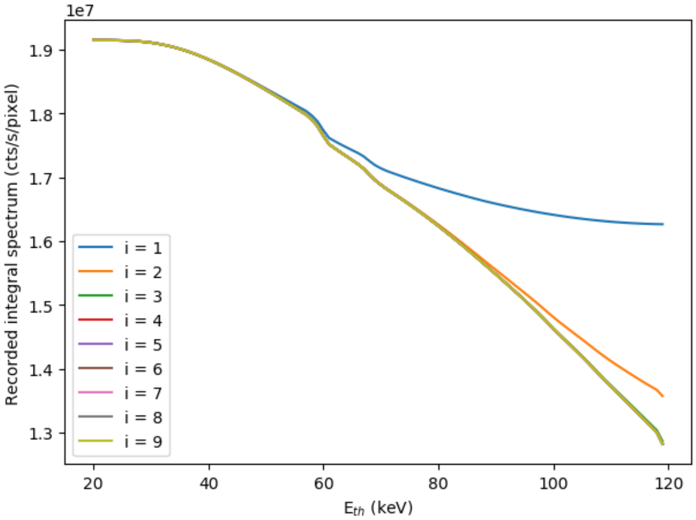

Figure 17: Recorded integral spectrum considering the increasing number of pileup events allowed in analytical model.

The non-paralyzable and instant-retrigger models sightly differ in their assumptions, where the non-paralyzable model considers delta pulse shape while the instant-retrigger model considers rectangular pulse width of adjustable shape. The output of the non-paralyzable model is recorded counts for a given energy (or energy range) while the instant-retrigger model gives counts over the selected threshold.

4.2 Validation of models

The validation process of the developed detector response model consisted of the validation of photon transport and charge sharing model using experimental data obtained in a separate study [61]. The data acquisition employed a large-area photon-counting detector (PixiRad-1/Pixie-III) featuring a CdTe sensor with a thickness of $650\,\mu$m. This detector had pixels measuring $62 \times 62\,\mu$m, spanning a total active area of $3.17 \times 2.49\,\mathrm{cm}^2$ (512×402 pixels). The data was acquired at $-30°$C, utilizing a monochromatic synchrotron X-ray source at energies of 26, 33, 37, and 50 keV. The integral spectra were obtained through threshold scanning, and differential spectrums were derived through numerical differentiation. To address the charge-sharing effect among pixels, the detector employed three operational modes. The "neighborhood pixel inhibit and pixel summing" (NPISUM) mode assigns the total energy of an event involving up to 4 pixels to the pixel receiving the highest fraction of the total energy. While NPISUM operation mode allows for well-preserved energy peaks and corrects for effects of charge sharing, it is prone to pulse pileup due to longer processing times. The effect was minimized by acquiring data in the linearity range of the detector (fluence rate $< 2 \times 10^6$ photons $\mathrm{mm}^{-2}\ \mathrm{s}^{-1}$). For 26 keV, additional data was available corresponding to the two other modes, the "neighborhood pixel inhibit" (NPI) mode and no summing mode (NONPI). The latter operates with no correction to the counting process, while the NPI mode is similar to the NPISUM mode but assigns the energy of the pixel receiving the highest fraction of total energy to the event energy without performing any summing of the charge detected in the neighborhood.

The experimental conditions for data acquisition were replicated to validate our photon transport and charge-sharing model. Since the data was acquired in the linearity range of the detector, the effects of pulse pileup were not modeled at this step of the validation. The implementation of NPI and NPISUM modes involved modification of the analytical charge-sharing simulation to apply corrections to a neighborhood of 2×2 pixels surrounding the pixel with maximum energy deposition within a simulated event. The specific neighborhood of 2×2 pixels was chosen based on the minimum distance of interaction location from the pixel corners. Since NPISUM corrects for most effects of charge sharing, no charge sharing was simulated at locations of interactions for that mode. For each incident energy and mode, a total of 10^5 events were simulated.

The experimentally obtained energy spectra can be distorted by various sources of noise, including statistical and electronic noise. Here, statistical noise refers to the fluctuations in the energy required for electron-hole pair generation in the detector bulk. The contribution of noise was introduced to our simulated spectra using experimentally measured energy resolutions (quantified as the full width at half maximum - FWHM). Since the energy resolutions were determined only at specific energy peaks (e.g., 26, 33, 37, and 50 keV monochromatic beams), we needed to estimate how statistical and electronic noise (cumulatively) affect the detector's energy resolution at other energies. To do this, we performed a linear fit on the standard deviations ($\sigma_{s+e}(E)$) computed from the measured FWHM values. This allowed us to model the combined effect of statistical and electronic noise on the degradation of the detector's energy resolution at different energy levels. The collective blurring from statistical and electronic noise was incorporated in the simulated spectra using this linear fit to introduce Gaussian fluctuations (with σ_{s+e} as the standard deviation) in the threshold energy while converting photon energies to counts. For comparison, both the experimental and the simulated spectra for each incident energy were normalized using the area under the respective curves.

To validate the analytical non-paralyzable pileup model, the Monte Carlo method to generate the stochastic arrival times and integrate photon pulses at a non-paralyzable detector was used. Like the analytical model, the code generates delta pulses proportional to photon energies and sums their energy within the integration window to produce the integrated signal. Implemented in MATLAB, the simulation models photon pulses arriving at the detector as a Poisson process with count rate a, leading to the interarrival times of the photons being sampled from an exponential distribution with a mean of $1/a$. The energies of the individual photon pulses were sampled from a 140 kV spectrum (15-140 keV, bin width of 5 keV) and integrated at the detector using a running integration window of width corresponding to the deadtime τ of the detector. The count rate in this study (a) was defined relative to the detector deadtime (τ) using the dimensionless parameter $a\tau$. For validation, values of $a\tau$ = 0.1, 0.5, and 1.0 were considered, with 10^6 pulses sampled for each count rate. The simulated spectra with effects of pileup were then compared to that predicted by the analytical method for each count rate. The analytical instant-retrigger model has been validated against Monte Carlo simulation by Zambon et al. [60].

4.3 Charge-sharing validation results

Fig. 18 shows the experimental and simulated spectra for a CdTe-based detector ($0.062 \times 0.062 \times 0.65$ mm) at an incident beam energy of 26 keV using the "no summing" (NONPI) and the "neighborhood pixel inhibit" (NPI) mode. For both NONPI and NPI, the experimental and simulated spectra show agreement with $R^2_{\text{NONPI}} = 0.89$ and $R^2_{\text{NPI}} = 0.94$ and peak shift towards lower energies for the main peak in the simulated spectra (E_{peak} = 25 keV) compared to the experimental spectra (E_{peak} = 26 keV).

Fig. 19 shows experimental and simulated spectra for the same detector at incident energies of 26, 33, 37, and 50 keV using the "neighborhood pixel inhibit and pixel summing" (NPISUM) mode. An agreement of $R^2_{\text{NPISUM}} = 0.98$, 0.90, 0.91, and 0.95 between experimental and simulated spectra were observed for the NPISUM mode at incident energies of 26, 33, 37, and 50 keV, respectively. Since the

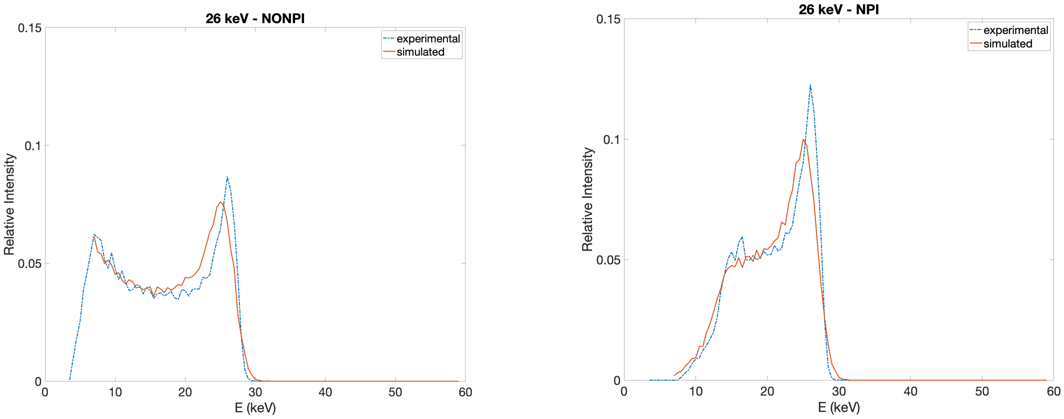

Figure 18: Experimental and simulated spectra for a CdTe-based detector ($0.062 \times 0.062 \times 0.65$) at an incident beam energy of 26 keV using no summing (NONPI) and the neighborhood pixel inhibit (NPI) mode.

incident energy of 26 keV is less than the K-edges of Cd ($E_{K,\mathrm{Cd}} = 26.7$ keV) and Te ($E_{K,\mathrm{Te}} = 31.8$ keV), no fluorescence and escape peaks were observed in both the simulated and experimental spectra. For other incident energies ($E = 33, 37, 50$ keV), as expected, fluorescence peaks for Cd were observed at the energy of $E_{K\alpha,\mathrm{Cd}} = 23.1$ keV, while the corresponding escape peaks for Cd and Te were observed at $E - E_{K\alpha,\mathrm{Cd}}$ and $E - E_{K\alpha,\mathrm{Te}}$ ($E_{K\alpha,\mathrm{Te}} = 27.4$ keV), respectively. No fluorescence peaks were observed for Te as $E_{K\alpha,\mathrm{Te}}$ is slightly above $E_{K,\mathrm{Cd}}$, leading to mean free paths comparable to the pixel size and high susceptibility for those photons being reabsorbed within the pixel. Similar to NPI, the slight inconsistencies in the heights of the fluorescence and escape peaks can be attributed to the lack of exact details on the implementation of the NPISUM mode. Although the experimental data was acquired in the linearity range of the PixiRad-1/Pixie-III detector, the longer processing times of the NPISUM can introduce distortions in the experimental spectra due to the effects of pulse pileup.

4.4 Non-paralyzable validation results

Fig. 20 shows the spectra after pulse pileup estimated for a 140 kV input spectrum (15-140 keV, bin width: 5 keV) using a Monte Carlo (MC) simulation modeling pileup of delta pulses and the corresponding analytical approximation method utilized in this study for 3 different products of count rate and deadtime (aτ = 0.1, 0.5, and 1.0). For all count rates considered, the spectra estimated using the analytical method and the MC simulation show close agreement of $R^2 > 0.99$. For both simulated and analytical spectra, spectral distortion characterized by low-energy photons piling up to higher energies was observed for all non-zero count rates with increased distortion for increasing incident count rates by 10%, 50%, and 100%, respectively.

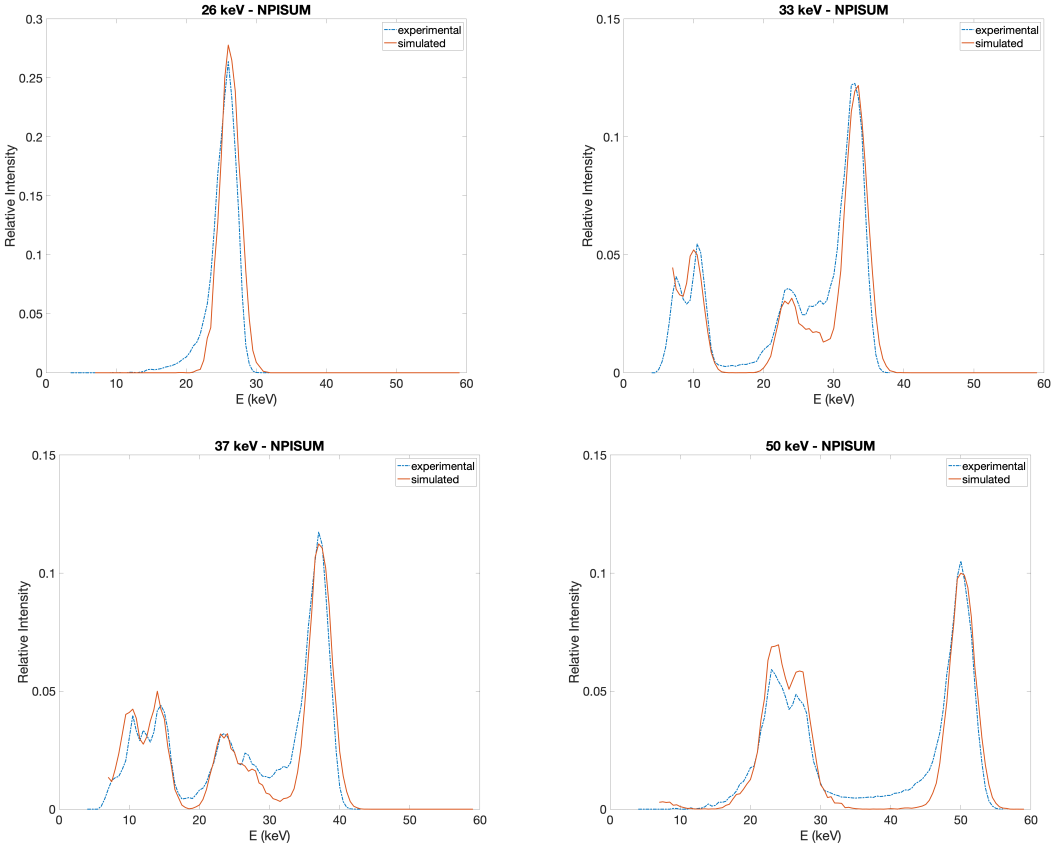

Figure 19: Experimental and simulated spectra for a CdTe-based detector ($0.062 \times 0.062 \times 0.65$) at incident beam energies of 26, 33, 37, and 50 keV using the neighborhood pixel inhibit and pixel summing (NPISUM) mode.

4.5 Integration of models in DukeSim CT simulator

The effects modeled in this study were implemented in a virtual imaging framework for simulating photon-counting CT images, specifically utilizing the DukeSim simulation platform. In this work, DukeSim was adapted to model the scanner-generic geometry featuring a CdTe detector with pixels measuring 0.5×0.6 and a sensor thickness of 1.6 mm.

The photon transport and charge-sharing simulators were utilized to compute matrices containing the quantum efficiencies $R(E, t_n)_{i,j}$, representing the counts detected per incident photon on the central pixel, for all pixels ($i, j \in C, S, X$) in the 3×3-pixel neighborhood of the central pixel across all energy thresholds t_n, as well as the corresponding spatio-energetic covariance matrix $Cov(E, t_m, t_n)_{i,j;k,l}$, which contains covariance values computed for all combinations of neighboring pixels ($i, j; k, l \in C, S, X$) and energy thresholds (t_m, t_n). The monochromatic quantum efficiency and covariance matrices were computed using monochromatic simulations ranging from 10 keV to 150 keV, with 10^5 events simulated per energy. The quantum efficiencies $R(E, t_n)_{i,j}$ were used to compute the noise-free mean signal $M(t_n)$ for all pixels in the 3×3-pixel neighborhood for a given energy threshold (t_n) as:

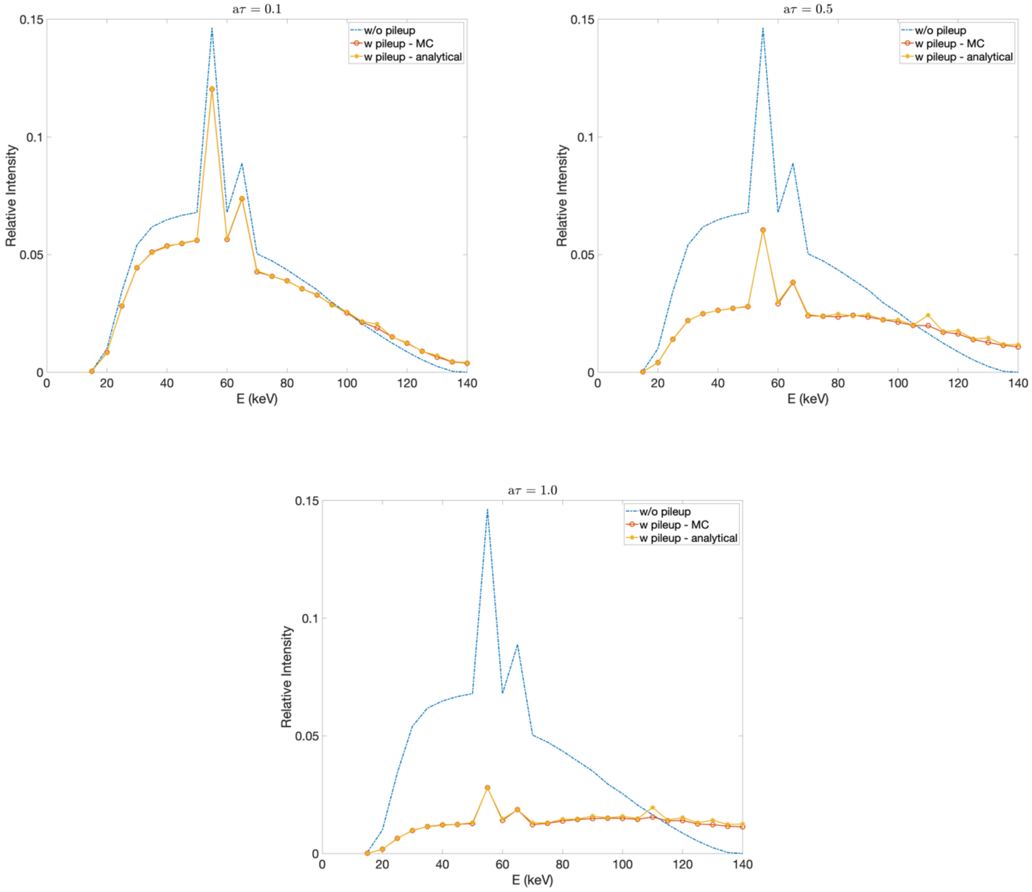

Figure 20: Spectra after pulse pileup estimated for a 140 kV input spectrum (15-140 keV, bin width: 5 keV) using a Monte Carlo (MC) simulation modeling pileup of delta pulses and the corresponding analytical approximation method utilized in this study for 3 different count rates (aτ = 0.1, 0.5, and 1.0).

$$M(t_n) = \sum_{E} \sum_{i,j \in C,S,X} N_{\mathrm{attn}}(E)_{i,j} \cdot R(E, t_n)_{i,j} \tag{66}$$

Where $N_{\mathrm{attn}}(E)$ represents the number of photon counts at energy E hitting the pixels after attenuation through the phantom. Similarly, the total covariance $Cov(t_m, t_n)_{i,j}$ for the correlated noise associated with the mean signal for a given pixel (i, j) and pair of thresholds (t_m, t_n) was computed using the spatio-energetic covariance matrix $Cov(E, t_m, t_n)_{i,j;k,l}$ as:

$$Cov(t_m, t_n) = \sum_{E} \sum_{i,j \in C,S,X} N_{\mathrm{attn}}(E)_{i,j} \cdot Cov(E, t_m, t_n)_{i,j} \tag{67}$$

The noisy signal for a pair of thresholds (t_m, t_n) was then estimated using multivariate Gaussian random variables with means $M(t_m)$ and $M(t_n)$ and the covariance matrix $Cov(t_m, t_n)$. To incorporate the effects of pulse pileup in the non-paralyzable detector, noisy spectral projections, and the corresponding air scans were simulated using multiple pairs of energy thresholds to obtain energy-binned projections, which were then processed using the method described in Sec. 4.1.3. The values of the true count rate (a) for each pixel were computed as the sum of the counts across all energy bins and adjusted for the total acquisition time of the scan. The implementation of the instant-retrigger model was simpler because the model takes counts above the threshold as an input. The projections were logged using air scans to compute attenuations and corrected for the effects of beam hardening using a 4th-order polynomial water correction before reconstruction.

Fig. 21 shows the normalized mean, variance, and covariance of counts for incident energies 10-150 keV summed across the 3×3 pixel neighborhood for energy thresholds of $t = 20$ and $t = 60$ keV for CdTe- ($0.5 \times 0.6 \times 1.6$ mm) detector modeled in this study. Across both energy thresholds, the magnitudes of mean and variance of counts were observed to peak with increasing energy (including secondary peaks from K-edges of Cd and Te at 26 and 31 keV) from the threshold cutoff to monotonically decrease at higher energies.

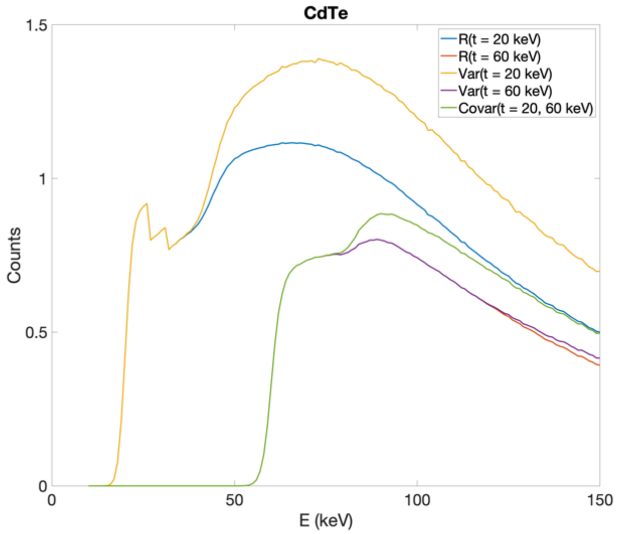

Figure 21: The normalized mean, variance, and covariance of counts for incident energies 10-150 keV summed across the 3×3 pixel neighborhood (C, S, X) for energy thresholds of $t = 20$ keV and $t = 60$ keV for CdTe-based ($0.5 \times 0.6 \times 1.6$ mm) sensors modeled in this study.

Fig. 22 shows the corresponding covariance matrices for incident energies of 60 and 90 keV for all pixels in the 3×3 pixel neighborhood for energy thresholds of 20 and 60 keV. As expected, incident energy of 60 keV only shows signals at thresholds of 30 and 60 keV while incident energy of 90 keV shows signals in all thresholds (30, 60, and 90 keV). A high covariance (up to 0.7) in counts was observed between the central (C) and the neighboring pixels (S, X) for both incident energies, with a relatively larger inter-pixel spread in the lowest threshold (30 keV) for 90 keV.

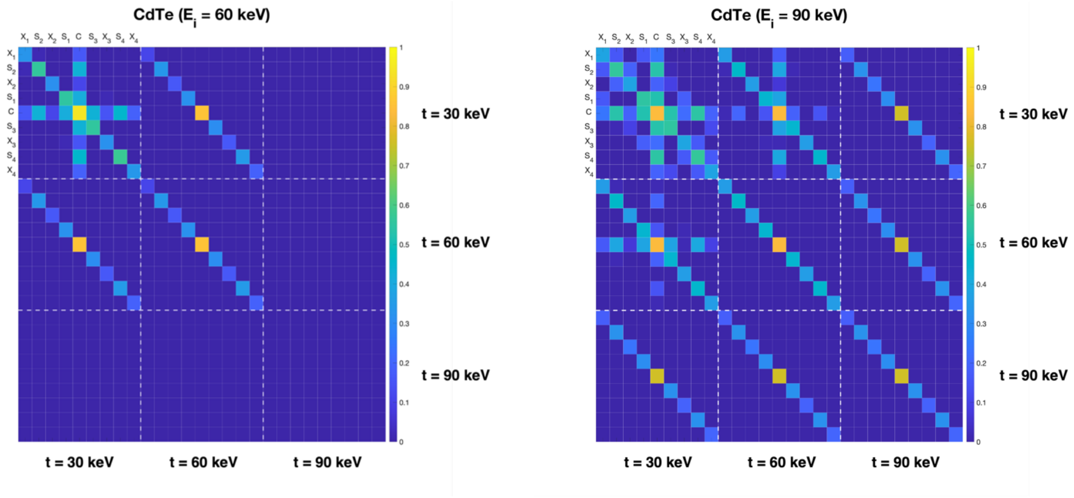

(a) (b)

Figure 22: Covariance matrices for incident energies (a) $E_i = 60$ keV and (b) $E_i = 90$ keV for all pixels the 3×3 pixel neighborhood (C,S,X) for energy thresholds of $t = 30$ keV, $t = 60$ keV, and $t = 90$ keV for CdTe-based ($0.5 \times 0.6 \times 1.6$ mm) detector modeled in this study.

4.6 Discussion of detector response model

In this study, a modular detector response model was developed and validated, accounting for the combined effects of X-ray fluorescence, charge sharing, and pulse pileup on the image formation process in CdTe-based photon-counting detectors. The simulated spectra for the CdTe-based detector (PixiRad-1/Pixie-III) at an incident energy of 26 keV using no summing mode and the NPI mode were found to be in good agreement (avg. $R^2 = 0.92$) with the experimental spectra. The peak shift towards lower energies for the main peak observed in the simulated spectra compared to the experimental spectra can be attributed to the blurring applied to model the energy resolution of the detector. Particularly, in Fig. **??** symmetric Gaussian blurring of the spectra skews the main peak toward the lower energies because of the high contribution of the low energy tail created by charge sharing events. In the other spectra (*e.g.*, the ones in Fig. 19) this effect is less pronounced in the main peak as it stands more isolated due to the effects of charge sharing being eliminated in the NPISUM operation mode. The $\sigma_{s+e}(E)$ used for modeling the energy resolution were computed as a linear fit on the FWHM values measured on experimental data acquired using the NPISUM mode, which might not apply to other modes. The close agreement ($R^2 > 0.99$) of the analytical approximation method with the MC simulation for incorporating the effects of pulse pileup demonstrates the feasibility of this approach for the processing of energy-binned count data for a variety of true count rates and detector deadtimes. The slight overestimation of magnitudes (up to 3%) at the bin corresponding to 110 keV is due to the particular choice of energy bins considered for validation, which leads to the maximum number of combinations of delta pulses whose sum of energies results in a total energy of 110 keV.

It was observed that increasing the number of bins by reducing the bin width rectifies this issue at a cost of increased computational time. Since only unipolar delta pulses piling up as summation of energies within the integration window were considered in this study, the spectral distortion from pulse pileup presents itself as a shift in the expected spectra towards higher energies. The mean, variance, and covariance of counts in Fig. 21 were observed to have a dependence on the incident energy and the choice of energy thresholds. The mean and variance of counts increase from the threshold cutoff energy peak with increasing energy due to increased multiple counting above the threshold due to the fluorescence effects and charge sharing, and then monotonically decrease at higher energies due to decreasing attenuation of CdTe. There are also secondary peaks observed at energies corresponding to the K-edges of Cd (26.7 keV) and Te (31.8 keV) due to increased absorption of incident photons in the detector. The imperfections in the energy thresholds arise due to the presence of electronic noise that was added during the modeling process. Similar trends were also observed in the covariance matrices in Fig. 22, reinforcing the incident energy and threshold dependence of covariance values observed in Fig. 21.

The limitations of this study are reflected in the definition of the charge cloud size utilizes a constant value of the initial charge cloud size (σ_i), which might not accurately reflect the physical reality. For increased accuracy, the σ_i should be defined using either the Kanaya-Okayama radius or be derived using MC simulations. The charge cloud sizes can also be calibrated using experimental measurements for a given detector design. Second, the methods for incorporating the effects of pulse pile-up in the projection data assume unipolar delta (pulse-width $pw = 0$) or rectangular delta pulses (pulse-width $pw > 0$). Although leading to efficient computations, unipolar delta pulses might not be as realistic as alternate pulse shapes such as a unipolar triangular or bipolar triangle with long negative tails, which additionally lead to pileup from high to low energies. Future versions of the study need to validate the pile-up model against experimental data for a variety of pulse shapes to find the most relevant match.

4.7 Material decomposition in the presence of charge sharing and pulse pile-up

To demonstrate the viability of our model to perform clinically relevant VITs for PC-CT, we integrated the developed detector response model with an existing imaging framework for CT to generate scanner-specific images of an anthropomorphic imaging phantom. The influence of charge sharing and pulse pileup on the detector spectral response was evaluated through the clinically relevant task of material decomposition.

4.7.1 Simulation setup

The anthropomorphic phantom of the abdomen and thorax region was created using the XCAT phantom generator software [62], simulating iodine contrast injection for cardiac perfusion CT scan. The appearance of the phantom is given in Fig. 23.

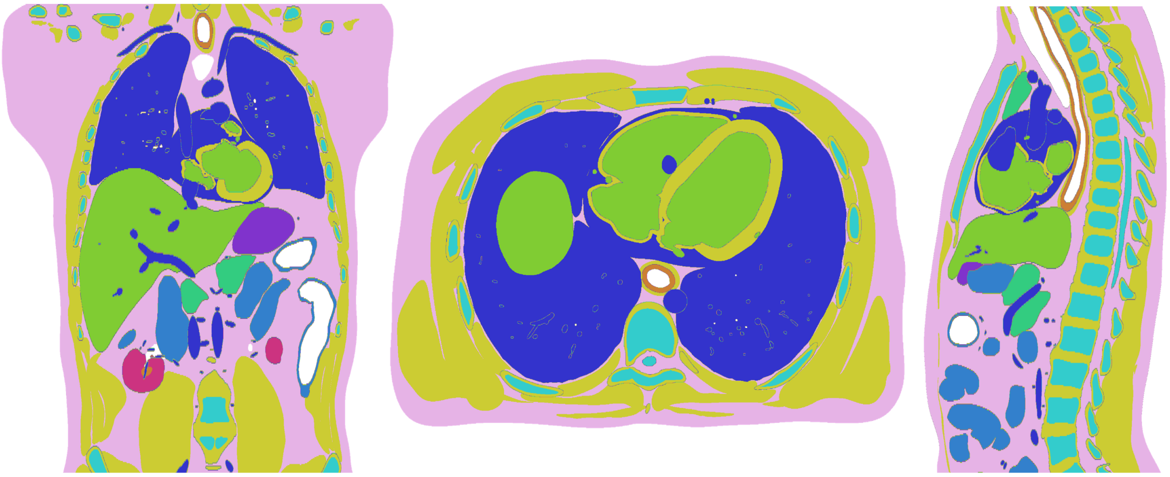

Figure 23: Antrophomorphic abdomen and thorax phantom generated using XCAT software. Images are color-coded to emphasize that this is a ground truth phantom that is to be fed to the CT simulator.

Images were acquired with axial tube rotation at a tube current of 150 mAs, rotation time of 1 s, and a tube potential of 120 kVp. The instant-retrigger analytical model was adapted to matrix form and applied in projection space specifying energy thresholds of 20 keV and 65 keV, as this is the common output of the clinical NAEOTOM Alpha PCCT scanner. The nominal pulse width τ_P was set to 12 ns and retrigger time was varied in the range of 15 - 35 ns, with the step of 5 ns. The data was reconstructed using Astra Toolbox [63] cone-beam filtered backprojection to obtain 20 and 65 keV threshold reconstructions with a 37 cm FOV and matrix size 800 × 800 pixels. The material decomposition algorithm described in Sec. 2.1.2 was applied in image space to obtain iodine images and virtual monochromatic images, using water and bone as basis materials. The workflow is illustrated in Fig. 24.

4.7.2 Simulation results

Fig. 25 shows the influence of retrigger time on the redistribution of weights in the water-bone material decomposition process. Iodine and water decomposition coefficients are determined by averaging values across a 50 × 50 pixel region within the central slice of the XCAT phantom, which contains the heart artery (aorta) filled with iodine contrast, heart muscle, and body fat.

In the presence of strong photon flux, a rapid retrigger of counters suppresses the pulse pileup and leads to more accurate material decomposition. Using a fast retrigger time (15 ns) quantitatively accu-

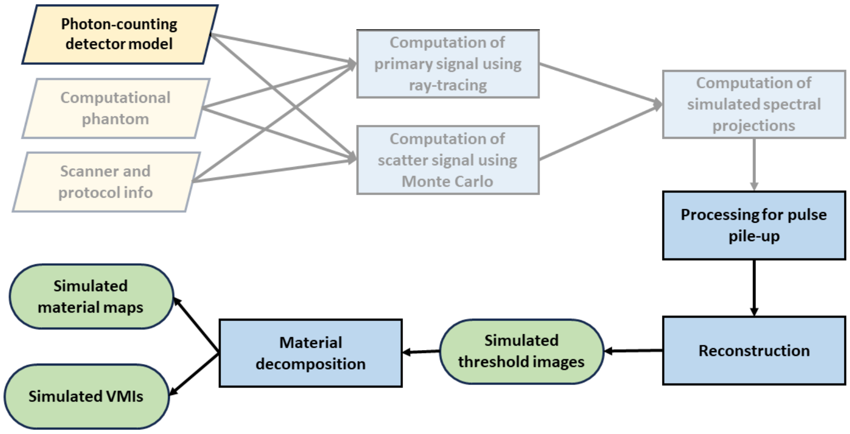

Figure 24: Implementation of charge sharing and pulse pileup model into a DukeSim virtual CT platform. The charge-sharing model is implemented in the detector response, while the pulse pileup model is applied in the projection domain.

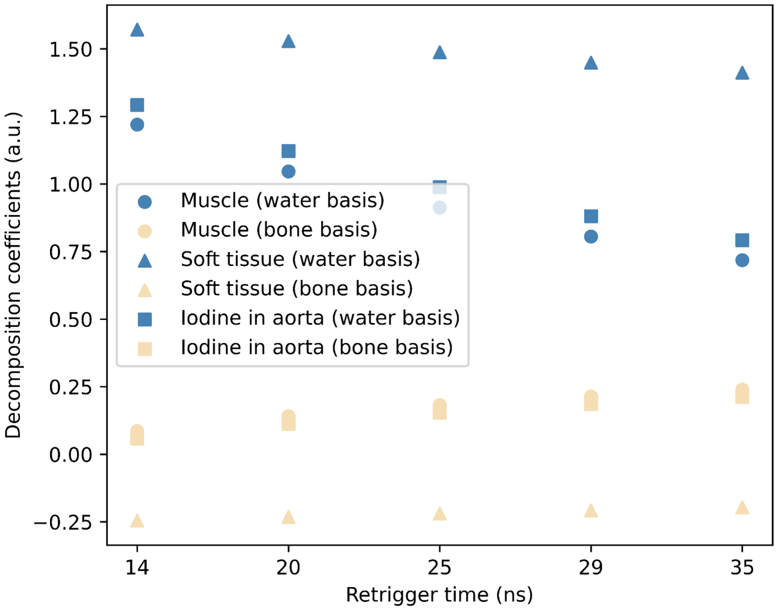

Figure 25: Material decomposition weights for muscle, soft tissue, and iodine solvent in water and bone basis as a function of retrigger time in high flux condition.

rate material decomposition can be performed to compute virtual monochromatic images at different energy levels as demonstrated in Fig. 26.

Iodine contrast spread in the aorta and heart can be qualitatively observed as more enhancing at low VMI (50 keV) than at higher VMI energy levels. Finally, pulse pileup influences the accuracy of VMI through material decomposition. Fig. 27 shows how slower retrigger times suppress less pulse pileup effects and can lead to a slight underestimation of 8.4 % when comparing the 15 and 30 ns retrigger times.

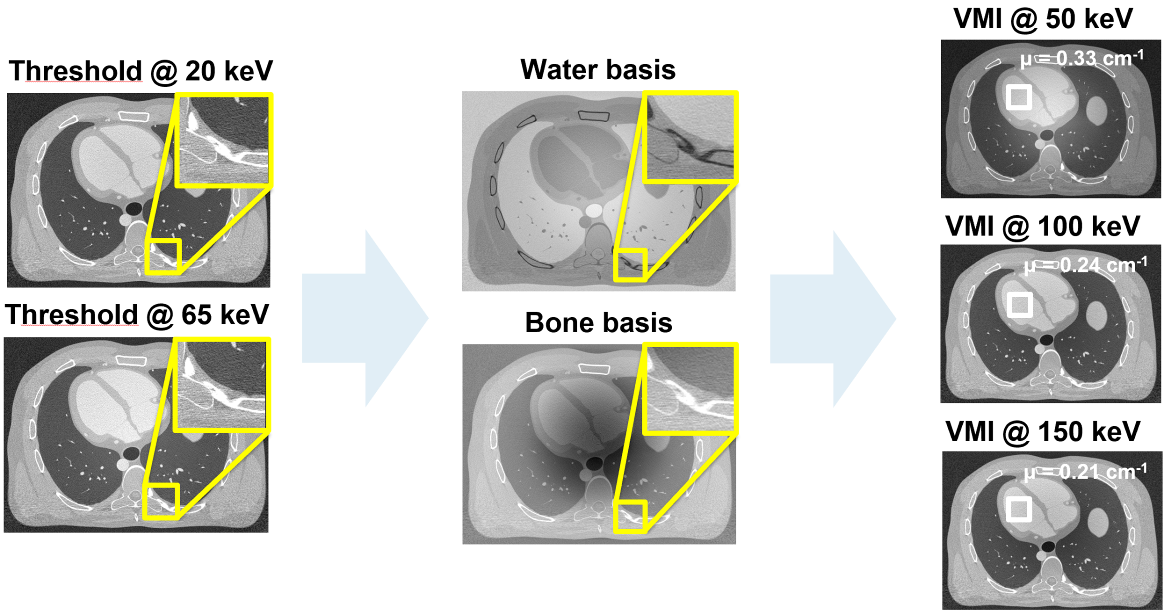

Figure 26: Low (20 keV) and high (65 keV) energy threshold reconstructions of XCAT phantom are decomposed into water and bone material maps. From said decomposition, VMIs at 50, 100, and 150 keV were reconstructed.

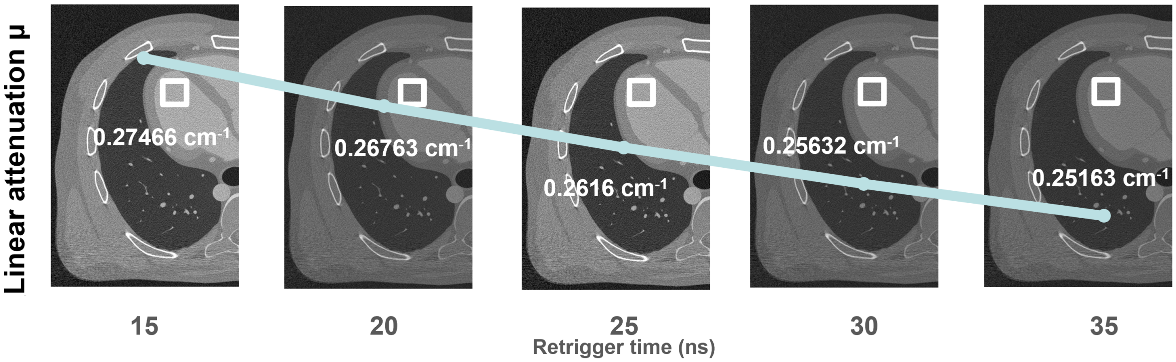

Figure 27: Virtual monochromatic images at 70 keV were reconstructed for a set of decreasing retrigger times. Linear attenuation coefficients were measured from a 50 × 50 region inside the heart ventricle as marked on the slices.

The obtained results indicate the necessity of fast retrigger times in the presence of increased photon flux for accurate quantitative imaging. More advanced flat-field correction techniques based on empirical projection-based material decomposition approach and pre- and post-processing steps could also prove valuable in suppressing or efficiently mitigating the influence of pulse pileup on the quantitative accuracy of measured data [64, 65, 66].

5 Photon-counting spectral CT in clinics

Spectral computed tomography (CT) has allowed the possibility of a more quantitative evaluation of data acquired from clinical scanners. Virtual monochromatic imaging (VMI) and iodine quantification (IQ) are the major quantitative representations in spectral CT to highlight specific attributes of clinical information. For example, VMI promises to offer improved differentiation of tissues by targeting specific points of their $\mu(E)$ dependence, while further correcting for beam-hardening artifacts[67] with benefits in imaging abdomen [68], lungs [69] and head and neck [70]. The clinical relevance of iodine quantification has been reflected in many studies. The most significant application includes the studies of pulmonary disease [71], coronary artery disease through the detection of myocardial ischemia based on contrast distribution [72], tumor status (eg., thymic epithelial tumor [73]), differentiation of metastatic and non-metastatic lymph nodes [74], renal masses and hepatocellular carcinoma [75, 76, 77], and lung cancer where iodine quantification has significant diagnostic and prognostic power. Increased popularity and demand for VMI and IQ has resulted in several studies testing their accuracy, precision, and repeatably across different vendors and scanning conditions offering spectral information. Most investigations have focused on the identification of sources of error when estimating quantitative parameters and comparing results from different scanner generations. Jacobsen et al. [78] performed a study measuring the iodine concentration bias from different scanners and computing VMI data at several energies. Following the suggestion from this paper, Euler et al. [79] conducted a large study among second and third-generation CT scanners focused on minimum detectable concentration difference under various scan- and patient-related factors. Several other studies compared different scanner generations and vendors based on acquisition technique [72], iterative reconstruction, tube settings, and patient size [80], fluid characteristics of solvent, and influence of the iodine concentration itself [81]. These studies show that third-generation dual-energy CT (DE-CT) scanners outperform the second-generation models. The difference between single-source fast kV-switching and DE-CT in estimating IQ and VMI maps was found to have a small impact. The choice of reconstruction algorithm (*i.e.,* filtered-back projection or iterative reconstruction) and exposure level showed either insignificant or very minor impact [82, 83] on quantitative measurements. Most of the variability was introduced through non-controllable factors such as patient size, iodine concentration, solvent chemical composition, and misalignment of the phantoms with respect to the iso-center (patient positioning errors).

As we saw before, a new generation of CT scanners equipped with PCDs has reached clinical status. This started a new era of computed tomography since the process of data collection with PCDs is inherently different from energy-integrating detectors (EIDs). Images can be obtained with reduced noise while maintaining comparable or better spatial resolution. In other words, photon-counting CT is capable of delivering images of comparable or better quality at significantly reduced doses. While spectral imaging on earlier scanners is limited by the overlap of low and high-energy spectra, the approach of photon binning in PCD can potentially improve the accuracy of estimated quantities [45, 84]. During its development, the photon-counting approach to detection was extensively studied using simulation frameworks, bench setups, and prototype systems [85, 86, 87]. Rajendran et al. [88] performed one of the first technical evaluations of a clinical PC-CT scanner, demonstrating improved spatial resolution as well as the potential for lower radiation dose and image noise when compared to current state-of-the-art CT systems. Booij et al. [89] compared the contrast-to-noise ratio of an iodinated contrast agent in DE-CT and PC-CT at three different phantom sizes and several VMI levels. They demonstrated improved PC-CT performance only at VMI levels below 60 keV. They also discovered that using a tube voltage of 90 kV results in a higher CNR than using a tube voltage of 120 kV. Sartoretti et al. [90] conducted a comparison study in 30 patients using the same two scanners for iodine quantification in liver parenchyma and lesions. They demonstrated good iodine quantification accuracy regardless of radiation dose, iodine concentration, or base attenuation. Both studies found no significant differences in PC-CT and DE-CT [90] or minor differences in iodine-to-tissue CNR at low energy VMIs (40 - 60 keV) [89] at radiation doses recommended by diagnostic reference levels (DRLs). Decker et al. [91] published the first low-dose study in clinical PC-CT, demonstrating a statistically significant improvement in CNR and image noise in abdominal scans when compared to a second-generation scanner. This study demonstrated that PCD technology produces higher-quality images at lower doses, but it was not quantitative in the sense that VMI levels were not compared. Leeds et al. [92] provided a quantitative evaluation of multiple VMI levels between DE-CT and PC-CT Siemens scanners at low doses, reporting improved accuracy in a large phantom and significant reduction in electronic background noise. In both low-dose studies, the iodine quantification task was not evaluated.

In the following sections, we investigated the potential of PC-CT for low-dose quantitative spectral tasks on the NAEOTOM Alpha, a newly released CT scanner in the clinical environment. The scanner was evaluated against a clinical DE-CT scanner (Siemens Somatom FORCE) in VMI and IQ tasks. The study tested the accuracy of both Siemens scanners in estimating Hounsfield units (HU) and iodine concentrations of phantom inserts against the ground truth. Guided by the evidence from previous research [89, 83], scan-related parameters were closely matched, shifting the focus to patient-specific and the most influential parameters: phantom volume, material type, its location in the scanner, and also comparing the relevant concentration of iodine (2 mg/ml) in two different tissue backgrounds (solvents) - water and blood. The virtual monochromatic images were generated at energies of 40, 70, and 100 keV. The radiation dose used for image acquisition needed special consideration. Previous research on quantitative imaging in DE-CT scanners indicates optimal performance at current DRLs, but research PC-CT systems showed significant improvement in contrast-to-noise ratio at the same doses [93, 88]. Thus, in addition to routine dose levels, data in this study was collected at doses below the current diagnostic reference levels, according to the potential of the new technology. Moreover, using the combination of large phantom sizes and extra-low doses we explored the ranges within which quantitative imaging remains viable.

5.1 Experiment design

The experimental design developed for the comparison study between a dual-energy CT of the new generation and the first clinically approved photon-counting CT scanner is given in the following sections.

5.1.1 Phantom

The Multi-Energy 20-cm-diameter CT Phantom (Model 1472, Gammex Inc.) containing 9 different inserts that were used for this study is shown in Fig. 28. Inserts contained iodine (concentrations of 2, 5, and 15 mg/ml), calcium (50,100, and 300 mg/ml), and body tissues (brain and blood). Custom-made rings (each 5 cm in width) of fat-equivalent material were added to simulate the waist circumference (WC) of larger patients. There were a total of three rings, referred to as M, L, and XL sizes, designed according to the NIH practical guide to represent normal (WC: 90-100 cm), type-I, and type-II obese (WC: 110-130 cm), and extreme obese (WC: > 130 cm) patients.

Figure 28: The phantom with inserts used for data collection. The core is a commercial Multi-Energy CT Phantom (Model 1472, Gammex Inc.) while fat-equivalent rings were produced in-house to simulate different patient sizes.

5.1.2 CT scanners

Quantitative analysis was performed on two clinical scanners: Siemens FORCE and Siemens NAEOTOM Alpha. The FORCE scanner is representative of a third-generation dual-energy CT system, utilizing the latest energy-integrating detector technology. Spectral separation is enabled by two X-ray tubes which are simultaneously operated at different tube voltages. Thus, in spectral mode, the standard outputs of this system are ”low” and ”high” energy projections. The tube operating at higher energy has also a smaller field of view, limiting the quantitative analysis for very large patients. The NAEOTOM Alpha is a first-generation photon-counting CT scanner. It is a dual-source scanner with two CdTe photon-counting detectors with both tubes operating at the same voltage. The in-plane resolution in ultra-high mode reaches 0.125 mm [88], somewhat higher than the 0.30 mm in the FORCE scanner. In lower resolution ”standard mode”, spectral separation is possible by up to 4 energy levels, but in high resolution ”ultrahigh-resolution mode”, only two energy thresholds are available. It is worth noting that even when operating in standard mode by averaging the values in the 2-by-2 pixel neighborhood, the effective pixel size is still smaller than in the FORCE scanner. The reconstruction software uses an iterative reconstruction approach (Quantum Iterative Reconstruction, or QIR) different from the one that comes with the FORCE scanner (ADMIRE) and the standard output is always a VMI dataset. Sartoretti et al. [83] showed a reduction of up to 45 % in the global noise index between filtered back-projection and maximum QIR. This improvement didn't compromise the noise texture and mean attenuation values of measured regions. Thus, the iterative strength in the NAEOTOM Alpha scanner has no influence on quantitative values except for measurement standard deviation.

5.1.3 Acquisition and reconstruction

For each phantom size, we determined the required effective mAs to achieve CTDI$_{vol}$ values that align with our clinical quality reference mAs (QRM) for a routine abdomen pelvis exam. Given the desire to use the new technology for low-dose imaging, the clinical CTDI$_{vol}$ was then halved and quartered to give three dose levels. In this study, scanners were matched based on CTDI$_{vol}$ values and we refer to dose levels as standard, low, and extra-low doses. In addition, for each dose level, the phantom was shifted 5 cm in a vertical direction to ascertain the effect of variability in patient positioning on the results. The acquisition parameters used on both scanners are given in Table 2. In the DE-CT scanner, the low voltage tube was set to 80 kVp or 100 kVp and high to 150 Sn kVp[80, 86, 90], while for PC-CT both tubes were at 120 or 140 kVp, with the two thresholds set at 20 and 65 keV [94] and 20 and 70 keV, respectively. All scans were acquired at the pitch of 1.

The quantitative reconstruction kernel ”Qr40” was used with both scanners. The influence of iterative reconstruction strength was shown to be negligible in the presence of other patient-related

Table 2: Scan parameters of both scanners

Scanner model	Phantom size	CTDI$_{vol}$ (mGy)	Offset (cm)	Tube voltage (kVp)	Tube current (mAs)
Somatom FORCE	M	2.6, 5.2, 10.4	0;5	80/150Sn; 100/150Sn	18, 36, 73
	L	6.8, 13.6, 27.2	0;5	80/150Sn;100/150Sn	48, 95, 190
	XL	20, 40, 70	0;5	80/150Sn;100/150Sn	140, 280, 557
NAEOTOM Alpha	M	2.6, 5.2, 10.4	0;5	120; 140	19, 36, 73
	L	6.8, 13.6, 27.2	0;5	120; 140	43, 68, 172
	XL	20, 40, 70	0;5	120; 140	127, 253, 380

parameters in DE-CT [80, 79] and it also does not bias mean values in PC-CT [83]. Because QIR has 4 degrees of strength and ADMIRE has 5, we decided to use strength 3 for the NAEOTOM Alpha scanner (75 %, Syngo VA40) and strength 4 (80 %, Syngo VB10) for the FORCE scanner. All reconstructions were performed using a slice thickness of 2 mm, a field of view of 500 mm, and a matrix size of 512 × 512. The choice of VMI energy level is task-dependent and for non-contrast tasks, 70 keV images are a vendor standard output on NAEOTOM Alpha PC-CT. Besides 70 keV, images at lower energy (40 keV) and higher energy (100 keV) were rendered on both scanners to enable a full comparison. Ground truth values provided by the phantom manufacturer were calculated from the elemental compositions of the inserts. For iodine quantification, measured values exported in DICOM iodine maps were converted to units of iodine concentration (mg/ml) [79] using vendor calibration. Fig. 29 shows extra-low dose scans for qualitative comparison.

5.1.4 Statistical evaluation

An automated approach to data collection was implemented (Python, version 3.10.0) and statistical analysis was performed in dedicated statistical software (R, version 4.1.3). Pixel values were extracted from the 9 circular regions in each slice (16 mm in diameter). A total of 10 slices free from major artifacts were considered for each scan. All data acquired were initially separated into two groups according to scanner type. The association between measured and true values of iodine concentration and HU values across all scanner conditions was statistically evaluated using Pearson correlation. Experimental data were compared to ground truth values across different patient-related parameters using known material compositions provided by the phantom manufacturer. To assess the accuracy of measurements, the difference D = (mean measured value - true value) was computed for each region of interest (ROI) leading to a total of 90 values per scan. An uncertainty on the difference was reported using 95 % confidence intervals computed as 1.96 × standard error. Using D as the dependent variable and analysis of variance (ANOVA), the influence of each patient-related parameter (patient size, radiation dose, solvent type, and displacement from the iso-center) on the accuracy of each scanner was assessed. After the most significant sources of error were identified, further analysis was performed using posthoc Tukey honest significance (HSD) on the same dataset. The goal of this

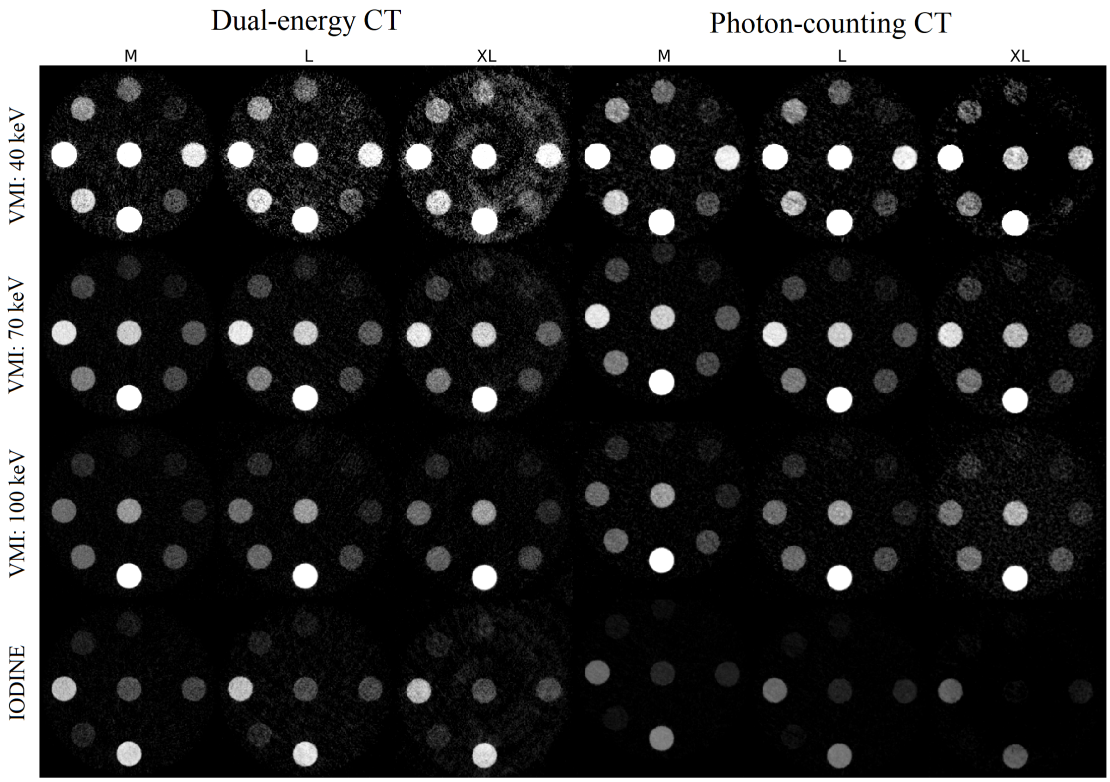

Figure 29: The extra-low dose phantom CT reconstructions from the DE-CT and the PC-CT scanner organized by size (M, L, XL) for three virtual monochromatic energy levels (40, 70, and 100 keV) and an iodine map. Scans are displayed with window width 0-500 HU and the orientation of inserts is the same as in Fig. 28

step was the pairwise comparison of groups within the selected patient-related parameter to estimate the influence of each group on the accuracy of measurement (D). To consider overall deviation from the ground truth, a virtual monochromatic scanner bias was estimated as:

$$MB = \sum_{i = 40,\, 70,\, 100\; keV} (\text{measured} - \text{true})_i \tag{68}$$

and an iodine scanner bias was defined as:

$$IB = \sum_{i = 2,\, 5,\, 15\; mg/ml} (\text{measured} - \text{true})_i \tag{69}$$

previously defined by Jacobsen et al. [78]. The results reported in this study were obtained at a $p <$ 0.01 statistical significance level.

Table 3: Analysis of variance

	Virtual monochromatic imaging		Iodine quantification	
	EID	PCD	EID	PCD
Quantitative task	19.15***	505.63***	–	–
Phantom size	288.64***	499.05***	220.61***	1934***
CTDI$_{vol}$	21.22***	0.61	5.35**	1.70
Material type	115.05***	77.42***	223.73***	294.34***
Displacement from iso-center	52.73***	0.22	15.68***	44.88***
Solvent	–	–	20.23***	9.17**

$^{***}p < 0$; $^{**}p < 0.001$; $^{*}p < 0.01$; $^{\cdot}p < 0.05$

5.2 Comparison results

5.2.1 Quantitative assessment of virtual monochromatic data

In our analysis, we obtained superior HU and iodine quantification accuracy for higher tube power setups (100/150Sn kVp and 140 kVp) in large and extra-large phantoms at low doses, and a comparable accuracy in the medium-size phantom. Thus, subsequent analysis was performed using higher voltage setups, and the raw data visualization for major patient-specific dependencies is shown in Fig. 30. The results of the Pearson test showed a statistically significant correlation between measured and the phantom manufacturer (true) HU values in both scanners. A slightly higher correlation coefficient of 0.993 was observed for the DE-CT scanner, versus 0.970 for the PC-CT scanner. The overall mean difference with 95% confidence interval for the combined contribution of all patient-related factors was 13 ± 2 HU for DE-CT and -28 ± 3 HU for PC-CT at all three VMI energy levels, 14 ± 4 and -83 ± 6 for 40 keV, 17 ± 1 and -1 ± 1 for 70 keV, and 10 ± 1 and 14 ± 1 for 100 keV, for DE-CT and PC-CT, respectively.

The analysis of variance revealed that the choice of monochromatic energy level in both scanners had a significant effect on the difference between actual and measured values. All patient-related parameters used in this study significantly affected the accuracy of HU values in the DE-CT, while in the PC-CT scanner, the radiation dose and the displacement proved insignificant for the virtual monochromatic imaging in tested conditions. The ANOVA results for VMI are shown in the first part of Table 3.

The posthoc Tukey pairwise comparison of the significant patient-related parameters is summarized in Fig. 31. The statistically significant difference in the pairwise comparison of dense material inserts containing calcium and high iodine concentrations against other materials was observed in both scanners (Fig. 31 a). The most obvious difference between the two scanners was observed in a pairwise comparison of dose levels: in the PC-CT scanner, there were no statistically significant differences between dose levels while in DE-CT significant differences were observed in the comparison of extra-low

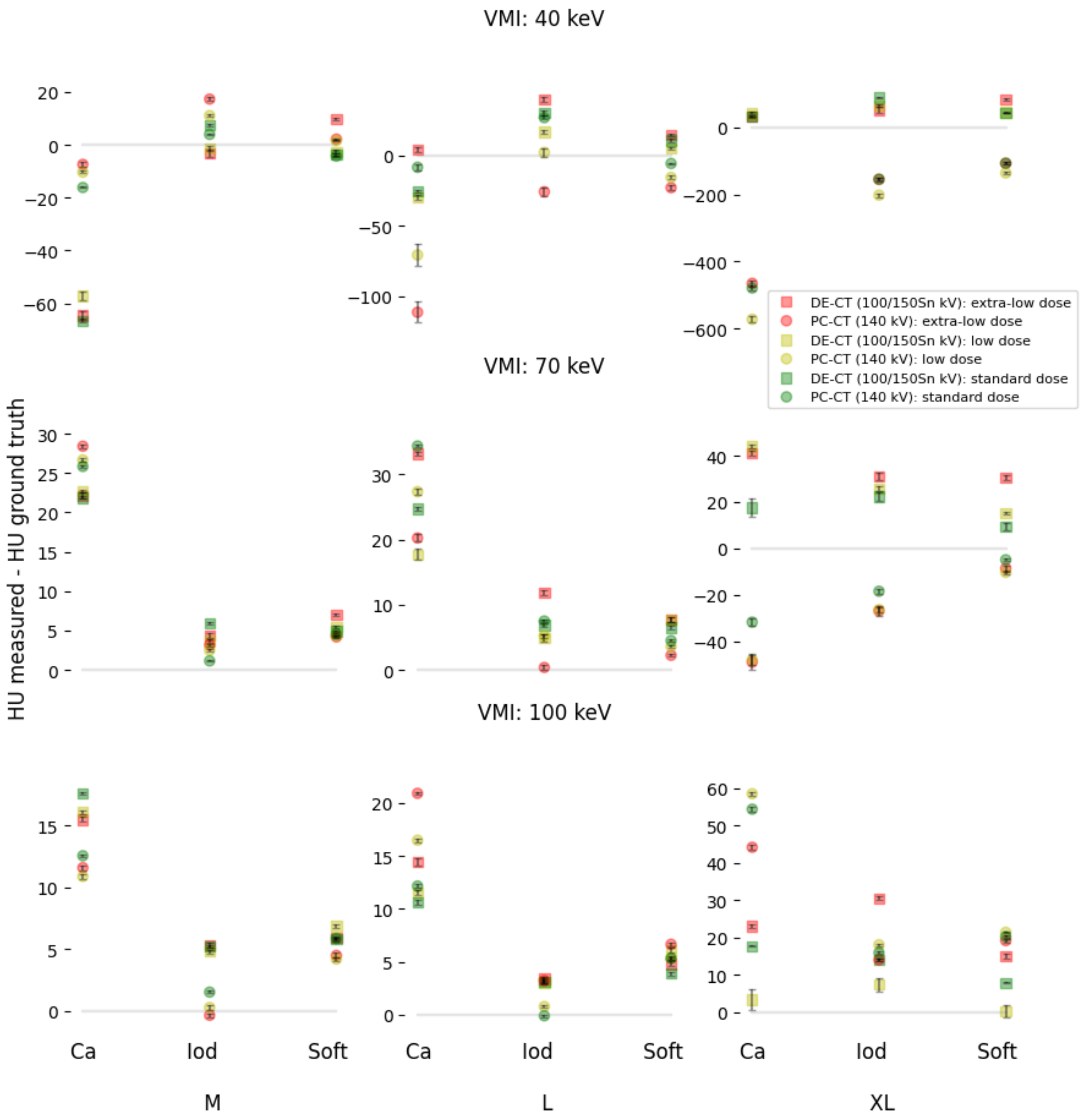

Figure 30: Comparison of the three virtual monochromatic levels (40, 70, and 100 keV) as deviations from the ground truth (*baseline equals no deviation*), for a combination of three patient-related factors (phantom size, dose, and material density), highlighting the difference between PC-CT and DE-CT. The data points represent the mean differences obtained from 10 different slices, while the error bars are the mean standard errors. Similar tissue inserts (soft, calcium, iodine), and values measured when the phantom was displaced from the iso-center were averaged together. Data points were grouped based on phantom size (M, L, XL), radiation dose (extra-low: red, low: yellow, standard: green), and material insert type.

dose levels and the other two higher dose levels (Fig. 31 b). The VMI levels significantly differed from each other, especially in PC-CT where the average accuracy D for 40 keV VMI level and XL phantom was -503 HU in calcium, -182 in iodine, and -117 in soft inserts (given in more detail in the Appendix). The mean difference between all sizes in both scanners was statistically significant, but a major increase in mean difference was associated with the extra-large phantom size.

The monochromatic bias was characterized for each VMI level according to the formulation given in Sec. 5.1.4 and shown later in Fig. 34. The results demonstrated the opposite overall MB of 40

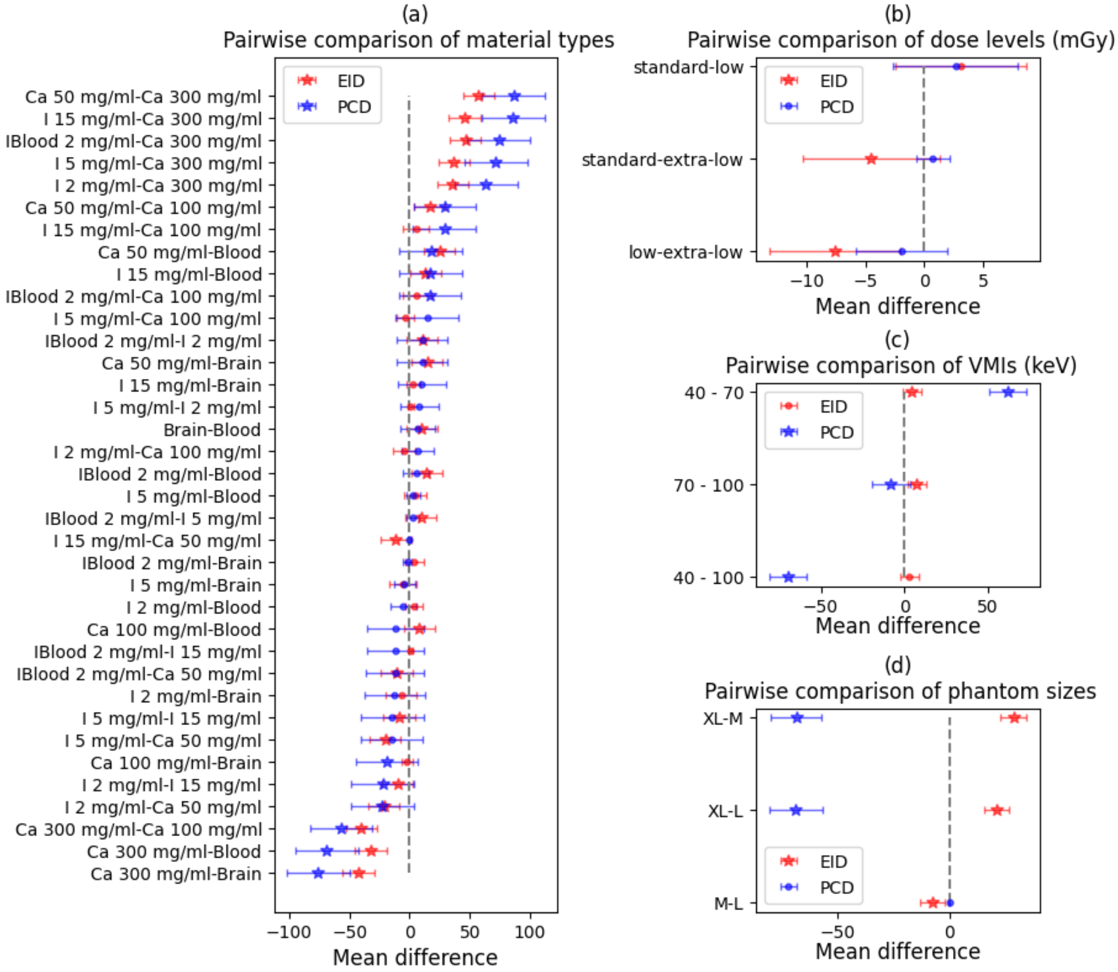

Figure 31: Tukey pairwise comparisons of groups within each statistically significant patient-related parameter for the virtual monochromatic imaging task are presented with 95% family-wise confidence intervals. Panels show a comparison of mean differences of accuracy (D) between material types (a), dose levels (b), VMI levels (c), and phantom sizes (d). Star shapes (⋆) mark the statistically significant mean differences of accuracy (D), while circles show insignificant pairwise mean differences.

± 5 HUs in DE-CT and -83 ± 7 in the PC-CT scanner. A major contribution to a negative bias in the PC-CT scanner was driven by the underestimation of HU values at 40 keV virtual monochromatic images, especially in dense phantom inserts (Ca 300 mg/ml and iodine 15 mg/ml).

5.2.2 Quantitative assessment of iodine quantification

Measured iodine concentrations showed a statistically significant correlation with ground truth values in both scanners for the task of iodine quantification. The Pearson correlation in PC-CT (0.89) was significantly higher than in DE-CT (0.80). Visual inspection of the data revealed that patient-related parameters have a lower influence on the accuracy and stability of measurements in the PC-CT scanner. For the iodine quantification task, a comparison between the two scanners is shown in Fig. 32. Data were sorted by the level of iodine concentration, radiation dose, and phantom size.

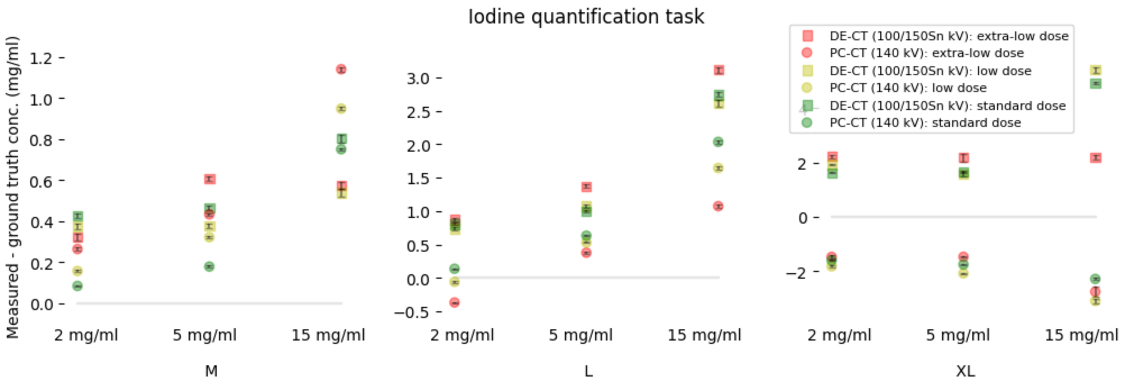

Figure 32: Comparison of measured iodine concentrations to the ground truth, highlighting the difference between PC-CT and DE-CT for respective tube configurations 140 kVp and 100/150Sn kVp. The data points represent the mean differences obtained from 10 different slices, while the error bars are the mean standard errors. All data points were grouped by phantom size (M, L, XL), radiation dose, and level of iodine concentration (2, 5, and 15 mg/ml). Iodine inserts at 2 mg/ml for two different tissue backgrounds (water and blood), and values measured when the phantom was displaced from the iso-center were averaged together.

The overall mean difference when all patient-related factors influencing the iodine quantification task were taken into account was 1.57 ± 0.04 mg/ml in the DE-CT and -0.30 ± 0.02 mg/ml in the PC-CT, with significant differences between DE-CT and PC-CT. The mean difference increased with the phantom size, 0.50 ± 0.03 and 0.47 ± 0.01 for M size, 1.59 ± 0.06 and 0.67 ± 0.03 for L size, and 2.63 ± 0.13 and -2.04 ± 0.11 for XL size in DE-CT and PC-CT respectively. The complete ANOVA and Tukey pairwise comparison results are shown in Table 3, that is Fig. 33.

The results of the analysis of variance indicate that phantom size, iodine concentration, phantom displacement from the iso-center, and solvent type (water or blood) are significant parameters for both scanners. However, the radiation dose only affects the DE-CT scanner and not the PC-CT scanner. Further analysis using Tukey pairwise comparison within the significant groups reveals that there is a significant difference in means between high (15 mg/ml) and lower (2 and 5 mg/ml) iodine concentrations in both scanners. This difference is more pronounced in the DE-CT scanner than in the PC-CT scanner (as shown in Fig. 33 a). Additionally, there were no significant differences in means obtained at extra-low, low, and standard doses for the iodine quantification task in the PC-CT scanner (as shown in Fig. 33 c), as was the case for the VMI task. However, in the DE-CT scanner, measurements obtained at the standard dose were statistically different from the lower doses. The mean difference in the extra-large phantom size is significantly different from the medium and large sizes in both scanners (as shown in Fig. 33 d).

Based on these statistical results, the iodine size bias was characterized for each iodine concentration according to equation 68 and is shown in Fig. 34.

The iodine quantification bias of -0.9 ± 0.15 was significantly lower in PC-CT compared to IB of 4.72 ± 0.22 in DE-CT.

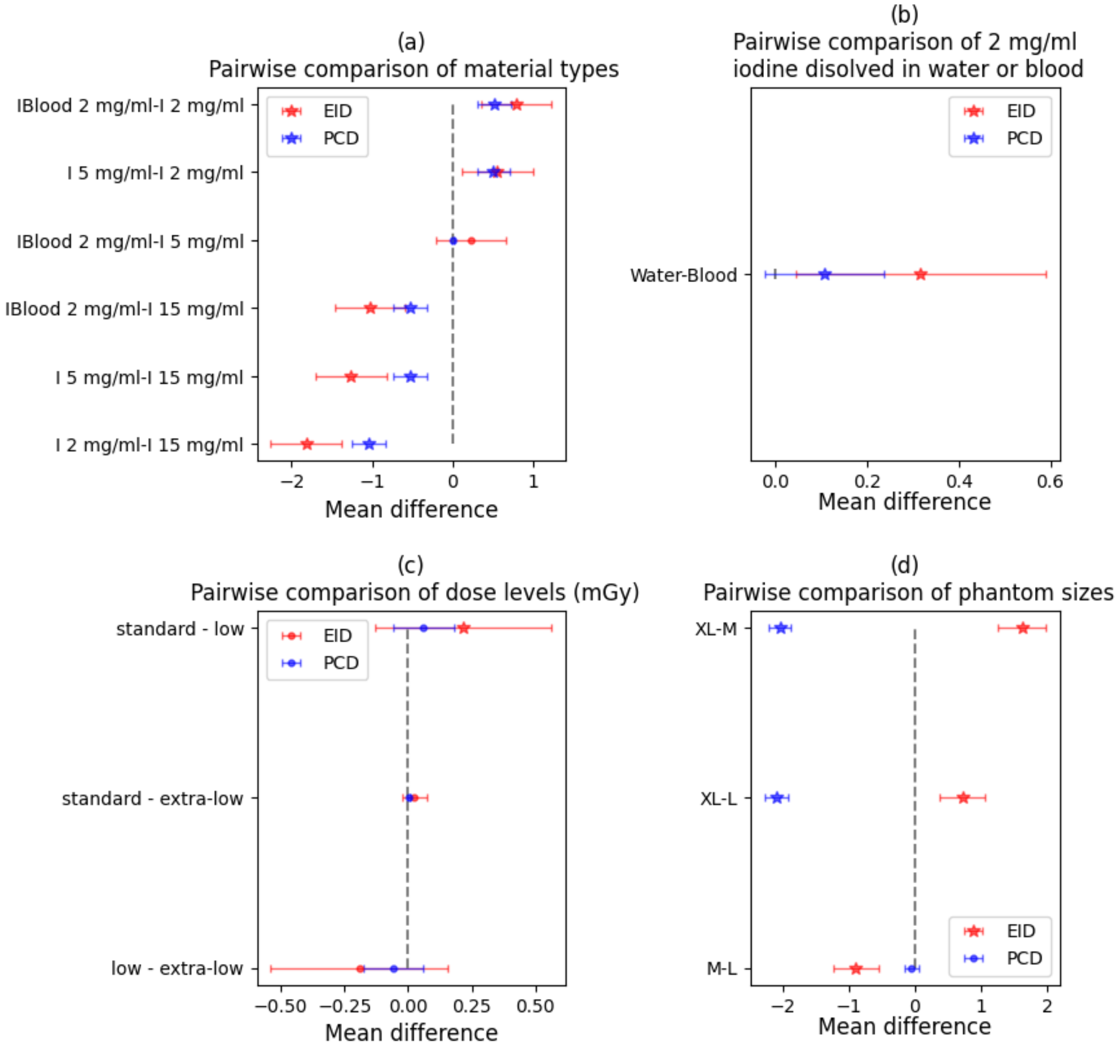

Figure 33: Tukey pairwise comparisons of elements within each statistically significant patient-related parameter for the iodine quantification task are presented with 95% family-wise confidence intervals. Panels show a comparison of mean differences of accuracy (D) between iodine concentration (a), tissue backgrounds (b), dose levels (c), and phantom sizes (d). Star shapes ($\star$) mark the statistically significant differences in the observed mean differences.

5.3 Discussion of comparison results

Spectral CT scanners offer new opportunities in quantitative imaging through virtual monochromatic images and iodine quantification. These methods are useful for a variety of clinical tasks, including tumor, staging, and tissue differentiation. To be considered fully quantitative they must be accurate, precise, and repeatable. Numerous studies on early-generation scanners have been conducted, testing the influence of many scan- and patient-related parameters on the accuracy and precision of VMI and IQ. Through their inherent ability to differentiate the energies of detected photons, paired with uniform spectral weighting and low electronic noise, a new generation of CT scanners with photon-counting detectors offer new potential for spectral imaging. However, studies by Sartoretti et al. [90, 83]

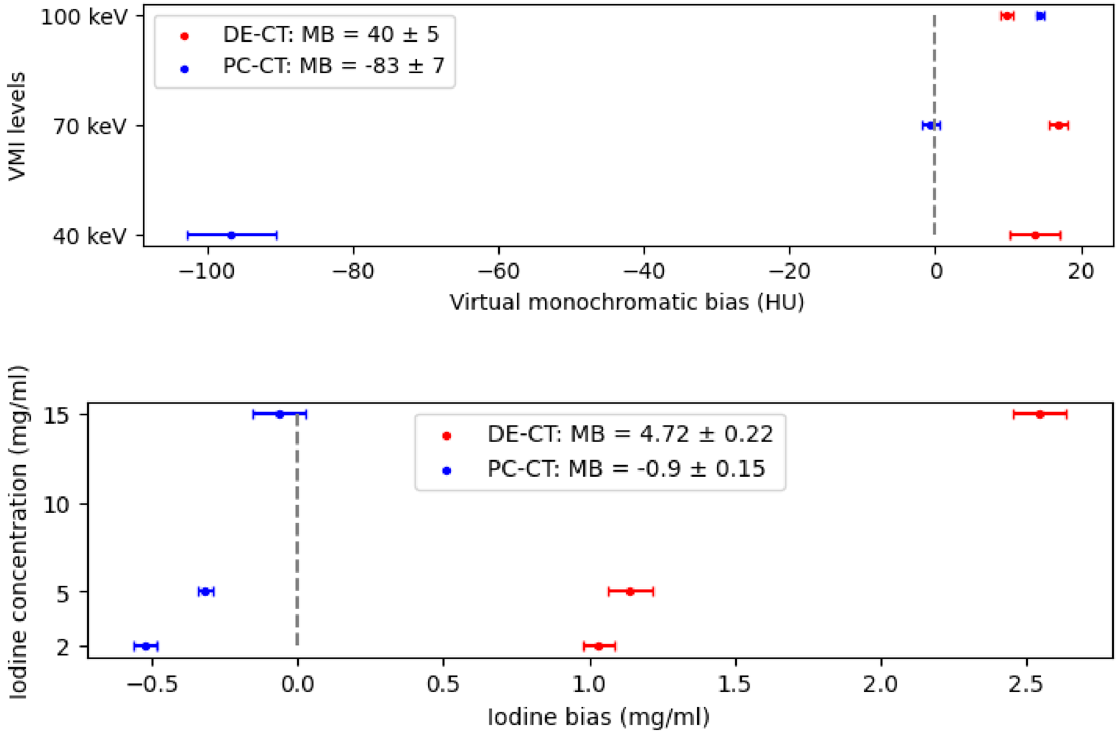

Figure 34: Scanner bias: VMI and iodine bias computed using equations 68 and 69, respectively. The horizontal lines show the 95% confidence intervals.

and Booij et al. [89] found little or no difference in quantitative performance at doses comparable with DRLs, whereas Rajendran et al. [88] and Decker et al. [91] obtained statistically significant improvement in CNR at low dose range. Leening et al. [95] performed a quantitative evaluation of VMI levels at low doses, stating that PC-CT outperforms DE-CT in given conditions. The purpose of this study was to compare the advantages of photon-counting versus energy-integrating detection in quantitative imaging with two representative clinical CT scanners under the influence of major patient-related factors such as patient size, radiation dose, patient positioning, iodine concentrations, and their dissolving environment at very low dose levels. Compared to other similar studies [91, 92], in addition to VMI performance evaluation, we evaluated the iodine quantification task and included more patient-related parameters and analyzed cases where quantitative imaging becomes extremely difficult such as in extremely obese patients at low doses.

Using the ANOVA we found that low-dose quantitative imaging was significantly affected by most patient-related parameters in both scanners. However, the radiation dose did not significantly affect the accuracy of quantitative imaging in the PC-CT scanner. The PC-CT scanner showed an obvious improvement in the iodine quantification task, as iodine concentrations could be estimated with good accuracy (D = -0.30 ± 0.02 mg/ml) and small bias (-0.90 ± 0.15 mg/ml), while the accuracy of VMI was comparable at higher VMI levels (in agreement with previous studies) but degraded in the 40 keV virtual images. The VMI bias was higher and the iodine bias was lower in the PC-CT than in the DE-CT scanner in our study. For the iodine quantification task, some of the results of this study can be compared to the findings of Sartoretti et al. [90]. For the identical phantom circumferences (M size phantoms in both studies) the dose levels ($\text{CTDI}_{vol} = 15$, 10, and 5 mGy) were on average 1.7× higher than in our study. The reported iodine error in the PC-CT scanner ($|\text{D}| = 0.32 \pm 0.39$) was comparable to the one obtained in the PC-CT scanner in our study (0.30 ± 0.02 mg/ml), and in the DE-CT scanner ($|\text{D}| = 0.36 \pm 0.31$) the reduction of the dose severely affected the accuracy of iodine quantification (1.57 ± 0.04 mg/ml) in our study. Iodine quantification bias results were compared to the largest study [78] evaluating the most widespread dual-energy scanners from different vendors. The dose reported in their study was on average 1.6× higher for nearly matching phantom sizes (elliptical phantom 40×30 cm versus the L size phantom of diameter 40 cm) and the iodine inserts used in both studies were of the same concentration. The iodine bias range obtained from several dual-energy scanners (-2.6 to 1.5 mg/ml) was comparable to the iodine bias in PC-CT (-0.9 ± 0.15 mg/ml) but not with the bias in DE-CT (4.72 ± 0.22 mg/ml) scanner used in our study. Therefore, iodine quantification at very low doses in PC-CT produces a comparable accuracy and bias to that of dual-energy scanners at DRLs, but the reduction of dose in the same DE-CT scanner type significantly increases the iodine bias. The comparisons with the previous studies further corroborate our result that radiation dose was not a statistically significant factor in the PC-CT scanner for the iodine quantification task.

The size of the phantom was the most influential factor when estimating both quantitative maps. The size factor has been investigated before [96] and some vendors have implemented a size-dependent calibration factor that re-scales the iodine concentrations based on the effective size of the patient. The main effects influencing the accuracy at increased phantom size are the combined effects of photon starvation and energy weighing of the signal inside the detector. Because photon starvation is energy-dependent (beam hardening effect), the improved spectral weighting of low-energy photons in photon-counting detectors becomes even more important in the imaging of large and dense objects at low doses. The combined effect of beam hardening and sub-optimal energy weighting has a particular influence on iodine quantification because the most prominent feature of iodine, its K-edge, is located at the low end of diagnostic energy spectra (33.2 keV). Indeed, the mean differences in the Tukey pairwise comparisons were the largest between low and high iodine concentrations and between medium and larger phantom sizes. For comparison, iodine quantification accuracy for M and L size phantom is comparable in PC-CT ($\text{D} = 0.47 \pm 0.01 \rightarrow \text{D} = 0.67 \pm 0.03$), while a significant drop in accuracy is observed in DE-CT for the two sizes ($\text{D} = 0.50 \pm 0.03 \rightarrow \text{D} = 1.59 \pm 0.06$). However, when photon statistic becomes very low such as in XL size phantom, both scanners exhibit low iodine quantification accuracy. Because the L and XL phantom sizes used in this study are representative of obese and severely obese patients and at the same time they make up nearly 42 % and 10 % of the US adult population (NHANES 2017-18), our results suggest improved quantitative imaging performance in PC-CT for the substantial part of US population.

The virtual monochromatic imaging task is different from the iodine quantification task in that the basis materials used for material decomposition usually don't contain a K-edge. An advantage of improved photon statistics at very low energies in the PC-CT scanner (due to improved weighting of low energy photons) that is crucial for the iodine quantification task, seems to diminish in the VMI tasks for the condition of low-dose-obese patient imaging, especially for the estimation of bone VMI HU values and other dense tissues. Overall, the DE-CT scanner HU accuracy for all VMI levels (13 ± 2 HU) was within the range (11.4–52.0 HU) reported in prior studies [78], and compared to these values the PC-CT scanner showed similar accuracy (-28 ± 3 HU) but in opposite direction. Further investigation revealed that the significant negative bias (-83 ± 3 HU) was driven by an underestimation of 40 keV HU values in XL phantom (top-right Fig. 30), particularly in high-concentration calcium and iodine inserts (see Appendix A). Leening et al. reported larger deviations from the ground truth in 40 keV images compared to higher virtual monochromatic levels for both PC-CT at 120 kVp and DE-CT at 100/150Sn kVp scanner. Since we used much larger patient sizes (L and XL) and denser inserts (calcium 100 and 300 mg/ml and iodine 15 mg/ml), the accuracy of estimating HU values at 40 keV was significantly reduced in PC-CT. Previous studies found that an increase in tube potentials in DE-CT benefits virtual monochromatic imaging at low doses, despite decreased spectral separation and decreased attenuation difference between basis materials. Perhaps, following the same logic, PC-CT scanners could benefit from increased tube potentials and/or threshold optimization for the specific case.

The analysis of the influence of the dissolving environment on the accuracy of iodine estimation in the two special inserts of 2 mg/ml with different body fluids backgrounds showed statistically significant differences in both scanners. The insert containing blood produced consistently higher iodine concentration measurements and positive iodine bias in both scanners. This is because blood contains a certain amount of iron, which can erroneously mimic iodine-induced attenuation. Thus, it is worth noting that the true iodine concentration in blood could be slightly lower compared to the measured values. Lastly, the offset of 5 cm from the iso-center didn't cause any differences in virtual monochromatic imaging performance in the PC-CT scanner, but it was significant for iodine imaging and for both quantitative tasks in the DE-CT.

Irrespective of spectral performance, to complement the picture one should consider the level of noise and resolution of both scanners. For the exact two scanners (study done in the same institution [97]), it was found that PC-CT exhibits similar or better noise, contrast, and CNR than DE-CT when comparing kernels with similar names. Sharp kernels on PC-CT had lower resolution than DE-CT's sharp kernels.

Some of the limitations of our study should be noted. We performed this study on phantoms, thus, results may slightly differ in actual patients. Our study covered a wide range of patient-related parameters relative to clinical practice but we mostly focused on low-dose performance. Although we had different levels of iodine concentration, we didn't estimate a minimal detectable concentration difference [79] due to the lack of suitable inserts. Although expected to be minimal, some differences in results could exist due to the difference in smoothing kernel implementation and reconstruction software version. Finally, in the case of larger phantoms (*e.g.,* L and XL), it's important to note that the comparison between DE-CT and PC-CT might not be entirely fair. This is because DE-CT employed a higher tube voltage of 150 keV (with Sn filter), whereas the PC-CT scanner used 140 keV. It's worth mentioning that both settings represented the maximum voltages available on their respective machines. In clinical scenarios with patients of similar sizes, the recommended clinical protocols advise utilizing the highest tube potential.

According to our statistical analysis, photon-counting CT has the potential to achieve better quantitative performance at lower radiation doses. Our study found that the Siemens NAEOTOM Alpha PC-CT scanner showed comparable accuracy in iodine and VMI imaging between low and standard radiation dose levels. In contrast, the DE-CT scanner's performance was affected by radiation dose levels and showed reduced accuracy at lower radiation doses. The PC-CT scanner outperforms the DE-CT scanner in the iodine quantification task in all cases. The accuracy of virtual monochromatic imaging is comparable between scanners for normal and obese patients, but in extreme cases of very large patients and dense material inserts, DE-CT seems to benefit from the increased tube potential configurations available on the system, outperforming the PC-CT scanner.

6 Synchrotron spectral breast CT - density and effective atomic number

Tissue differentiation in mammography is challenging due to the overlap of tissues with similar linear attenuation coefficients μ in the diagnostic energy range. A comparison of the attenuation of glandular tissue and close-by malignant tumors found that the average attenuation values are almost identical even in the low-energy range [98, 99]. Computed tomography (CT) solves tissue overlapping issues and provides additional diagnostic information based on tissue morphology in 3D volumes. On the other hand, breast-dedicated CT uses higher X-ray energies than mammography due to the imaging of uncompressed breasts, thus reducing attenuation contrast between similar tissues. Tissue separation can be significantly improved by acquiring data at multiple energy levels using spectral CT imaging [5]. As we established before, photon-counting detectors are particularly interesting due to the availability of multiple energy thresholds (up to 12 [84]), flat spectral response, and low imaging noise. The first breast CT scanners with PC detectors are being introduced in clinics [100, 101, 102, 103] and synchrotron facilities [104, 105], where spectral separation can be obtained using multiple monochromatic X-ray beams. Despite the available technology for spectral imaging in both systems, the benefits of such an approach in breast CT imaging have not been explored yet.

Spectral data representation through material decomposition into two basis materials is the most common approach because two physical effects contribute to image formation in the diagnostic energy range: the photoelectric effect and Compton scattering. The photoelectric-Compton basis itself is very convenient because of the well-defined dependencies of these effects on density and atomic number. However, such basis spans an infinite range of physical materials, given that a “purely Compton” material would be the element in the limit Z $\rightarrow 0$, while a “purely photoelectric” one would correspond to Z $\rightarrow \infty$. Such a broad range would degenerate the separation of similar materials, such as soft tissues. To address this issue, the use of a pair of physical (or even virtual) materials that span the range of materials of interest has been shown to significantly reduce decomposition uncertainty [30]. A popular choice of physical materials for decomposing biological tissues are polymethyl-methacrylate (PMMA) and aluminum (Al) basis pair [106], also used in this study. Estimated weights of the linear combination of two basis materials carry physical information but have no particular comprehensive meaning except when one of the basis materials is the same as the material of interest (e.g. iodine quantification or calcium scoring). However, using the weights and the known energy dependence of basis attenuation coefficients virtual monochromatic images (VMIs) can be extrapolated at an arbitrary energy value within the diagnostic energy range [107]. VMIs have simple interpretation and clinical case studies show that virtual monochromatic images are diagnostically valuable for certain tasks [67], and they are a standard output in the first clinical whole-body PC-CT (Naeotom Alpha, Siemens) [108].

In the present research, a spectral study was specifically designed to characterize breast CT images in terms of material density ρ and the effective atomic number Z_{eff}. While ρ/Z_{eff} decomposition has been implemented in some clinical CT scanners [109], no studies specifically focused on breast tissue characterization were performed. In section 6.1.1, a theoretical approach to computing ρ and Z_{eff} values from physical material decomposition instead of the photoelectric-Compton decomposition was developed to improve the accuracy of results. Using synchrotron X-ray beams at several energies and a high-resolution PCD described in section 6.1.2, CT scans of a dedicated phantom and 5 mastectomy samples were acquired. Due to the superior imaging quality and spectral separation available with synchrotron setup, the work investigates the feasibility and the potential diagnostic benefit of $\rho/\mathrm{Z}_{\text{eff}}$ decomposition in breast CT imaging. This information is of interest since PCDs matured enough to operate in clinical conditions with the ability to obtain better spectral separation than other approaches mentioned earlier [84]. The introduced concept of effective atomic number was further investigated in section 6.1.3. Section 6.1.4 describes tissue preparation and section 6.2 provides a detailed explanation of the practical realization of the analysis with careful consideration of the well-known problem of the decomposition noise [16, 110, 111]. Finally, the data analysis approach is given in 6.3. We also showed that virtual monochromatic μ values at desired energy can be computed using the known dependence of X-ray attenuation on density and atomic number.

6.1 Experiment design

6.1.1 Theoretical model

In the first step of our method, we performed material decomposition to determine the coefficients x_1 and x_2. Because more than two spectral scans were available for each sample [112], instead of using traditional matrix inversion [113], x_1 and x_2 coefficients were calculated by using a least-square fit approach described in equation 29. Using the dependence of the linear attenuation coefficient on PE and CE as stated in equation 47 to describe basis materials in equation 23 and once again assuming $A = 2Z$, as it is almost true for any chemical element with $Z \lesssim 20$, the linear combination coefficients of equation 23 read

$$x_1 = \frac{\rho\, Z_1 (Z^n Z_2 - Z\, Z_2^n)}{\rho_1 Z \left(Z_1^n Z_2 - Z_1 Z_2^n\right)} \tag{70}$$

$$x_2 = \frac{\rho\, Z_2 (Z\, Z_1^n - Z^n Z_1)}{\rho_2 Z \left(Z_1^n Z_2 - Z_1 Z_2^n\right)} \tag{71}$$

ρ_j and Z_j being the density and the atomic number of the j-th basis material. It is straightforward to notice that equations 70 and 71 depend on both the density and the atomic number of the material. In order to decouple the two dependencies, it is necessary to rotate the reference frame (by an angle $\phi = \arctan\left(\frac{\rho_2}{\rho_1}\right)$) and then rescale the second coordinate dividing it by the first one. The resulting coordinates, which read

$$x_\rho = \frac{\rho}{\sqrt{\rho_1^2+\rho_2^2}} \tag{72}$$

$$x_Z = \frac{Z^\ell\left(\rho_1^2+\rho_2^2\right)-\left(Z_1^\ell\rho_1^2+Z_2^\ell\rho_2^2\right)}{(Z_2^\ell-Z_1^\ell)\rho_1\rho_2} \tag{73}$$

(with $\ell = n-1$) are labeled x_ρ and x_Z because of their exclusive dependencies on the variables mentioned in the subscripts. Equations 72 and 73 represent the expected relationships between x_ρ and ρ, and between x_Z and Z, for a given choice of basis materials. Such expressions are used in the calibration procedure described in section 6.4.1, where the (known) densities and atomic numbers of reference materials will be fitted against the corresponding (measured) values of x_ρ and x_Z using the functional forms

$$x_\rho(\rho) = \kappa\,\rho \tag{74}$$

$$x_Z(Z) = p\,Z^\lambda + q \tag{75}$$

stemming directly from equations 72 and 73 with the (physically motivated) coefficients replaced by the effective fit parameters κ, λ, p, and q. The resulting calibrated relationships map the measured x_ρ and x_Z of any imaged material onto its actual values of density and effective atomic number.

6.1.2 Scan setup

The experimental image acquisition was carried out at the SYRMEP beamline of Elettra, an Italian synchrotron light source in Trieste, in the framework of SYRMA-3D (SYnchrotron Radiation for MAmmography) collaboration [105]. The SYRMEP beamline utilizes a laminar beam having a cross-section at the detector equal to 148.5 mm (horizontal) × 3.25 mm (vertical), while the energy is selected through a Si double-crystal (1,1,1) monochromator with a resolution around 0.1%. To perform tomographic acquisition the sample was positioned on a rotation stage spinning at a constant speed of 4.5 degrees/s while 1200 projections were acquired over 180 degrees. The imaging detector was a large area high-resolution CdTe photon-counting device (Pixirad8) featuring a honeycomb matrix of 4096 × 476 pixels with a 60 μm horizontal and 52 μm vertical pitch [114, 115]. It was positioned

~1.6 m from the sample to employ the propagation-based phase-contrast imaging technique. The source-to-sample distance was 30 m, leading to a magnification factor of 1.05. Acquired projections were pre-processed with an ad-hoc procedure [116] and then phase-retrieved using an algorithm based on the homogeneous transport of intensity equation (TIE-Hom) [51]. Finally, CT reconstructions were obtained via a GPU-based filtered-back-projection algorithm with Shepp-Logan filtering [117]. It is worth noting that, despite being a product of phase retrieval, reconstructions are maps of the attenuation coefficients μ at a given energy, as thoroughly explained in [50, 53, 112].

6.1.3 Calibration phantom and effective atomic number

A custom-made cylindrical phantom with a 10 cm diameter dedicated to calibration and quality control of the synchrotron breast CT system was used [118, 119]. The phantom was filled with water and contained five inserts of polyethylene (PE), nylon (PA), PMMA, polyoxymethylene (POM), and polytetrafluoroethylene (PTFE) mimicking soft tissues of similar attenuation properties. The density of each material was known and the effective atomic number was computed from the material composition. Comparison between the methods using the open-source GUI software "Z*comp*ARE" [31] software is analyzed in Appendix B, showing that depending on the method chosen, Z_{eff} number can take different values for the same compound. However, any choice of the method led to a unique material description on a chosen basis. Quantity x_Z derived in section 6.1.1, was simply calibrated to the desired definition of effective atomic number for a compound by putting $Z = Z_{\text{eff}}$ in equation (75). In this paper, we used the approach by Champley *et al* [30] which defines Z_{eff} of a compound as a linear combination of two consecutive Z numbers such that the least square error between X-ray transmission of the compound and the transmission of a combination of the two elements is minimized. Compounds' brute formula, density, and Z_{eff} are given in table 4. The phantom served two purposes: *i)* to obtain the ρ and Z_{eff} calibration curve from the decoupled set in equations (72) and (73) and *ii)* to validate the theoretical model against the ground truth.

Table 4: List of materials composing the phantom together with chemical formulas, effective atomic numbers, and material density values [33].

Material	**Water**	**PE**	**PA**	**PMMA**	**POM**	**PTFE**
Brute formula	H_2O	C_2H_4	$C_{12}H_{22}N_2O_2$	$C_5H_8O_2$	CH_2O	C_2F_4
Effective Z	7.44	5.28	6.16	6.49	7.01	8.56
Density (g/cm^3)	1.0	0.94	1.14	1.19	1.425	2.2

6.1.4 Breast mastectomy samples

In addition to phantom scanning, post-mastectomy breast tissue images were analyzed in a retrospective study. The analyzed surgical samples (N=5) were fixed in formalin, sealed in a vacuum bag, and conserved at 4 °C. The preliminary analysis of the same data was published [112] as a feasibility study of the synchrotron breast CT approach. All the procedures adopted in this work followed Directive 2004/23/EC of the European Parliament and of the Council of 31 March 2004 on setting standards of quality and safety for the donation, procurement, testing, processing, preservation, storage, and distribution of human tissues. In the present work, we further processed the data to extract ρ and Z_{eff} of breast tissues. Tomographic reconstructions of selected samples are given in Fig. 35. They all contained adipose, fibro-glandular, and tumorous tissue, but only in sample 4 existed a region of glandular tissue clearly separated from the fibrous. It also contained calcification regions that were not evaluated in this study. All samples contained some type of malignant tissue: Samples 1, 2, and 3 contain infiltrating ductal carcinoma, Sample 4 contains infiltrating ductal carcinoma with a core of desmoplastic tissue, and Sample 5 contains vastly differentiated infiltrating ductal carcinoma. Samples 1,2,4, and 5 also contained portions of the skin. The mean glandular dose of 5 mGy delivered per scan was computed according to a dedicated Geant4 Monte Carlo simulation [120, 121]. The phantom scans were acquired at 25, 28, 32, and 35 keV, and mastectomy samples at several monochromatic beam energy levels in the range of 24 - 38 keV, from which three scans were selected for the spectral analysis.

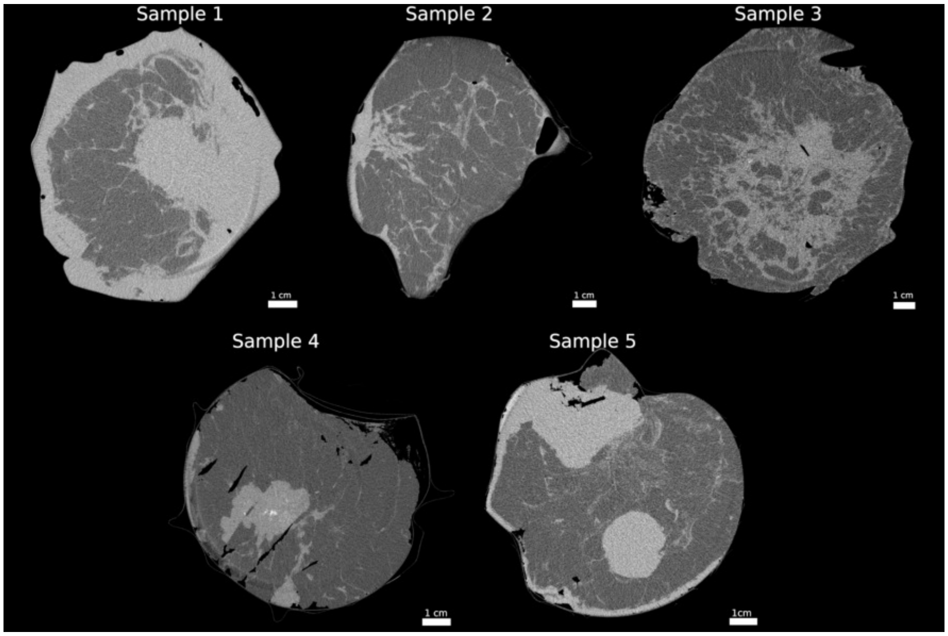

Figure 35: Mastectomy CT reconstructions acquired at SYRMEP beamline at Elettra Sincrotrone Trieste at the energy of 28 keV (Sample 1,2,3, and 5) and 26 keV (Sample 4).

6.2 Practical implementation

The theoretical model described in section 6.1.1 was implemented with Python (Python 3.10.0) and an interactive delineation tool was developed to select an arbitrary region of interest (ROI) within a reconstructed spectral data set (Matplotlib, Python 3.10.0) containing a single tissue type. In the first step of the process (framed with a dashed line in Fig. 36), the voxel-to-voxel material decomposition method using the PMMA-Al basis is applied to the selected regions (Fig. 36(a)), resulting in PMMA and Al maps for each ROI (Fig. 36(b)). In the next step, the material maps are combined in 2D histograms, one for each tissue type (Fig. 36(c)). In literature, this approach to material visualization is often referred to as CT fingerprinting [109]. Due to the presence of noise, the obtained histograms are blurred and elongated. The correct decomposition coefficients x_1 and x_2 are considered to be the centers of obtained distributions. They are extracted using a 2D Gaussian fit method of the form:

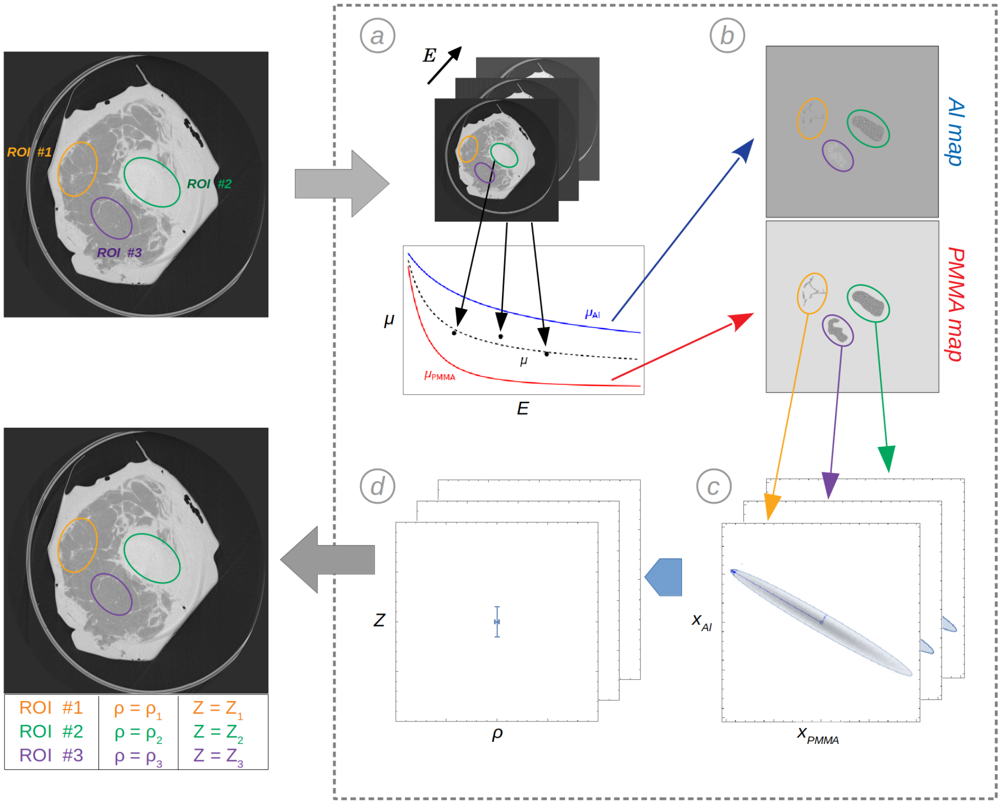

Figure 36: The step-by-step scheme of quantitative material evaluation followed in this work. Inputs to the algorithm (dashed rectangle) are delineated tissues. Section *a* shows the material decomposition task which leads to material maps in section *b*. These maps are represented in form of a 2D histogram and centers of clusters corresponding to each delineated material are extracted in section *c*. These values are then transformed using equations 72 and 73 and an offline calibration using materials from table 4 is performed in section *d* to obtain the ρ and Z_{eff} values as a final output.

$$G(x_1, x_2) = A\, e^{\left(-\frac{u^2}{2\,S_u^2} + \frac{v^2}{2\,S_v^2}\right)} \tag{76}$$

A is the intensity of the peak and S_u, S_v the spreads (that is, the standard deviations of the associated distributions) along the major and minor axes, respectively. The peak coordinates $\bar{x}_1$ and $\bar{x}_2$ relative to (x_1, x_2)-plane of the histogram are contained in the quantities u and v,

$$u = (x_1 - \bar{x}_1)\,\cos\theta + (x_2 - \bar{x}_2)\,\sin\theta \tag{77}$$

$$v = (x_2 - \bar{x}_2)\,\cos\theta - (x_1 - \bar{x}_1)\,\sin\theta \tag{78}$$

θ is the tilt of the major axis of the spot with respect to the horizontal direction. After the fitting, the peak coordinates $\bar{x}_1$ and $\bar{x}_2$ found according to equations (77) and (78) are used in equations (70) and (71) to compute the final output of the procedure: the single values for densities and effective atomic numbers of selected tissues (Fig. 36(d)). The measurement uncertainty, estimated as the standard error on the center of fitted 2D Gaussian distribution, is propagated through all mathematical transformation steps and measurement calibration. For the sake of conciseness, the complete analysis is given in the B.

6.3 Data analysis

In addition to the experimental data obtained using the calibration phantom, the procedure described in the theoretical model (section 6.1.1) was also applied to published μ ("true") values [33] of phantom material inserts at the energy levels used in the experiment. The true data points are used to evaluate the accuracy of the model by calculating the percentage error between the experimental and the ground truth data points, as given in equation 79.

$$\%\,error = \frac{|\text{ground truth - measured}|}{\text{ground truth}} \times 100 \tag{79}$$

The segmentation of the breast CT reconstructions were performed by an experienced radiologist, who selected ROIs containing adipose, fibro-glandular, glandular, skin, and tumorous tissue already knowing the mastectomy content from specimens sampled for the histological examination. Considering magnification, slices were reconstructed with 0.057×0.057 mm pixel size and slice thickness of 0.049 mm. The segmentation was done slice by slice to extract values from a 3D volume, using at least 3 pixel thick (0.17 mm) margins to avoid partial volume effects. For each sample and tissue type, density and Z_{eff} values and their uncertainties were estimated respectively as the mean and standard deviation evaluated over 10 consecutive CT slices. To estimate the discrimination power of ρ/Z_{eff} and x_{PMMA} and x_{Al} decomposition, hence diagnostic potential, a mean Silhouette score using Euclidean distance as a metric was computed on mean values of all tissue types collected from the mastectomy samples [122]. The mean Silhouette score (MSS) is a tool to quantify how similar are samples within the same cluster and how separated they are from other clusters, defined as:

$$\mathrm{MSS} = \frac{1}{n}\sum_{k=0}^{n}\frac{\mathrm{NC}_k - \mathrm{IC}_k}{max(\mathrm{NC}_k,\, \mathrm{IC}_k)} \tag{80}$$

where IC is the mean intra-cluster distance and NC is the mean nearest-cluster distance for each sample k, and n equals the number of selected tissue types × number of selected mastectomy samples. Negative values of MSS indicate cluster overlap, values around 0 signal that samples are on or close to the boundary between clusters, and positive values up to 1 indicate increased cluster separation.

Finally, extracted density and effective atomic numbers from the calibration phantom and Sample 4 were fed to the mathematical relationship given in equation 47 to extrapolate linear attenuation coefficients of tissues for arbitrary (virtual) monochromatic energy levels. The uncertainty was propagated from the standard deviation of obtained ρ and $\mathrm{Z_{eff}}$ values.

6.4 Results

6.4.1 Calibration phantom results

The accuracy of material decomposition in phantom materials following the Gaussian fitting in the histogram space is shown in Fig. 37a. Quantities x_1 and x_2 in equations 70 and 71 are replaced with x_{PMMA} and x_{Al} because of the particular basis choice. Fig. 37b corresponds to the decoupling of density and effective atomic number in equations 72 and 73. The fitting parameters A, S_u, S_v defined in equation 76, and angle θ for phantom materials are given and further discussed in C.

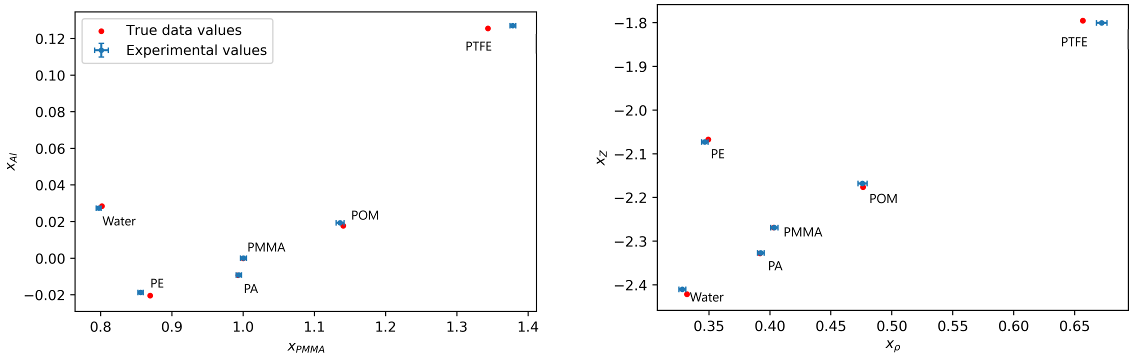

(a) (b)

Figure 37: Experimentally obtained basis material concentrations (blue) against the true data values (red) in (a) the PMMA-Al basis and (b) decoupled reference frame. The error bars show standard error a) computed using equations 82 and 83 and b) propagated using equations 87 and 88 in section B.

The decoupled values from Fig. 37b were calibrated to absolute density and effective atomic numbers (table 4) applying the least-squares fitting method to the functional forms given in equations 74 and

75. Both calibration curves were based on the phantom material inserts in the range of interest for soft tissue imaging and the mapping to correct density and the effective atomic number was obtained at $R^2 = 0.998$ and $R^2 = 0.997$, respectively. Calibration curves are given in Fig. 38 and corresponding density and Z_{eff} values are given in table 5. Using the equation 79, % errors in calibration materials were estimated to be below 3% and 1.5%, respectively, after the density and effective atomic number calibration.

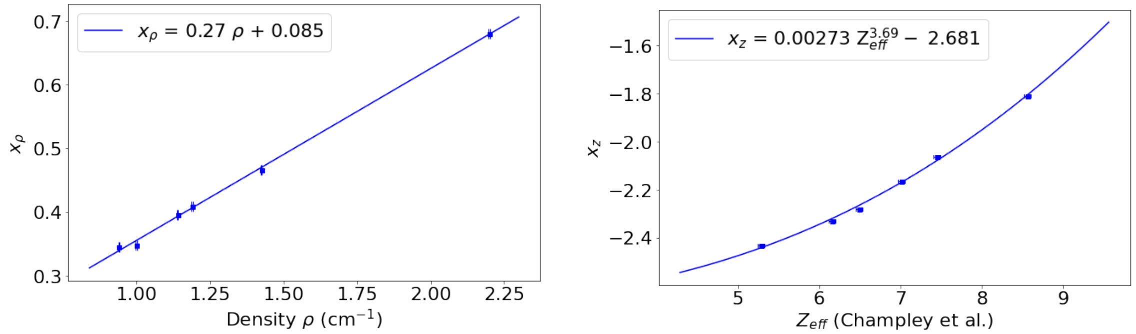

(a)

(b)

Figure 38: Theoretical data points fitted to (a) a linear calibration curve for density ρ, and (b) a power-law curve for Z_{eff} of the same form suggested by the equations 74 and 75.

Table 5: Z_{eff} and ρ with the corresponding standard errors σ_Z and σ_ρ obtained from the calibration phantom and $\%err$ computed using equation 79.

Material	$\rho \pm \sigma_\rho$ (g/cm^3)	$Z_{\mathrm{eff}} \pm \sigma_{Z_{\mathrm{eff}}}$	$\%err\ \rho$	$\%err\ Z_{\mathrm{eff}}$
PE	0.963 ± 0.004	5.36 ± 0.02	2.4	1.3
Water	0.971 ± 0.001	7.51 ± 0.02	2.9	0.9
PA	1.149 ± 0.004	6.10 ± 0.01	0.7	1.0
PMMA	1.198 ± 0.004	6.40 ± 0.01	0.7	1.4
POM	1.411 ± 0.004	7.04 ± 0.01	1.0	0.4
PTFE	2.204 ± 0.003	8.55 ± 0.01	0.2	0.2

6.4.2 Breast mastectomy results

Tissues inside the mastectomies delineated by a radiologist were quantitatively analyzed in terms of their density and effective atomic number and presented in Fig. 39, with average values given in table 6. For comparison, decomposition to basis material coefficients x_{PMMA} and x_{Al} are also given in Fig. 39. Skin tissue was not included in the graph as it is anatomically well separated from other tissues of the breast.

The level of separation between adipose, fibro-glandular, and tumor tissue in ρ and Z_{eff} space was found to be 0.31 (on a scale of -1 to 1) using MSS. Pairwise comparison of adipose and fibro-glandular (MSS = 0.59), adipose and tumor (MSS = 0.74), and fibro-glandular and tumor (MSS = 0.17) showed

Table 6: Average Z_{eff} and ρ from 5 mastectomy samples.

Tissue type	$\rho \pm SD_\rho$ (g/cm^3)	$Z_{\text{eff}} \pm SD_{Z_{\text{eff}}}$
Adipose	0.90 ± 0.02	5.94 ± 0.09
Fibro-glandular	0.96 ± 0.02	7.03 ± 0.12
Tumor	1.07 ± 0.03	7.40 ± 0.10
Skin	1.08 ± 0.02	7.31 ± 0.06

that adipose tissue can be distinguished from the other two, while fibro-glandular and tumor are closer together in ρ/Z_{eff} space. In comparison, MSS in x_{PMMA} and x_{Al} space was -0.02. From Fig. 39 it can be seen that adipose tissue can be distinguished from fibro-glandular and tumorous purely based on effective atomic number values. On the other hand, fibro-glandular and tumorous tissues are overlapping both in their effective atomic numbers and densities and can be distinguished only if both quantitative values are observed together.

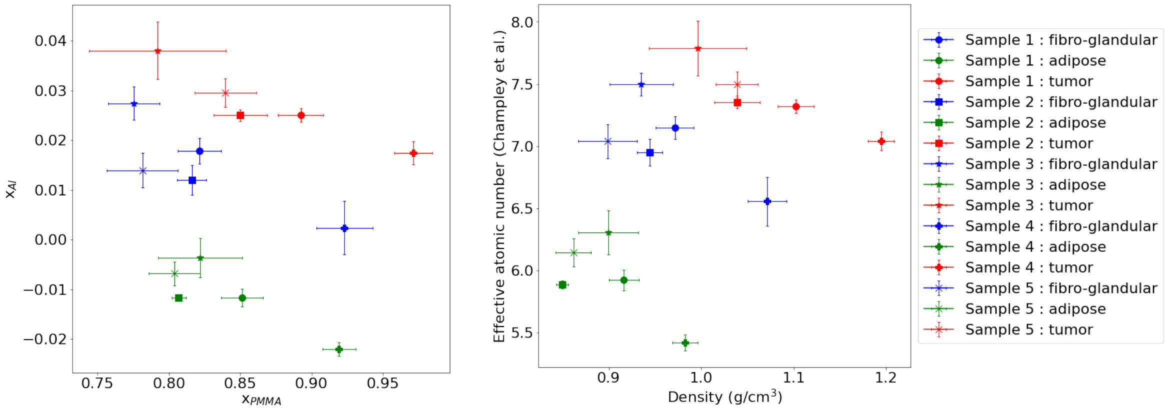

(a)

(b)

Figure 39: Quantitative description of tissues in (a) x_{PMMA} and x_{Al} basis and (b) in terms of density (g/cm^3) and atomic number computed as in Champley *et al* [30]. Adipose, fibro-glandular, and tumorous tissues are distinguished with green, blue, and red colors, respectively, while marker shapes correspond to different mastectomy samples. Error bars represent the standard deviation of 10 ROIs.

In addition to adipose, fibro-glandular, and malignant tissue, the mastectomy labeled as Sample 4 contains well-separated pure glandular tissue and skin. Thus, an extensive investigation was conducted on this tissue. Extracted density and effective atomic number were 0.98 ± 0.01 and 5.42 ± 0.06 for adipose, 1.07 ± 0.02 and 6.56 ± 0.20 for fibro-glandular, 1.18 ± 0.02 and 6.88 ± 0.09 for glandular, 1.19 ± 0.01 and 7.04 ± 0.07 for tumorous, and 1.19 ± 0.02 and 6.87 ± 0.04 for skin tissue, respectively. In this particular mastectomy sample, mean density and Z_{eff} are not distinguishable between the skin and glandular tissue. Glandular tissue has higher Z_{eff} and density than fibro-glandular tissue, but almost the same density and slightly lower Z_{eff} than tumorous tissue.

Virtual μ values of phantom materials and tissues in sample 4 are given in Fig. 40. The obtained

ρ and Z_{eff} values correctly map to experimentally measured μ values and provide information about tissue separation at lower energies with respect to those used for tissue scanning.

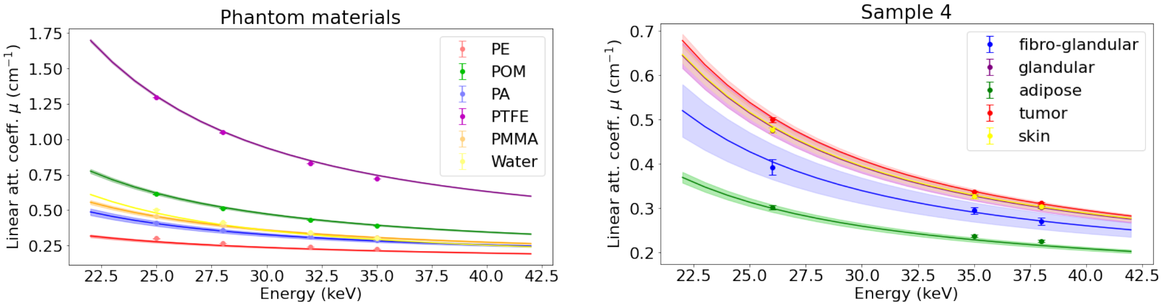

Figure 40: Virtual linear attenuation coefficients computed from extracted density and effective atomic numbers. Full lines represent virtual μ values extracted from experimental data at an arbitrary energy level, while uncertainty was propagated from the standard deviation of ρ and Z_{eff}.

6.5 Discussion of breast mastectomy results

Conventional CT scans offer a relatively low specificity when distinguishing between soft tissues of slightly different compositions. On the other hand, spectral imaging advances the ability to distinguish such tissues by probing their attenuation properties at several energy levels. Spectral information is used for the decomposition of data in basis materials, such as PMMA-Al. The decomposed material maps can be used as an intermediate step to estimating the uniquely defined physical quantities of imaged tissues. Utilizing these quantities, virtual monochromatic μ values at arbitrary energy levels can be further extrapolated. In this work, a new approach to material decomposition and ρ/Z_{eff} estimation was presented to characterize breast tissues.

A least-square fitting approach to two-basis material decomposition was adopted for an over-determined system when μ values can be measured at several energy levels. This was the case in our retrospective study with monochromatic beams, but the same approach can be applied to multi-threshold photon-counting detectors. Although both setups provide multiple spectral imaging channels, the performance of multi-threshold photon-counting detectors is limited compared to multiple monochromatic images as *i)* energy bins cover a range of energies much wider than the energy resolution of synchrotron monochromatic beams, and as already briefly explained, *ii)* energy resolution of PCDs is further degraded by charge sharing and pulse pileup effects. Thus, the latter limits the reduction of bin energy width and the increase of the number of energy bins. To attain similar performance, novel approaches to charge sharing and pulse pileup correction such as the one introduced in 4.1.4 are needed. The procedure for decoupling density from Z_{eff} depends on the quality of performed material decomposition, but is at the same time independent of the method itself, and can be applied to other methods published in the literature. Experimentally computed concentrations x_{PMMA} and x_{Al} of basis materials and related basis x_ρ and x_{Z} in the phantom were found to be in good agreement with the ground truth values. Moreover, small associated standard errors in Fig. 37 show that plastic inserts can be separated in both material and x_ρ/x_{Z} basis. The theoretically derived functions in equations 74 and 75 were fitted to 6 data points corresponding to tissue-equivalent plastics in the phantom. The high accuracy ($\text{R}^2 > 0.99$) of the fitting procedure justifies the assumptions made in theoretical derivation. The systematic errors observed in Fig. 37 for some materials (*e.g.,* PTFE and PE), that can probably be ascribed to slight differences between the composition of the phantom materials and the ones published in [33], do not impact the process of calibration, leading to an agreement with the ground truth data at an average % error of 1.34 % for ρ and 0.89 % for Z_{eff}, as shown in table 5. These results demonstrate that soft-tissue-equivalent plastic materials of similar composition can be distinguished from spectral CT data using estimated effective atomic number and density values.

The preliminary study on the breast cancer mastectomy samples was an attempt to demonstrate the feasibility of our method to distinguish between fibro-glandular and tumorous tissues inside the breast. Based on the available samples, it was shown that starting from spectral data it is possible to separate adipose, fibro-glandular and tumorous tissues based on their physical characteristics. This might be useful in risk assessment, cancer diagnosis, and the assessment of the status of the disease. Although pure glandular and tumorous tissue in Sample 4 had almost the same density and slightly different effective atomic numbers, this could be due to the desmoplastic core present inside the tumor and no conclusions could be made based on a single piece of evidence. The importance of Z_{eff} to X-ray attenuation can be observed when comparing adipose and fibro-glandular tissue clusters. It can be seen that lower μ values for adipose tissue are driven by lower Z_{eff}, rather than significantly lower density. Distinguishing tumorous and pure glandular tissue is challenging because only slight differences exist in both density and Z_{eff}. In our study, we observed that it is not possible to distinguish between different tissues solely on density or effective atomic number or μ value alone while reasonable discrimination (MSS = 0.31) can be obtained considering 2D clusters in ρ/Z_{eff} space. A worse separation (MSS = -0.02) can be obtained using just material coefficients x_{PMMA} and x_{Al}. Therefore, using density and effective atomic number maps in the diagnostic workflow could be beneficial, potentially allowing the identification of the tissue type based on quantitative measurements. Because of improved tissue separation, interpretability, as well as the ability to measure these quantities with other experimental techniques, density and Z_{eff} should be preferred over a simple material decomposition approach.

Virtual monochromatic images are usually computed directly from decomposed basis (*e.g.,* μ_1 and μ_2) using x_1 and x_2 in equation 23. Equivalently, physically relevant ρ/Z_{eff} space can be used to compute other quantitative maps established in clinical practice. Linear attenuation values in

Fig. 40 were calculated using equation 47 at energies within and outside the energy range used in the experiment. Virtual μ values calculated using the Z_{eff} defined by Champley *et al* [30] were in agreement (within the measurement error) with experimentally measured μ coefficients in both the phantom and Sample 4 and they enabled comparison with experimentally obtained μ values in other studies. For Sample 4, which contained tissues examined by Fredenberg *et al* [99], μ values were compared at energies of 20, 30, and 40 keV with average % error of 3.3, 7.3, and 3.4 %, for glandular, adipose and tumor tissue, respectively.

Our approach to tissue analysis could be directly applied to state-of-the-art synchrotron radiation breast CT setups currently developed in Trieste at Elettra Sincrotrone SYRMEP beamline [105], and at ANSTO Imaging and Medical beamline in Australia [123]. With these experimental settings, it should be mentioned that multiple energy acquisitions would be required, thus resulting in an increased dose to the breast. On the other hand, due to the high contrast-to-noise ratio of phase-contrast images, the dose per scan could be reduced thus bringing overall acceptable radiation exposures. Considering clinical systems in hospitals, the advent of spectral CT paves the way to material decomposition following a single shot acquisition without a significant increment of the dose. Photon-counting breast CT systems are in clinical practice [101] and an extension to spectral applications is expected.

Studies estimating both ρ and Z_{eff} of human tissues using synchrotron CT systems are almost nonexistent. The study by Torikoshi *et al* [34] introduced a method to compute these quantities avoiding the material decomposition task. An average accuracy of 0.9 % for ρ_e and 1 % for Z_{eff} is comparable to our method, but the dose level used was not reported. The analysis was performed on low-Z_{eff} plastic materials using a pair of monochromatic acquisitions. Considerably more papers using conventional systems have been published, but not focusing on breast tissues or breast dedicated scanners. Szczykutowicz *et al* [36] performed a methodologically similar approach to the one presented in this paper using a clinical scanner and test object without any noise remedying approach. They successfully decompose electron density and Z_{eff} but at the cost of a significant reduction in signal-to-noise ratio. Lalonde *et al* [124] developed a model in which materials are decomposed in a compressed basis with principal component analysis, using the fact that human tissues are composed of a very limited number of elements. Then, the first principal components are virtual materials containing a certain fraction of those elements. From there Z_{eff} were computed. Azevedo *et al* [29] implemented their System-Independent-Rho-Z (SIRZ) method to obtain physical quantities of phantom materials independent of the shape of the X-ray spectrum. The photoelectric-Compton decomposition is performed in sinogram space and absolute ρ_e and Z values are obtained after the calibration procedure. While physical characterization was successfully described for materials of fairly distinguishable compositions, the noise behavior was also not described in this work. Champley *et al* [30] released a follow-up paper focusing on the optimization and simplification of spectral modeling as a new method called SIRZ-2. Most recently, Busi *et al* [37] developed a physical characterization method using spectral detectors. They claim higher robustness and increased estimation accuracy (25%) compared to SIRZ methods. Extended work from the same group was published in [125] to optimize the computation speed. Machine learning solutions to ρ/Z_{eff} extraction were also tested by Su *et al* [126] using dedicated phantoms with several tissue-equivalent inserts. Good results in computing Z_{eff} were obtained using artificial neural networks and the random forest method with the relative error between 1 and 2 % at clinically relevant doses. However, a low-dose scanning and evaluation of the model on materials that were removed from the training set led to errors up to 6 %. Nonetheless, the authors showed that the machine learning approach is robust and computationally efficient.

Considering specifically the estimation of ρ and Z_{eff} for breast tissues, only a few studies exist and most have been made with experimental setups not used in diagnostic radiology. Berggren *et al* [127] performed clinical evaluation of breast skin Z_{eff} obtained from 709 screening patients using planar spectral mammography. They reported slightly higher values of 7.365 (95% confidence interval: 7.364,7.366) comparable to our findings of 7.31 ± 0.06, with a difference of less than 1% that might be due to the fact that tissues in our experiment were formalin-fixed. Gobo *et al* [128] used a combination of transmission and scattering measurements with ^{241}Am source and an X-ray tube, while Antoniassi *et al* [129] performed scattering measurements at 90 degrees by using low energy beams. Given diverse formulations of Z_{eff} across the literature, we made a comparison in relative change using Z_{eff} of nylon as a reference value in table 7.

Table 7: Literature review of experimentally obtained density and Z_{eff} numbers for fibro-glandular, adipose, and tumorous tissues.

Tissue type	**Density ρ (g/cm^3)**		**Z_{eff} to nylon % diff**		
	This work	Gobo et. al	This work	Gobo *et al*	Antoniassi *et al*
Fibro-glandular	0.96	1.04	15.38	16.73	14.07
Adipose	0.90	0.95	2.68	4.40	5.60
Tumorous	1.07	1.05	21.31	18.87	14.79

This study shows potential for quantitative breast imaging by translating spectral information into the computation of physically relevant quantities, but it also has some limitations. The accuracy of the presented method is mainly governed by the quality of material decomposition, which is highly dependent on the denoising of decomposed data. We gave up the spatial information inside the ROI to obtain quantitatively correct material decomposition during the 2D Gaussian denoising approach. Inaccurate tissue segmentation would result in an erroneous Gaussian fitting procedure as the number of peaks in 2D histogram space corresponds to the number of tissue types being evaluated at once. The appearance of a histogram containing several plastic materials was published in our previous study [19].

Thus, either correct tissue segmentation or an algorithm capable of correctly fitting multiple Gaussian functions in case no segmentation is performed are critical aspects of the present model. For the proof of concept, we relied on high-quality synchrotron beam radiation, but to make this approach broadly used, we plan to apply the method to more accessible polychromatic sources. Finally, the conclusions drawn in this study were based on the analysis of 5 mastectomy samples fixed in formalin which could slightly bias the measured μ values (less than 0.5 % [99]). More samples will be evaluated to further confirm these findings. Despite the mentioned limitations, given the general validity of the proposed decomposition model and the foreseeable use of spectral detectors in breast CT scanners, the present feasibility study paves the way for its application to clinical spectral breast CT data.

In conclusion, a model incorporating CT reconstructions of an arbitrary number of spectral energy channels was developed to compute material density and effective atomic number. The density and effective atomic number of soft-tissue-equivalent plastic materials were computed with an average accuracy in the order of 1 %, and the same approach was applied to the set of 5 mastectomy samples. The quantitative analysis presented here suggests that adipose, fibro-glandular, and tumorous tissues can be distinguished, given the mean Silhouette scores obtained for each tissue pair. Density and effective atomic number can also be used for physics-based extrapolation of virtual monochromatic linear attenuation coefficients outside of the experimental energy range. Breast CT is an emerging technology that is capable of providing three-dimensional imaging of the breast and its extension to spectral imaging is certainly desirable for exploring the potential of material characterization in clinical trials.

7 Optimization of spectral imaging for clinical synchrotron CT

In the previous chapter 3.3, it has been demonstrated that synchrotron radiation offers unique advantages over conventional setups in terms of high brilliance and coherent X-ray beam, enabling precise manipulation of the beam for improved image acquisition. One of the primary benefits of high brilliance for X-ray imaging is the capability to filter, shape, and monochromatize the beam to meet specific imaging requirements. As we introduced in section 3.3.1, the coherent nature of the beam can be exploited by placing the detector at an appropriate distance, allowing for the propagation of X-ray phase differences caused by the interaction with a sample. Utilizing phase retrieval techniques such as Paganin filtering [51], pure attenuation maps with an improved contrast-to-noise ratio can be obtained. This has proven particularly advantageous in imaging soft tissues, where the differentiation between similar tissues is crucial for accurate diagnosis. This realization spurred the development of clinical synchrotron X-ray imaging facilities, such as breast CT synchrotron setups in Trieste, Italy, and Melbourne, Australia [105].

Monochromatic beams for X-ray imaging are preferred over polychromatic beams due to the enhanced contrast-to-noise ratio between different tissues especially at low energy levels, the elimination of beam-hardening artifacts, and the utilization of phase-contrast to improve image quality. In the realm of synchrotron CT, thanks to the high brilliance of synchrotron sources, medical imaging beamlines can afford the filtration of polychromatic ("white") beams to obtain specific X-ray wavelengths using crystal monochromators. This approach eliminates the need for material decomposition to obtain monochromatic images but doesn't provide spectral measurements needed for more quantitative evaluation of scanned materials. The strait-forward approach leading to the best spectral separation and the most accurate quantitative analysis would be acquiring one more (or several) monochromatic images at other energy levels. However, there are two major objections to this approach: i) the acquisition of a larger number of images at different energy levels introduces an additional dose to the sample, and ii) changing the energy in synchrotron setups typically involves rotating and adjusting the monochromator, which is time-consuming and takes several minutes.

In this work, spectral data acquisition with synchrotron beams was further optimized to characterize breast CT images in terms of material density ρ and the effective atomic number. We addressed the challenges of multiple data acquisition with monochromatic beams through a study aimed at examining the effect of acquiring multiple monochromatic images versus just a pair of monochromatic images on the accuracy of material decomposition. In this approach number of spectral channels was governed by the number of image acquisitions with the PCD detector which did not operate in spectral mode. Instead, the detector operated in a single-threshold continuous reading "dead-time free" mode (*i.e.* counting in one counter while reading the other one).

7.1 Optimization methods

CT images were once again acquired at the SYRMEP beamline of Elettra, an Italian synchrotron light source in Trieste. The detector was the same large area Pixirad8 photon-counting detector of very fine pitch (62 microns) and experimental conditions matched the ones introduced in section 6.1.2, in terms of acquisition geometry and processing of the data. Acquired projections were pre-processed with an ad-hoc procedure [116] and then phase-retrieved using an algorithm based on the homogeneous transport of intensity equation (TIE-Hom) [51]. Finally, CT reconstructions were obtained via a GPU-based filtered-back-projection algorithm with Shepp-Logan filtering [117].

Material decomposition, used as an intermediate step to ρ/Z_{eff} decomposition, was performed using the singular value material decomposition approach described in section 2.1.2. As a reminder, with the SVD method, the number of left-singular vectors (also referred to as principal components) corresponding to the number of input spectral channels are extracted. The principal components are the linear combinations of the spectral datasets that capture the maximum variance in the data, and they are ordered in such a way that the first principal component explains the most variance, the second explains the second most, and so on. In section 2.1.2 we showed that the first two components can always be related to an arbitrary set of basis materials. In this particular study, we once again selected aluminum and PMMA and obtained full 3D volumes of PMMA and Al basis maps that contained sufficiently low noise, which was further suppressed with an adopted bilateral filter. Our procedure for extracting ρ and Z_{eff} is independent of the material decomposition approach as long as it produces quantitatively correct results. Thus, we applied the same approach laid out in the section 6.2 to obtain density and Z_{eff} maps from said decomposition. The study was performed on the same custom-made cylindrical phantoms that contained the five inserts of polyethylene (PE), nylon (PA), PMMA, polyoxymethylene (POM), and polytetrafluoroethylene (PTFE) mimicking soft tissues of similar attenuation properties. For this acquisition, the single threshold of the detector operating in "dead-time free" mode was set to 3 keV as a single noise cancellation threshold. Spectral information was obtained with monochromatic beams of energies: 25, 28, 30, 32, 35, 38, and 40 keV, and as the phantom is a rigid object, data didn't require any co-registration. The metric of interest was CNR computed on the ROI inside PTFE ("Teflon") and PA ("nylon") inserts with respect to the surrounding water, defined as:

$$\mathrm{CNR} = \frac{|\mathrm{PTFE}_{\mathrm{avg}} - \mathrm{PA}_{\mathrm{avg}}|}{\mathrm{H_2O}_{\mathrm{std}}}, \tag{81}$$

where $\mathrm{PTFE}_{\mathrm{avg}}$ and $\mathrm{PA}_{\mathrm{avg}}$ represent the mean intensity of the signal and background, respectively, while $\mathrm{H_2O}_{\mathrm{std}}$ represents the standard deviation of the noise in water.

7.2 Optimization results

The acquisition of a larger number of images at different energy levels introduces an additional dose to the sample. The first two principal components and following PMMA and Al material maps were obtained from the five datasets containing 2, 3, 4, 5, and 7 spectral CT reconstructions. The CNR was measured on both, extracted principal components and decomposed basis set, and results are shown in Fig. 41.

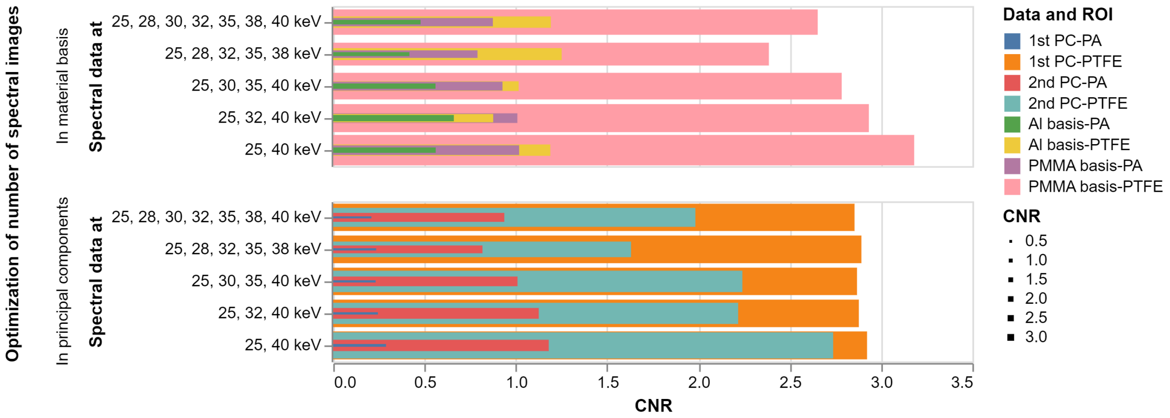

Figure 41: Contrast-to-noise ratio was computed in space of principal components and also basis material space. Contrast was estimated as a difference in mean values measured in PTFE and PA inserts against water.

Fig. 41 suggests that SVD decomposition can be performed on just two independent scans at beam energies of 25 and 40 keV without affecting the CNR. Therefore, this set of spectral images was chosen for the SVD approach. In Fig. 42, principal components of singular value decomposition are given in the first column and basis material image pair in the second column. Physical quantities - effective atomic number and material density - are extracted from said decomposition, after applying an adopted bilateral filtering procedure [130] to PMMA and Al images. Density and effective atomic number maps obtained this way are shown in the last column of the same figure.

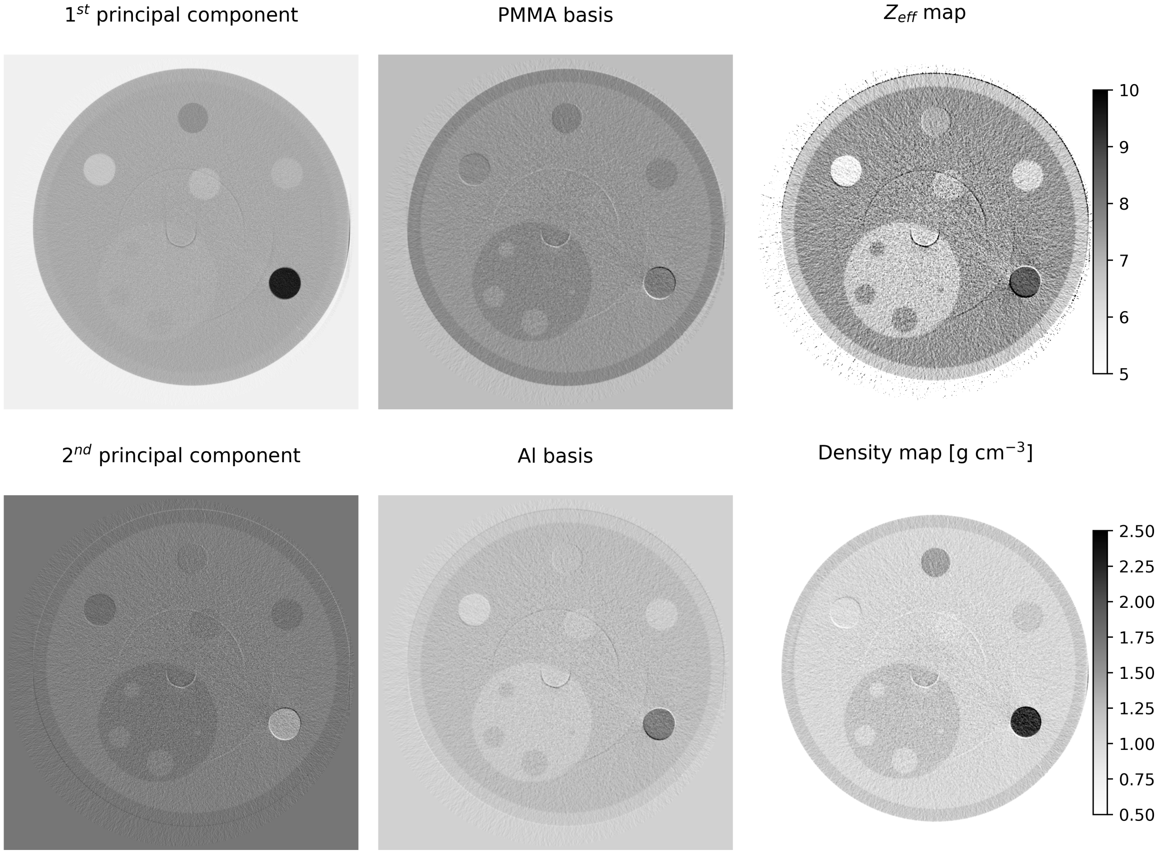

Figure 42: The first column shows the principal components extracted from spectral data. The corresponding material basis images obtained by the procedure described in Sec. 2.1.2 are given in the second column. Basis images were post-processed by an adopted bilateral filter. The last column shows extracted Z_{eff} and density maps. Scans are represented in the inverted grayscale, where higher density and Z_{eff} are represented with darker shades of gray.

Conclusion

In conclusion, this doctoral thesis has underscored the significance of spectral imaging as a promising avenue to address the enduring challenge of soft tissue characterization in X-ray imaging. The primary focus has been on the quantification of tissue properties, particularly iodine content, virtual monochromatic imaging, density, and effective atomic number. It is worth noting that the computation of density and effective atomic number presents a valuable and intuitive approach, rooted in the fundamental physics of X-ray interactions, and measurable via diverse methods.

The effectiveness of quantitative imaging relies on the synergy between spectral technology and the accurate recording of spectral data, and the progress in algorithms capable of deriving these key quantities from spectral information. Photon-counting detectors have emerged as a prime candidate, given their ability to reduce imaging noise, provide high resolution, maintain a uniform detector energy response, and inherently obtain spectral information. A critical factor driving the recent adoption of photon-counting detectors in clinical practice is the technological maturity of detector ASICs. Nonetheless, this thesis has revealed that challenges such as charge sharing and pulse pileup can introduce inaccuracies into quantitative maps. The utilization of a virtual imaging platform, which models the detection mechanism and is validated against real-world measurements, has been instrumental in elucidating these limitations. Hardware-based pulse pileup correction solutions such as instant-retrigger technology allow detectors to operate in a specific non-paralyzable mode and extend the linearity range of counting in high flux conditions, which could play a pivotal role in the wider application of photon-counting detectors for quantitative material characterization. Additionally, an investigation into low-dose imaging with the first clinical photon-counting CT system has shown improved iodine quantification when compared to dual-energy scanners. However, it was observed that low-energy virtual monochromatic imaging on the photon-counting CT scanner, employing a 140 keV tube and accommodating large patient volumes, exhibits bias. This appears to be due to the limitation of the potential not being sufficiently high for this specific case. In contrast, dual-energy CT with a potential of 150 keV, using a thin filter, demonstrates more accurate results owing to the availability of higher tube potential. The thesis also explores the most advanced application of spectral imaging utilizing synchrotron radiation, while acknowledging its current lack of clinical feasibility. It illustrates that in the ρ/Z_{eff} space, soft-tissue equivalent materials can be effectively differentiated keeping the spatial information. Singular value material decomposition analysis has shown that two well-separated spectral channels can provide an equivalent amount of information for material decomposition, rendering multiple scans at different energies redundant, with no need for additional exposure. Finally, the analysis of breast tissues demonstrates the capacity of synchrotron-based spectral imaging to discriminate between adipose, fibro-glandular, and tumorous tissues in ρ/Z_{eff} space. This preliminary study suggests a possible solution for tissue differentiation and tumor characterization inside the breast, offering diagnostic benefits.

Spectral imaging, particularly with photon-counting detectors and synchrotron beams, addresses the longstanding challenges of soft tissue differentiation and characterization. Through a comprehensive examination of various aspects of spectral imaging, from fundamental physical principles to practical clinical applications, this research contributes to the ongoing advancement of medical imaging technology, with implications for improved patient diagnosis and care. It highlights both the opportunities and the ongoing challenges in the pursuit of enhancing the capabilities of X-ray imaging for soft tissue characterization.

Appendices

A Low energy VMI in clinical PCCT in large phantoms

The PC-CT scanner is underestimating 40 keV virtual monochromatic levels in the extra-large phantom, particularly in higher-density inserts. This underestimation remains consistent even with increased doses, indicating that low VMIs may not be accurate in extremely obese patients, particularly for dense tissues. The results for the particular case with repeated scans for each dose are given in Fig. 43.

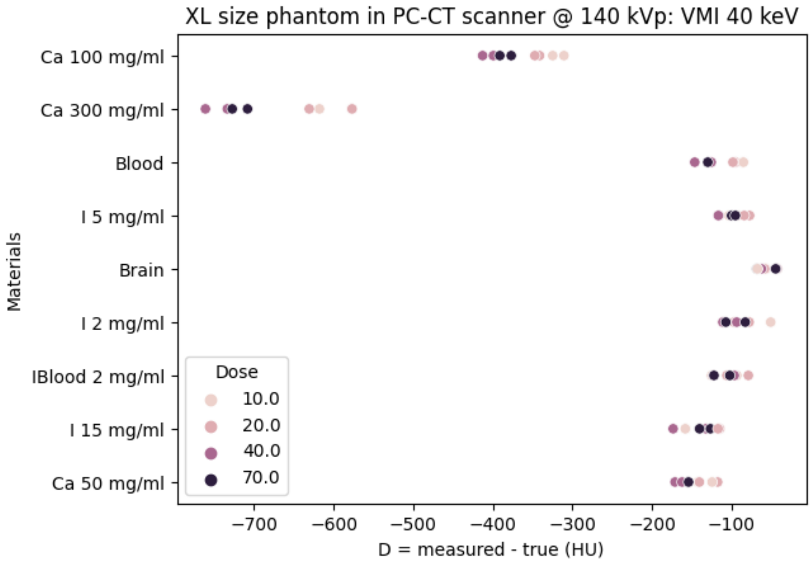

Figure 43: The accuracy of VMI 40 keV HU values in the PC-CT scanner for XL phantom size. Measurements were repeated twice at doses of 10,20,40 and 70 mGy.

B Noise analysis and uncertainties

As it was shown in section 6.2, regions of uniform composition result in scattered values of elongated shape (*i.e.* clusters) in the (x_1, x_2)-plane histogram. Such behavior was ascribed to the unavoidable amount of noise carried by the tomographic reconstructions on which the whole decomposition method is based. Detailed analysis of the propagation of measurement uncertainties, related to the size of the cluster, was carried out. The Gaussian fitting procedure introduced in section 6.2 individuates a preferred direction at angle θ aligned to the major axis u of elliptical Gaussian. The length in this direction and the orthogonal one (minor axis) are identified as the Gaussian spreads in a reference frame (x_u, x_v), which is parallel to the major and minor axes of the spot. The standard errors of the centroid coordinates can be approximated by the ratios between the Gaussian spreads S_u and S_v and the square root of the volume under the Gaussian surface

$$\sigma_{x_u} = \frac{S_u}{\sqrt{V}} \tag{82}$$

$$\sigma_{x_v} = \frac{S_v}{\sqrt{V}} \tag{83}$$

where the volume is given as

$$V = 2\pi\, A\, \frac{S_u\, S_v}{b_1\, b_2} \tag{84}$$

that it is equal to the total number of voxels contributing to the corresponding two-dimensional Gaussian function. Quantities b_1 and b_2 are bin sizes in both directions and A is the peak value. Calculated errors are then translated into uncertainties of coordinates x_ξ and x_ζ in the reference frame rotated by the angle ϕ defined in section (6.1.1). Rotation from the frame identified by angle θ to the frame identified by angle ϕ is defined as

$$\begin{bmatrix} x_\xi \\ x_\zeta \end{bmatrix} = \begin{bmatrix} \cos\alpha & \sin\alpha \\ -\sin\alpha & \cos\alpha \end{bmatrix} \begin{bmatrix} x_u \\ x_v \end{bmatrix}$$

where $\alpha = \phi - \theta$. Propagating uncertainty through the rotation of the reference frame leads to

$$\sigma^2_{x_\xi} = \cos^2\alpha\, \sigma^2_{x_u} + \sin^2\alpha\, \sigma^2_{x_v} \tag{85}$$

$$\sigma^2_{x_\zeta} = \sin^2\alpha\, \sigma^2_{x_u} + \cos^2\alpha\, \sigma^2_{x_v} \tag{86}$$

From the rotated frame, to the rescaled x_ρ, x_Z frame, the division of the second coordinate by the first one implicates

$$\sigma_{x_Z}^2 = \frac{x_\zeta^2}{x_\xi^4}\sigma_{x_\xi}^2 + \frac{1}{x_\xi^2}\sigma_{x_\zeta}^2 \tag{87}$$

while propagating x_ρ remains trivial

$$\sigma_{x_\rho}^2 = \sigma_{x_1}^2 . \tag{88}$$

Finally, shifting to the pair ρ, Z requires equations (74) and (75), leading to the uncertainties

$$\sigma_\rho = \kappa^{-1}\,\sigma_{x_\rho} \tag{89}$$

$$\sigma_Z = \frac{(x_Z - q)^{\frac{1-\lambda}{\lambda}}}{\lambda\, p^{1/\lambda}}\,\sigma_{x_Z} . \tag{90}$$

C Noise behaviour in 2D histogram space

In addition to the estimated centers of the distributions in figure 37a, the 2D Gaussian fit method outputs several other parameters relevant for the accurate estimation of basis material concentrations summarized in table 8. The angle θ at which the cluster is extended remains constant ($\simeq -0.12$) for all materials indicating that blurring is not dependent on the material type. It is rather a result of combined contributions of image acquisition, reconstruction, and material decomposition noise. The amount of blurring in the major direction S_u and the direction orthogonal to it S_v is of the same order of magnitude for all materials. The S_u values are around 2 orders of magnitude larger than S_v values. The amplitude A of the Gaussian function remains constant for the same size of the ROI for all plastic inserts.

Table 8: List of output parameters in 2D Gaussian fitting method for the phantom materials.

Material	**Amplitude (A)**	**Major axis spread S_u**	**Minor axis spread S_v**	**Angle θ**
Water	38	0.40	0.0074	−0.121
PE	40	0.37	0.0065	−0.121
PA	38	0.32	0.0062	−0.120
PMMA	38	0.41	0.0073	−0.121
POM	38	0.32	0.0062	−0.120
PTFE	41	0.46	0.0078	−0.121

These properties are important for the Gaussian fitting procedure because an initial guess for fitting parameters can be given, improving the robustness of the method and increasing the computational speed. A more rigorous statistical description of these features will be the subject of a forthcoming standalone communication.

D Comparison of methods used to compute the atomic number of a compound - Z*comp*ARE

Effective atomic number as a property of a material depends on its chemical composition, but it is not uniquely defined in the literature. Very often different definitions are adopted by researchers depending on the experimental setup, energy range, and type of compounds. Several definitions that have been proposed to compute this quantity can be divided into: *i)* methods that compute Z_{eff} as a weighted average of composing elements in the compound, *ii)* and methods that rely on mass attenuation coefficients of composing elements to compute Z_{eff} [22]. The second group of methods was developed to solve the fundamental problem: Z_{eff} as the quantity defined in the first category is not specifically tied to the absorption property of a material. Thus, weighted sums of elements in a compound used in the first category are exclusively valid for certain energy ranges and often to a certain set of elements contained in the mixture, while methods in the second category rely on tabulated attenuation properties of materials to inherently define Z_{eff} as a quantity tied to attenuation property of the material.

In this section, we compared several available methods for the materials in the calibration phantom. Z*comp*ARE [31] is user-friendly software with a graphical interface that can be used to compare several methods most often used. The comparison of the methods for the calibration phantom materials in the energy range 20 - 40 keV is given in 9.

Table 9: Comparison of the most often used formulations of effective atomic numbers for phantom materials in the energy range 20 - 40 keV.

Material	**Water**	**PE**	**PA**	**PMMA**	**POM**	**PTFE**
Brute formula	H_2O	C_2H_4	$C_{12}H_{22}N_2O_2$	$C_5H_8O_2$	CH_2O	C_2F_4
Spiers *et al*	7.42	5.44	6.12	6.47	6.95	8.43
Glasser *et al*	7.96	5.94	6.60	6.94	7.38	8.62
Hine *et al*	3.34	2.67	3.27	3.60	4.00	7.99
Puumalainen *et al*	3.33	2.67	3.27	3.61	4.00	8.00
Tsai and Cho	7.44	5.47	6.15	6.50	6.98	8.45
Gowda *et al*	7.24	5.05	5.89	6.32	6.85	8.53
Champley *et al*	7.44	5.28	6.16	6.49	7.01	8.56

It can be seen that methods by Spiers *et al*, Tsai and Cho, Glasser *et al*, Gowda *et al*, and Champley *et al* provide very similar Z_{eff} numbers for our experimental conditions. Methods by Hine *et al* and Puumalainen *et al* gave considerably lower Z_{eff} numbers for all materials. Calibration functions of the form defined in equations (74) and (75) were applied to all definitions for Z_{eff} and results are given in figure 44. The mean Silhouette score defining the level of separation in the range -1 to 1 was found to be approx. 0.31 for all methods used. Thus, the distinguishment of tissues could be obtained irrespective of the proposed definition.

The method defined by Champley *et al* [30] showed a slightly better agreement of virtual monochro-

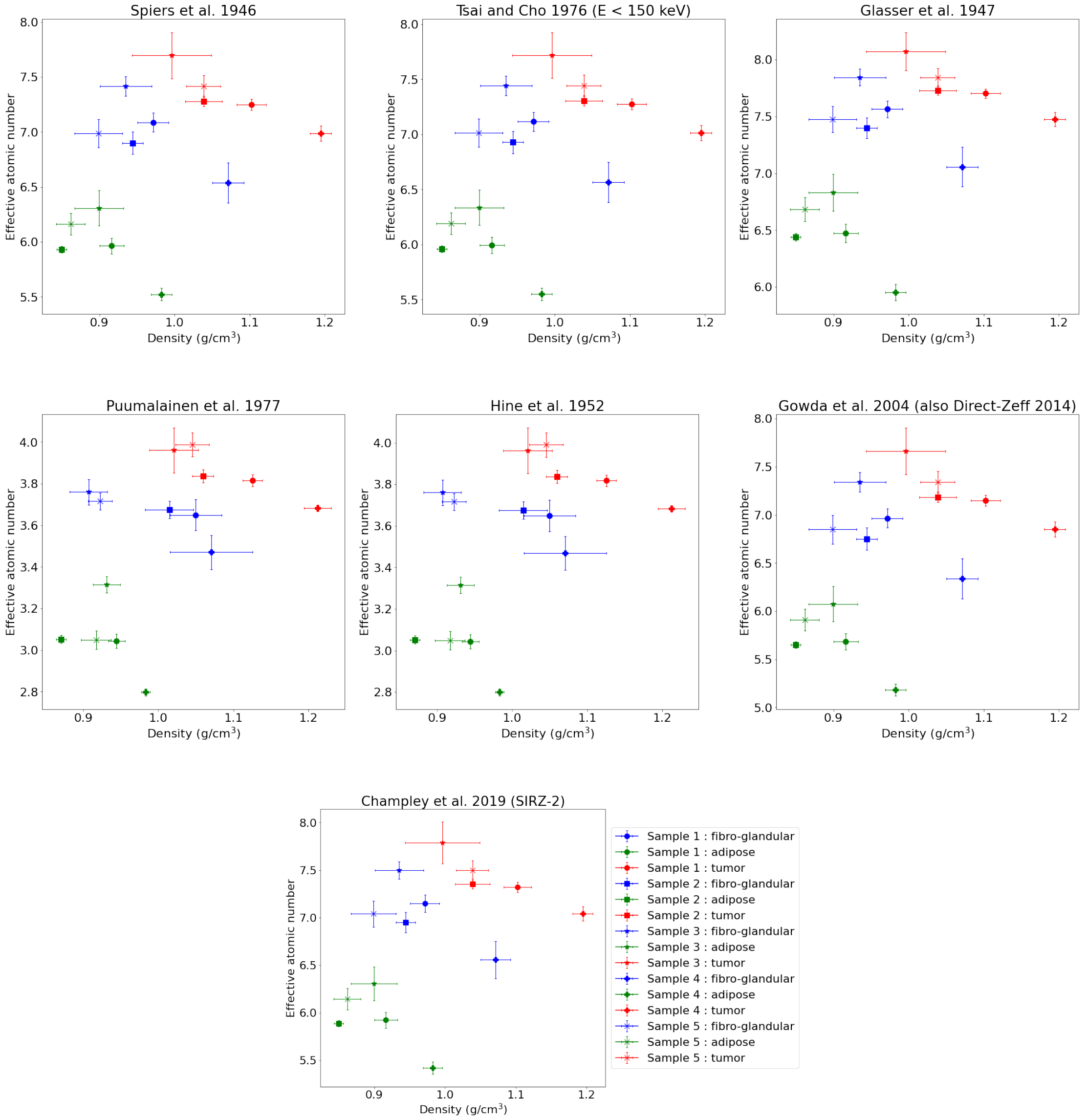

Figure 44: Comparison of Z_{eff} definitions in ρ/Z_{eff} space.

matic μ values computed using equation 47 with experimentally measured data. Constants n, K_1, and K_2 used in equation 47 were estimated to be 4.44, 9.4, and 1.6 using the least-square fit method for elemental materials found in the human body in the Z range of 1-20 across the diagnostic energy range (20 - 200 keV).

References

[1] René-Maxime Gracien, Michelle Maiworm, Nadine Brüche, Manoj Shrestha, Ulrike Nöth, Elke Hattingen, Marlies Wagner, and Ralf Deichmann. How stable is quantitative MRI? – Assessment of intra- and inter-scanner-model reproducibility using identical acquisition sequences and data analysis programs. *NeuroImage*, 207:116364, February 2020.

[2] R de Mello, Y Ma, Y Ji, J Du, and EY Chang. Quantitative MRI MSK Techniques: An Update. *AJR. American journal of roentgenology*, 213(3):524–533, September 2019.

[3] P. Tsialios, M. Thrippleton, A. Glatz, and C. Pernet. Evaluation of MRI sequences for quantitative T1 brain mapping. *Journal of Physics: Conference Series*, 931(1):012038, November 2017. Publisher: IOP Publishing.

[4] Rosa M.S. Sigrist, Joy Liau, Ahmed El Kaffas, Maria Cristina Chammas, and Juergen K. Willmann. Ultrasound Elastography: Review of Techniques and Clinical Applications. *Theranostics*, 7(5):1303–1329, March 2017.

[5] R. E. Alvarez and A. Macovski. Energy-selective reconstructions in X-ray computerised tomography. 21(5):733–744, September 1976. Publisher: IOP Publishing.

[6] A. Contillo and A. Taibi. Material characterisation in phase contrast imaging: The basis decomposition method revisited. *Europhysics Letters*, 117(4):48003, April 2017. Publisher: EDP Sciences, IOP Publishing and Società Italiana di Fisica.

[7] Tim Salditt, Timo Aspelmeier, and Sebastian Aeffner. Biomedical Imaging: Principles of Radiography, Tomography and Medical Physics. In *Biomedical Imaging*. De Gruyter, October 2017.

[8] Jiang Hsieh. *Computed Tomography, Second Edition*. SPIE, 1000 20th Street, Bellingham, WA 98227-0010 USA, October 2009.

[9] Glenn F. Knoll. *Radiation Detection and Measurement*. Wiley, 1979. Google-Books-ID: ih9RAAAAMAAJ.

[10] Teddy Loeliger, Christian Broennimann, and Roger Schnyder. Photon counting imaging method and device with instant retrigger capability, July 2015.

[11] Katsuyuki Taguchi, Eric C. Frey, Xiaolan Wang, Jan S. Iwanczyk, and William C. Barber. An analytical model of the effects of pulse pileup on the energy spectrum recorded by energy resolved photon counting x-ray detectors. *Medical Physics*, 37(8):3957–3969, August 2010.

[12] Teddy Loeliger, Christian Brönnimann, Tilman Donath, Matthias Schneebeli, Roger Schnyder, and Peter Trüb. The new PILATUS3 ASIC with instant retrigger capability. In *2012 IEEE Nuclear Science Symposium and Medical Imaging Conference Record (NSS/MIC)*, pages 610–615, October 2012. ISSN: 1082-3654.

[13] Katsuyuki Taguchi and Jan S. Iwanczyk. Assessment of multi-energy inter-pixel coincidence counters for photon-counting detectors at the presence of charge sharing and pulse pileup: A simulation study. *Medical Physics*, 48(9):4909–4925, September 2021.

[14] A. Sossin, V. Rebuffel, J. Tabary, J. M. Létang, N. Freud, and L. Verger. Influence of scattering on material quantification using multi-energy x-ray imaging. In *2014 IEEE Nuclear Science Symposium and Medical Imaging Conference (NSS/MIC)*, pages 1–5, November 2014.

[15] Bill Triggs, Philip F. McLauchlan, Richard I. Hartley, and Andrew W. Fitzgibbon. Bundle Adjustment — A Modern Synthesis. In Bill Triggs, Andrew Zisserman, and Richard Szeliski, editors, *Vision Algorithms: Theory and Practice*, Lecture Notes in Computer Science, pages 298–372, Berlin, Heidelberg, 2000. Springer.

[16] T. Niu, X. Dong, M. Petrongolo, and L. Zhu. TU-F-18A-02: Iterative Image-Domain Decomposition for Dual-Energy CT. *Medical Physics*, 41(6Part27):475–476, 2014. _eprint: https://aapm.onlinelibrary.wiley.com/doi/pdf/10.1118/1.4889338.

[17] Bingqing Xie, Ting Su, Valérie Kaftandjian, Pei Niu, Feng Yang, Marc Robini, Yuemin Zhu, and Philippe Duvauchelle. Material Decomposition in X-ray Spectral CT Using Multiple Constraints in Image Domain. *Journal of Nondestructive Evaluation*, 38(1):16, January 2019.

[18] Bingqing Xie, Pei Niu, Ting Su, Valérie Kaftandjian, Loic Boussel, Philippe Douek, Feng Yang, Philippe Duvauchelle, and Yuemin Zhu. ROI-Wise Material Decomposition in Spectral Photon-Counting CT. *IEEE Transactions on Nuclear Science*, 67(6):1066–1075, June 2020. Conference Name: IEEE Transactions on Nuclear Science.

[19] S. Vrbaski, R. Longo, A. Taibi, and A. Contillo. Quantitative material characterization based on the spectral decomposition of X-ray tomographic images. *Il nuovo cimento C*, 44(4-5):1–4, 2021. Number: 4-5 Publisher: Societa italiana di fisica.

[20] Stevan Vrbaski, Renata Longo, and Adriano Contillo. From spectral decomposition through SVD to quantitative description of monochromatic CT images: a phantom study. In *Medical Imaging 2022: Physics of Medical Imaging*, volume 12031, February 2022.

[21] Nuclear Data Section International Atomic Energy Agency, Vienna (Austria). XMuDat: Photon attenuation data on PC Version 101 of August 1998 Summary documentation. Technical report, International Atomic Energy Agency (IAEA), 1998. IAEA-NDS–195(rev0) INIS Reference Number: 30022813.

[22] Anne Bonnin, Philippe Duvauchelle, Valérie Kaftandjian, and Pascal Ponard. Concept of effective atomic number and effective mass density in dual-energy X-ray computed tomography. *Nuclear Instruments and Methods in Physics Research Section B: Beam Interactions with Materials and Atoms*, 318:223–231, January 2014.

[23] F. W. Spiers. Effective atomic number and energy absorption in tissues. *The British Journal of Radiology*, 19:52–63, February 1946.

[24] Paul N. Goodwin, Edith H. Quimby, Russell H. Morgan, and Otto Glasser. *Physical foundations of radiology.* Medical Dept., Harper & Row, New York, 4th ed edition, 1970. OCLC: 159036.

[25] G. J. Hine. SECONDARY ELECTRON EMISSION AND EFFECTIVE ATOMIC NUMBERS. *Nucleonics (U.S.) Ceased publication*, Vol: 10, No. 1, January 1952. Institution: Originating Research Org. not identified.

[26] C. M. Tsai and Z. H. Cho. Physics of contrast mechanism and averaging effect of linear attenuation coefficients in a computerized transverse axial tomography (CTAT) transmission scanner. *Physics in Medicine & Biology*, 21(4):544, July 1976.

[27] P. Puumalainen, H. Olkkonen, and P. Sikanen. Assessment of fat content of liver by a photon scattering technique. *The International Journal of Applied Radiation and Isotopes*, 28(9):785–787, September 1977.

[28] Adem Un and Tanfer Caner. The Direct-Zeff software for direct calculation of mass attenuation coefficient, effective atomic number and effective electron number. *Annals of Nuclear Energy*, 65:158–165, March 2014.

[29] Stephen G. Azevedo, Harry E. Martz, Maurice B. Aufderheide, William D. Brown, Kyle M. Champley, Jeffrey S. Kallman, G. Patrick Roberson, Daniel Schneberk, Isaac M. Seetho, and Jerel A. Smith. System-Independent Characterization of Materials Using Dual-Energy Computed Tomography. *IEEE Transactions on Nuclear Science*, 63(1):341–350, February 2016. Number: 1.

[30] Kyle M. Champley, Stephen G. Azevedo, Isaac M. Seetho, Steven M. Glenn, Larry D. McMichael, Jerel A. Smith, Jeffrey S. Kallman, William D. Brown, and Harry E. Martz. Method to Extract

System-Independent Material Properties From Dual-Energy X-Ray CT. *IEEE Transactions on Nuclear Science*, 66(3):674–686, March 2019. Number: 3.

[31] Stevan Vrbaski. ZcompARE, November 2022. original-date: 2022-11-17T15:56:00Z.

[32] A. Brunetti, M. Sanchez del Rio, B. Golosio, A. Simionovici, and A. Somogyi. A library for X-ray–matter interaction cross sections for X-ray fluorescence applications. *Spectrochimica Acta Part B: Atomic Spectroscopy*, 59(10):1725–1731, October 2004.

[33] Tom Schoonjans, Antonio Brunetti, Bruno Golosio, Manuel Sanchez del Rio, Vicente Armando Sole, Claudio Ferrero, and Laszlo Vincze. The xraylib library for X-ray-matter interactions : recent developments. *SPECTROCHIMICA ACTA PART B-ATOMIC SPECTROSCOPY*, 66(11-12):776–784, 2011. Number: 11-12.

[34] Masami Torikoshi, Takanori Tsunoo, Makoto Sasaki, Masahiro Endo, Yutaka Noda, Yumiko Ohno, Toshiyuki Kohno, Kazuyuki Hyodo, Kentaro Uesugi, and Naoto Yagi. Electron density measurement with dual-energy x-ray CT using synchrotron radiation. *Physics in Medicine and Biology*, 48(5):673–685, March 2003.

[35] B. J. Heismann, J. Leppert, and K. Stierstorfer. Density and atomic number measurements with spectral x-ray attenuation method. *Journal of Applied Physics*, 94(3):2073–2079, August 2003. Number: 3.

[36] Timothy P. Szczykutowicz, Zhihua Qi, and Guang-Hong Chen. A simple image based method for obtaining electron density and atomic number in dual energy CT. page 79613A, Lake Buena Vista, Florida, March 2011.

[37] Matteo Busi, Jan Kehres, Mohamad Khalil, and Ulrik Lund Olsen. Effective atomic number and electron density determination using spectral x-ray CT. In *Anomaly Detection and Imaging with X-Rays (ADIX) IV*, volume 10999, pages 7–17. SPIE, May 2019.

[38] T. Pascart, L. Norberciak, J. Legrand, F. Becce, and J. F. Budzik. Dual-energy computed tomography in calcium pyrophosphate deposition: initial clinical experience. *Osteoarthritis and Cartilage*, 27(9):1309–1314, September 2019.

[39] Nace Hudobivnik, Florian Schwarz, Thorsten Johnson, Linda Agolli, George Dedes, Thomas Tessonnier, Frank Verhaegen, Christian Thieke, Claus Belka, Wieland H. Sommer, Katia Parodi, and Guillaume Landry. Comparison of proton therapy treatment planning for head tumors with a pencil beam algorithm on dual and single energy CT images. *Medical Physics*, 43(1):495–504, 2016. _eprint: https://onlinelibrary.wiley.com/doi/pdf/10.1118/1.4939106.

[40] Sung Hyun Lee, Naoki Sunaguchi, Akie Nagao, Yoshiyuki Hirano, Hiroshi Sakurai, Yosuke Kano, Masami Torikoshi, Tatsuaki Kanai, and Mutsumi Tashiro. Calculation of Stopping-Power Ratio from Multiple CT Numbers Using Photon-Counting CT System: Two- and Three-Parameter-Fitting Method. *Sensors*, 21(4):1215, January 2021. Number: 4 Publisher: Multidisciplinary Digital Publishing Institute.

[41] Ming Yang, Patrick Wohlfahrt, Chenyang Shen, and Hugo Bouchard. Dual- and multi-energy CT for particle stopping-power estimation: current state, challenges and potential. *Physics in Medicine & Biology*, 68(4):04TR01, February 2023. Publisher: IOP Publishing.

[42] Leening P. Liu, Matthew Hwang, Matthew Hung, Michael C. Soulen, Thomas P. Schaer, Nadav Shapira, and Peter B. Noël. Non-invasive mass and temperature quantifications with spectral CT. *Scientific Reports*, 13(1):6109, April 2023. Number: 1 Publisher: Nature Publishing Group.

[43] G. N. Hounsfield. Computerized transverse axial scanning (tomography). 1. Description of system. *The British Journal of Radiology*, 46(552):1016–1022, December 1973.

[44] Aaron So and Savvas Nicolaou. Spectral Computed Tomography: Fundamental Principles and Recent Developments. *Korean Journal of Radiology*, 22(1):86–96, January 2021.

[45] Martin J. Willemink, Mats Persson, Amir Pourmorteza, Norbert J. Pelc, and Dominik Fleischmann. Photon-counting CT: Technical Principles and Clinical Prospects. *Radiology*, 289(2):293–312, November 2018.

[46] Salim Si-Mohamed, Sara Boccalini, Marjorie Villien, Yoad Yagil, Klaus Erhard, Loic Boussel, and Philippe Douek. First Experience With a Whole-Body Spectral Photon-Counting CT Clinical Prototype. *Investigative Radiology*, Publish Ahead of Print, February 2023.

[47] U. Bonse and M. Hart. AN X-RAY INTERFEROMETER. *Applied Physics Letters*, 6(8):155–156, November 2004.

[48] T. J. Davis, D. Gao, T. E. Gureyev, A. W. Stevenson, and S. W. Wilkins. Phase-contrast imaging of weakly absorbing materials using hard X-rays. *Nature*, 373(6515):595–598, February 1995. Number: 6515 Publisher: Nature Publishing Group.

[49] Franz Pfeiffer, Timm Weitkamp, Oliver Bunk, and Christian David. Phase retrieval and differential phase-contrast imaging with low-brilliance X-ray sources. *Nature Physics*, 2(4):258–261, April 2006. Number: 4 Publisher: Nature Publishing Group.

[50] Timur E. Gureyev, Yakov I. Nesterets, Alexander Kozlov, David M. Paganin, and Harry M. Quiney. On the "unreasonable" effectiveness of transport of intensity imaging and optical deconvolution. *JOSA A*, 34(12):2251–2260, December 2017. Publisher: Optica Publishing Group.

[51] D. Paganin, S. C. Mayo, T. E. Gureyev, P. R. Miller, and S. W. Wilkins. Simultaneous phase and amplitude extraction from a single defocused image of a homogeneous object. *Journal of Microscopy*, 206(1):33–40, 2002. _eprint: https://onlinelibrary.wiley.com/doi/pdf/10.1046/j.1365-2818.2002.01010.x.

[52] T. E. Gureyev, S. C. Mayo, D. E. Myers, Ya. Nesterets, D. M. Paganin, A. Pogany, A. W. Stevenson, and S. W. Wilkins. Refracting Röntgen's rays: Propagation-based x-ray phase contrast for biomedical imaging. *Journal of Applied Physics*, 105(10):102005, May 2009.

[53] Luca Brombal, Sandro Donato, Diego Dreossi, Fulvia Arfelli, Deborah Bonazza, Adriano Contillo, Pasquale Delogu, Vittorio Di Trapani, Bruno Golosio, Giovanni Mettivier, Piernicola Oliva, Luigi Rigon, Angelo Taibi, and Renata Longo. Phase-contrast breast CT: the effect of propagation distance. 63(24):24NT03, December 2018. Publisher: IOP Publishing.

[54] Ehsan Abadi, William P. Segars, Benjamin M. W. Tsui, Paul E. Kinahan, Nick Bottenus, Alejandro F. Frangi, Andrew Maidment, Joseph Lo, and Ehsan Samei. Virtual clinical trials in medical imaging: a review. *Journal of Medical Imaging*, 7(4):042805, July 2020.

[55] Ehsan Abadi, Brian Harrawood, Shobhit Sharma, Anuj Kapadia, William P. Segars, and Ehsan Samei. DukeSim: A realistic, rapid, and scanner-specific simulation framework in computed tomography. *IEEE transactions on medical imaging*, 38(6):1457–1465, June 2019.

[56] Xu Ji, Ran Zhang, Yongshuai Ge, Guang-Hong Chen, and Ke Li. Signal and noise characteristics of a CdTe-based photon counting detector: Cascaded systems analysis and experimental studies. *Proceedings of SPIE–the International Society for Optical Engineering*, 10132:1013207, February 2017.

[57] Vicki T. Taasti, David C. Hansen, Gregory J. Michalak, Amanda J. Deisher, Jon J. Kruse, Ludvig P. Muren, Jørgen B. B. Petersen, and Cynthia H. McCollough. Theoretical and experimental analysis of photon counting detector CT for proton stopping power prediction. *Medical physics*, 45(11):5186–5196, November 2018.

[58] Katsuyuki Taguchi, Christoph Polster, W. Paul Segars, Nafi Aygun, and Karl Stierstorfer. Model-based pulse pileup and charge sharing compensation for photon counting detectors: A simulation study. *Medical Physics*, 49(8):5038–5051, 2022. _eprint: https://onlinelibrary.wiley.com/doi/pdf/10.1002/mp.15779.

[59] Kyle Champley. Livermore Tomography Tools (LTT) Software Package.

[60] P. Zambon and C. Amato. Pulse pileup model for spectral resolved X-ray photon-counting detectors with dead time and retrigger capability. *Frontiers in Physics*, 11, 2023.

[61] V. Di Trapani, A. Bravin, F. Brun, D. Dreossi, R. Longo, A. Mittone, L. Rigon, and P. Delogu. Characterization of the acquisition modes implemented in Pixirad-1/Pixie-III X-ray Detector: Effects of charge sharing correction on spectral resolution and image quality. *Nuclear Instruments and Methods in Physics Research Section A: Accelerators, Spectrometers, Detectors and Associated Equipment*, 955:163220, March 2020.

[62] W. P. Segars, G. Sturgeon, S. Mendonca, Jason Grimes, and B. M. W. Tsui. 4D XCAT phantom for multimodality imaging research. *Medical Physics*, 37(9):4902–4915, September 2010.

[63] Wim van Aarle, Willem Jan Palenstijn, Jeroen Cant, Eline Janssens, Folkert Bleichrodt, Andrei Dabravolski, Jan De Beenhouwer, K. Joost Batenburg, and Jan Sijbers. Fast and flexible X-ray tomography using the ASTRA toolbox. *Optics Express*, 24(22):25129–25147, October 2016. Publisher: Optica Publishing Group.

[64] Daniel Vavrik, Tomas Holy, Jan Jakubek, Stanislav Pospisil, Zdenek Vykydal, and Jiri Dammer. *Direct Thickness Calibration:. way to Radiographic Study of Soft Tissues*. April 2006. Conference Name: Astroparticle, Particle and Space Physics, Detectors and Medical Physics Applications Pages: 773-778 ADS Bibcode: 2006apsp.conf..773V.

[65] Jan Jakubek. Data processing and image reconstruction methods for pixel detectors. *Nuclear Instruments and Methods in Physics Research Section A: Accelerators, Spectrometers, Detectors and Associated Equipment*, 576(1):223–234, June 2007.

[66] S. I. Inkinen, M. A. K. Juntunen, A. Kotiaho, and M. T. Nieminen. Calibration method and photon flux influences tiled flat-panel photon counting detector image uniformity in computed tomography. *Journal of Instrumentation*, 15(08):T08005, August 2020.

[67] Moritz H. Albrecht, Thomas J. Vogl, Simon S. Martin, John W. Nance, Taylor M. Duguay, Julian L. Wichmann, Carlo N. De Cecco, Akos Varga-Szemes, Marly van Assen, Christian Tesche, and U. Joseph Schoepf. Review of Clinical Applications for Virtual Monoenergetic Dual-Energy CT. *Radiology*, 293(2):260–271, November 2019.

[68] Negin Rassouli, Hamid Chalian, Prabhakar Rajiah, Amar Dhanantwari, and Luis Landeras. Assessment of 70-keV virtual monoenergetic spectral images in abdominal CT imaging: A com-

parison study to conventional polychromatic 120-kVp images. *Abdominal Radiology (New York)*, 42(10):2579–2586, October 2017.

[69] Moritz Kaup, Jan-Erik Scholtz, Alexander Engler, Moritz H. Albrecht, Ralf W. Bauer, J. Matthias Kerl, Martin Beeres, Thomas Lehnert, Thomas J. Vogl, and Julian L. Wichmann. Dual-Energy Computed Tomography Virtual Monoenergetic Imaging of Lung Cancer: Assessment of Optimal Energy Levels. *Journal of Computer Assisted Tomography*, 40(1):80–85, February 2016.

[70] Victor Neuhaus, Nils Große Hokamp, Nuran Abdullayev, Volker Maus, Christoph Kabbasch, Anastasios Mpotsaris, David Maintz, and Jan Borggrefe. Comparison of virtual monoenergetic and polyenergetic images reconstructed from dual-layer detector CT angiography of the head and neck. *European Radiology*, 28(3):1102–1110, March 2018.

[71] Suyon Chang, Jin Hur, Dong Jin Im, Young Joo Suh, Yoo Jin Hong, Hye-Jeong Lee, Young Jin Kim, and Byoung Wook Choi. Dual-energy CT-based iodine quantification for differentiating pulmonary artery sarcoma from pulmonary thromboembolism: a pilot study. *European Radiology*, 26(9):3162–3170, September 2016.

[72] Gert Jan Pelgrim, Robbert W. van Hamersvelt, Martin J. Willemink, Bernhard T. Schmidt, Thomas Flohr, Arnold Schilham, Julien Milles, Matthijs Oudkerk, Tim Leiner, and Rozemarijn Vliegenthart. Accuracy of iodine quantification using dual energy CT in latest generation dual source and dual layer CT. *European Radiology*, 27(9):3904–3912, September 2017.

[73] Wei-Qiang Yan, Yong-Kang Xin, Yong Jing, Gang-Feng Li, Shu-Mei Wang, Wei-Cheng Rong, Gang Xiao, Xue-Bin Lei, Bo Li, Yu-Chuan Hu, and Guang-Bin Cui. Iodine Quantification Using Dual-Energy Computed Tomography for Differentiating Thymic Tumors. *Journal of Computer Assisted Tomography*, 42(6):873–880, 2018.

[74] Stefania Rizzo, Davide Radice, Marco Femia, Paolo De Marco, Daniela Origgi, Lorenzo Preda, Massimo Barberis, Raffaella Vigorito, Giovanni Mauri, Alberto Mauro, and Massimo Bellomi. Metastatic and non-metastatic lymph nodes: quantification and different distribution of iodine uptake assessed by dual-energy CT. *European Radiology*, 28(2):760–769, February 2018.

[75] Achille Mileto, Daniele Marin, Juan Carlos Ramirez-Giraldo, Emanuele Scribano, Bernhard Krauss, Silvio Mazziotti, and Giorgio Ascenti. Accuracy of Contrast-Enhanced Dual-Energy MDCT for the Assessment of Iodine Uptake in Renal Lesions. *American Journal of Roentgenology*, 202(5):W466–W474, May 2014. Publisher: American Roentgen Ray Society.

[76] Daniele Marin, Drew Davis, Kingshuk Roy Choudhury, Bhavik Patel, Rajan T. Gupta, Achille Mileto, and Rendon C. Nelson. Characterization of Small Focal Renal Lesions: Diagnostic Accuracy with Single-Phase Contrast-enhanced Dual-Energy CT with Material Attenuation Analysis Compared with Conventional Attenuation Measurements. *Radiology*, 284(3):737–747, September 2017.

[77] Simon S. Martin, Sebastian Weidinger, Rouben Czwikla, Benjamin Kaltenbach, Moritz H. Albrecht, Lukas Lenga, Thomas J. Vogl, and Julian L. Wichmann. Iodine and Fat Quantification for Differentiation of Adrenal Gland Adenomas From Metastases Using Third-Generation Dual-Source Dual-Energy Computed Tomography. *Investigative Radiology*, 53(3):173–178, March 2018.

[78] Megan C. Jacobsen, Dawid Schellingerhout, Cayla A. Wood, Eric P. Tamm, Myrna C. Godoy, Jia Sun, and Dianna D. Cody. Intermanufacturer Comparison of Dual-Energy CT Iodine Quantification and Monochromatic Attenuation: A Phantom Study. *Radiology*, 287(1):224–234, April 2018. Publisher: Radiological Society of North America.

[79] André Euler, Justin Solomon, Maciej A. Mazurowski, Ehsan Samei, and Rendon C. Nelson. How accurate and precise are CT based measurements of iodine concentration? A comparison of the minimum detectable concentration difference among single source and dual source dual energy CT in a phantom study. *European Radiology*, 29(4):2069–2078, April 2019.

[80] Andreas P. Sauter, Felix K. Kopp, Daniela Münzel, Julia Dangelmaier, Martin Renz, Bernhard Renger, Rickmer Braren, Alexander A. Fingerle, Ernst J. Rummeny, and Peter B. Noël. Accuracy of iodine quantification in dual-layer spectral CT: Influence of iterative reconstruction, patient habitus and tube parameters. *European Journal of Radiology*, 102:83–88, May 2018.

[81] Vanja Harsaker, Kristin Jensen, Hilde Kjernlie Andersen, and Anne Catrine Martinsen. Quantitative benchmarking of iodine imaging for two CT spectral imaging technologies: a phantom study. *European Radiology Experimental*, 5(1):24, June 2021.

[82] Sebastian Feuerlein, Tobias J. Heye, Mustafa R. Bashir, and Daniel T. Boll. Iodine quantification using dual-energy multidetector computed tomography imaging: phantom study assessing the impact of iterative reconstruction schemes and patient habitus on accuracy. *Investigative Radiology*, 47(11):656–661, November 2012.

[83] Thomas Sartoretti, Anna Landsmann, Dominik Nakhostin, Matthias Eberhard, Christian Roeren, Victor Mergen, Kai Higashigaito, Rainer Raupach, Hatem Alkadhi, and André Euler. Quantum Iterative Reconstruction for Abdominal Photon-counting Detector CT Improves

Image Quality. *Radiology*, 303(2):339–348, May 2022. Publisher: Radiological Society of North America.

[84] Mats Danielsson, Mats Persson, and Martin Sjölin. Photon-counting x-ray detectors for CT. *Physics in Medicine &amp$\mathsemicolon$ Biology*, 66(3):03TR01, January 2021. Publisher: IOP Publishing.

[85] Salim Si-Mohamed, Daniel Bar-Ness, Monica Sigovan, Valérie Tatard-Leitman, David P. Cormode, Pratap C. Naha, Philippe Coulon, Lucie Rascle, Ewald Roessl, Michal Rokni, Ami Altman, Yoad Yagil, Loic Boussel, and Philippe Douek. Multicolour imaging with spectral photon-counting CT: a phantom study. *European Radiology Experimental*, 2(1):34, October 2018.

[86] Ashley Tao, Richard Huang, Shengzhen Tao, Gregory J Michalak, Cynthia H McCollough, and Shuai Leng. Dual-source photon counting detector CT with a tin filter: a phantom study on iodine quantification performance. *Physics in medicine and biology*, 64(11):115019, May 2019.

[87] Faraz Farhadi, Jayasai R. Rajagopal, Moozhan Nikpanah, Pooyan Sahbaee, Ashkan A. Malayeri, William F. Pritchard, Ehsan Samei, Elizabeth C. Jones, and Marcus Y. Chen. Review of Technical Advancements and Clinical Applications of Photon-counting Computed Tomography in Imaging of the Thorax. *Journal of Thoracic Imaging*, 36(2):84–94, March 2021.

[88] Kishore Rajendran, Martin Petersilka, André Henning, Elisabeth R. Shanblatt, Bernhard Schmidt, Thomas G. Flohr, Andrea Ferrero, Francis Baffour, Felix E. Diehn, Lifeng Yu, Prabhakar Rajiah, Joel G. Fletcher, Shuai Leng, and Cynthia H. McCollough. First Clinical Photon-counting Detector CT System: Technical Evaluation. *Radiology*, 303(1):130–138, April 2022. Publisher: Radiological Society of North America.

[89] Ronald Booij, Niels R. van der Werf, Marcel L. Dijkshoorn, Aad van der Lugt, and Marcel van Straten. Assessment of Iodine Contrast-To-Noise Ratio in Virtual Monoenergetic Images Reconstructed from Dual-Source Energy-Integrating CT and Photon-Counting CT Data. *Diagnostics*, 12(6):1467, June 2022. Number: 6 Publisher: Multidisciplinary Digital Publishing Institute.

[90] Thomas Sartoretti, Victor Mergen, Lisa Jungblut, Hatem Alkadhi, and André Euler. Liver Iodine Quantification With Photon-Counting Detector CT: Accuracy in an Abdominal Phantom and Feasibility in Patients. *Academic Radiology*, May 2022.

[91] Josua A. Decker, Stefanie Bette, Nora Lubina, Katharina Rippel, Franziska Braun, Franka Risch, Piotr Woźnicki, Claudia Wollny, Christian Scheurig-Muenkler, Thomas J. Kroencke, and Florian

Schwarz. Low-dose CT of the abdomen: Initial experience on a novel photon-counting detector CT and comparison with energy-integrating detector CT. *European Journal of Radiology*, 148:110181, March 2022.

[92] Leening P. Liu, Nadav Shapira, Pooyan Sahbaee, Mitchell Schnall, Harold I. Litt, and Peter B. Noël. First-generation clinical dual-source photon-counting CT: ultra-low dose quantitative spectral imaging. Technical report, medRxiv, December 2021. Type: article.

[93] Ralf Gutjahr, Ahmed F. Halaweish, Zhicong Yu, Shuai Leng, Lifeng Yu, Zhoubo Li, Steven M. Jorgensen, Erik L. Ritman, Steffen Kappler, and Cynthia H. McCollough. Human imaging with photon-counting-based CT at clinical dose levels: Contrast-to-noise ratio and cadaver studies. *Investigative radiology*, 51(7):421–429, July 2016.

[94] S. Sawall, L. Klein, E. Wehrse, L. T. Rotkopf, C. Amato, J. Maier, H.-P. Schlemmer, C. H. Ziener, S. Heinze, and M. Kachelrieß. Threshold-dependent iodine imaging and spectral separation in a whole-body photon-counting CT system. *European Radiology*, 31(9):6631–6639, September 2021.

[95] Leening P. Liu, Nadav Shapira, Andrew A. Chen, Russell T. Shinohara, Pooyan Sahbaee, Mitchell Schnall, Harold I. Litt, and Peter B. Noël. First-generation clinical dual-source photon-counting CT: ultra-low-dose quantitative spectral imaging. *European Radiology*, 32(12):8579–8587, December 2022.

[96] James D. Koonce, Rozemarijn Vliegenthart, U. Joseph Schoepf, Bernhard Schmidt, Amy E. Wahlquist, Paul J. Nietert, Gorka Bastarrika, Thomas G. Flohr, and Felix G. Meinel. Accuracy of dual-energy computed tomography for the measurement of iodine concentration using cardiac CT protocols: validation in a phantom model. *European Radiology*, 24(2):512–518, February 2014.

[97] Mridul Bhattarai, Steve Bache, Ehsan Abadi, and Ehsan Samei. A systematic task-based image quality assessment of photon-counting and energy integrating CT as a function of reconstruction kernel and phantom size. *Medical Physics*, n/a(n/a). _eprint: https://onlinelibrary.wiley.com/doi/pdf/10.1002/mp.16619.

[98] R. C. Chen, R. Longo, L. Rigon, F. Zanconati, A. De Pellegrin, F. Arfelli, D. Dreossi, R.-H. Menk, E. Vallazza, T. Q. Xiao, and E. Castelli. Measurement of the linear attenuation coefficients of breast tissues by synchrotron radiation computed tomography. *Physics in Medicine & Biology*, 55(17):4993, August 2010.

[99] Erik Fredenberg, Paula Willsher, Elin Moa, David R. Dance, Kenneth C. Young, and Matthew G. Wallis. Measurement of breast-tissue x-ray attenuation by spectral imaging: fresh and fixed

normal and malignant tissue. *Physics in Medicine & Biology*, 63(23):235003, November 2018. Publisher: IOP Publishing.

[100] Willi A. Kalender, Daniel Kolditz, Christian Steiding, Veikko Ruth, Ferdinand Lück, Ann-Christin Rößler, and Evelyn Wenkel. Technical feasibility proof for high-resolution low-dose photon-counting CT of the breast. *European Radiology*, 27(3):1081–1086, March 2017.

[101] Nicole Berger, Magda Marcon, Natalia Saltybaeva, Willi A. Kalender, Hatem Alkadhi, Thomas Frauenfelder, and Andreas Boss. Dedicated Breast Computed Tomography With a Photon-Counting Detector: Initial Results of Clinical In Vivo Imaging. *Investigative Radiology*, 54(7):409–418, July 2019. Number: 7 Publisher: Lippincott Williams & Wilkins.

[102] Caroline Zellweger, Nicole Berger, Jann Wieler, Dania Cioni, Emanuele Neri, Andreas Boss, Thomas Frauenfelder, and Magda Marcon. Breast Computed Tomography: Diagnostic Performance of the Maximum Intensity Projection Reformations as a Stand-Alone Method for the Detection and Characterization of Breast Findings. *Investigative Radiology*, 57(4):205–211, April 2022.

[103] Cynthia Sabrina Schmidt, Caroline Zellweger, Jann Wieler, Nicole Berger, Magda Marcon, Thomas Frauenfelder, and Andreas Boss. Clinical assessment of image quality, usability and patient comfort in dedicated spiral breast computed tomography. *Clinical Imaging*, 90:50–58, October 2022. Publisher: Elsevier.

[104] R. Longo, F. Arfelli, R. Bellazzini, U. Bottigli, A. Brez, F. Brun, A. Brunetti, P. Delogu, F. Di Lillo, D. Dreossi, V. Fanti, C. Fedon, B. Golosio, N. Lanconelli, G. Mettivier, M. Minuti, P. Oliva, M. Pinchera, L. Rigon, P. Russo, A. Sarno, G. Spandre, G. Tromba, and F. Zanconati. Towards breast tomography with synchrotron radiation at Elettra: first images. *Physics in Medicine and Biology*, 61(4):1634–1649, February 2016. Publisher: IOP Publishing.

[105] Renata Longo, Fulvia Arfelli, Deborah Bonazza, Ubaldo Bottigli, Luca Brombal, Adriano Contillo, Maria A. Cova, Pasquale Delogu, Francesca Di Lillo, Vittorio Di Trapani, Sandro Donato, Diego Dreossi, Viviana Fanti, Christian Fedon, Bruno Golosio, Giovanni Mettivier, Piernicola Oliva, Serena Pacilè, Antonio Sarno, Luigi Rigon, Paolo Russo, Angelo Taibi, Maura Tonutti, Fabrizio Zanconati, and Giuliana Tromba. Advancements towards the implementation of clinical phase-contrast breast computed tomography at Elettra. *Journal of Synchrotron Radiation*, 26(Pt 4):1343–1353, July 2019.

[106] L. A. Lehmann, R. E. Alvarez, A. Macovski, W. R. Brody, N. J. Pelc, S. J. Riederer, and A. L. Hall. Generalized image combinations in dual KVP digital radiography. *Medical Physics*, 8(5):659–667, 1981. _eprint: https://onlinelibrary.wiley.com/doi/pdf/10.1118/1.595025.

[107] Cynthia H. McCollough, Shuai Leng, Lifeng Yu, and Joel G. Fletcher. Dual- and Multi-Energy CT: Principles, Technical Approaches, and Clinical Applications. *Radiology*, 276(3):637–653, September 2015. Publisher: Radiological Society of North America.

[108] Kishore Rajendran, Martin Petersilka, André Henning, Elisabeth R. Shanblatt, Bernhard Schmidt, Thomas G. Flohr, Andrea Ferrero, Francis Baffour, Felix E. Diehn, Lifeng Yu, Prabhakar Rajiah, Joel G. Fletcher, Shuai Leng, and Cynthia H. McCollough. First Clinical Photon-counting Detector CT System: Technical Evaluation. *Radiology*, 303(1):130–138, December 2021.

[109] Prabhakar Rajiah, Anushri Parakh, Fernando Kay, Dhiraj Baruah, Avinash R. Kambadakone, and Shuai Leng. Update on Multienergy CT: Physics, Principles, and Applications. *RadioGraphics*, 40(5):1284–1308, September 2020. Publisher: Radiological Society of North America.

[110] Xue Dong, Tianye Niu, and Lei Zhu. Combined iterative reconstruction and image-domain decomposition for dual energy CT using total-variation regularization. *Medical Physics*, 41(5):051909, 2014. _eprint: https://onlinelibrary.wiley.com/doi/pdf/10.1118/1.4870375.

[111] Korbinian Mechlem, Sebastian Allner, Kai Mei, Franz Pfeiffer, and Peter B. Noël. Dictionary-based image denoising for dual energy computed tomography. page 97830E, San Diego, California, United States, March 2016.

[112] Anna Piai, Adriano Contillo, Fulvia Arfelli, Deborah Bonazza, Luca Brombal, Maria Assunta Cova, Pasquale Delogu, Vittorio Di Trapani, Sandro Donato, Bruno Golosio, Giovanni Mettivier, Piernicola Oliva, Luigi Rigon, Angelo Taibi, Maura Tonutti, Giuliana Tromba, Fabrizio Zanconati, and Renata Longo. Quantitative characterization of breast tissues with dedicated CT imaging. 64(15):155011, August 2019. Publisher: IOP Publishing.

[113] Wenkun Zhang, Hanming Zhang, Linyuan Wang, Xiaohui Wang, Ailong Cai, Lei Li, Tianye Niu, and Bin Yan. Image Domain Dual Material Decomposition for Dual-Energy CT using Butterfly Network. *Medical Physics*, 46(5):2037–2051, May 2019. Number: 5 arXiv: 1804.01685.

[114] R. Bellazzini, G. Spandre, A. Brez, M. Minuti, M. Pinchera, and P. Mozzo. Chromatic X-ray imaging with a fine pitch CdTe sensor coupled to a large area photon counting pixel ASIC. 8(02):C02028–C02028, February 2013. Publisher: IOP Publishing.

[115] P. Delogu, P. Oliva, R. Bellazzini, A. Brez, P. L. de Ruvo, M. Minuti, M. Pinchera, G. Spandre, and A. Vincenzi. Characterization of Pixirad-1 photon counting detector for X-ray imaging. 11(01):P01015–P01015, January 2016. Publisher: IOP Publishing.

[116] L. Brombal, S. Donato, F. Brun, P. Delogu, V. Fanti, P. Oliva, L. Rigon, V. Di Trapani, R. Longo, and B. Golosio. Large-area single-photon-counting CdTe detector for synchrotron radiation computed tomography: a dedicated pre-processing procedure. *Journal of Synchrotron Radiation*, 25(4):1068–1077, July 2018. Number: 4 Publisher: International Union of Crystallography.

[117] Francesco Brun, Lorenzo Massimi, Michela Fratini, Diego Dreossi, Fulvio Billè, Agostino Accardo, Roberto Pugliese, and Alessia Cedola. SYRMEP Tomo Project: a graphical user interface for customizing CT reconstruction workflows. *Advanced Structural and Chemical Imaging*, 3, January 2017.

[118] Adriano Contillo, Anna Veronese, Luca Brombal, Sandro Donato, Luigi Rigon, Angelo Taibi, Giuliana Tromba, Renata Longo, and Fulvia Arfelli. A Proposal for a Quality Control Protocol in Breast CT with Synchrotron Radiation. *Radiology and Oncology*, 52(3):329–336, March 2018.

[119] Sandro Donato, Luca Brombal, Lucia Mariel Arana Pena, Fulvia Arfelli, Adriano Contillo, Pasquale Delogu, Francesca Di Lillo, Vittorio Di Trapani, Viviana Fanti, Renata Longo, Piernicola Oliva, Luigi Rigon, Luisella Stori, Giuliana Tromba, and Bruno Golosio. Optimization of a customized simultaneous algebraic reconstruction technique algorithm for phase-contrast breast computed tomography. *Physics in Medicine &amp$\mathsemicolon$ Biology*, April 2022. Publisher: IOP Publishing.

[120] C. Fedon, F. Longo, G. Mettivier, and R. Longo. GEANT4 for breast dosimetry: parameters optimization study. 60(16):N311–N323, August 2015. Publisher: IOP Publishing.

[121] G. Mettivier, C. Fedon, F. Di Lillo, R. Longo, A. Sarno, G. Tromba, and P. Russo. Glandular dose in breast computed tomography with synchrotron radiation. *Physics in Medicine and Biology*, 61(2):569–587, January 2016.

[122] Peter J. Rousseeuw. Silhouettes: A graphical aid to the interpretation and validation of cluster analysis. *Journal of Computational and Applied Mathematics*, 20:53–65, November 1987.

[123] Seyedamir Tavakoli Taba, Benedicta D. Arhatari, Yakov I. Nesterets, Ziba Gadomkar, Sheridan C. Mayo, Darren Thompson, Jane Fox, Beena Kumar, Zdenka Prodanovic, Daniel Hausermann, Anton Maksimenko, Christopher Hall, Matthew Dimmock, Konstantin M. Pavlov, Darren Lockie, Masoumeh Gity, Andrew Peele, Harry M. Quiney, Sarah Lewis, Timur E. Gureyev, and

Patrick C. Brennan. Propagation-Based Phase-Contrast CT of the Breast Demonstrates Higher Quality Than Conventional Absorption-Based CT Even at Lower Radiation Dose. *Academic Radiology*, 28(1):e20–e26, January 2021.

[124] Arthur Lalonde and Hugo Bouchard. A general method to derive tissue parameters for Monte Carlo dose calculation with multi-energy CT. *Physics in Medicine and Biology*, 61(22):8044–8069, October 2016. Publisher: IOP Publishing.

[125] Doniyor Jumanazarov, Ja-Keoung Koo, Henning F. Poulsen, Ulrik L. Olsen, and Mihai Iovea. The significance of the spectral correction of photon counting detector response in material classification from spectral x-ray CT. In Ivan Prochazka, Roman Sobolewski, Martin Štefaňák, and Aurél Gábris, editors, *Quantum Optics and Photon Counting 2021*, page 15, Online Only, Czech Republic, April 2021. SPIE.

[126] Kuan-Hao Su, Jung-Wen Kuo, David W. Jordan, Steven Van Hedent, Paul Klahr, Zhouping Wei, Rose Al Helo, Fan Liang, Pengjiang Qian, Gisele C. Pereira, Negin Rassouli, Robert C. Gilkeson, Bryan J. Traughber, Chee-Wai Cheng, and Raymond F. Muzic. Machine learning-based dual-energy CT parametric mapping. *Physics in Medicine &amp$\mathsemicolon$ Biology*, 63(12):125001, June 2018. Publisher: IOP Publishing.

[127] Karl Berggren, Mikael Eriksson, Per Hall, Matthew G. Wallis, and Erik Fredenberg. In vivo measurement of the effective atomic number of breast skin using spectral mammography. *Physics in Medicine & Biology*, 63(21):215023, October 2018. Publisher: IOP Publishing.

[128] Michel S. S. Gobo, L. D. H. Soares, and M. E. Poletti. Effective atomic number of breast tissues determined by transmission and scattering methods. *Radiation Physics and Chemistry*, 167:108260, February 2020.

[129] M. Antoniassi, A. L. C. Conceiccão, and M. E. Poletti. Study of effective atomic number of breast tissues determined using the elastic to inelastic scattering ratio. *Nuclear Instruments and Methods in Physics Research Section A: Accelerators, Spectrometers, Detectors and Associated Equipment*, 652(1):739–743, October 2011.

[130] C. Tomasi and R. Manduchi. Bilateral filtering for gray and color images. In *Sixth International Conference on Computer Vision (IEEE Cat. No.98CH36271)*, pages 839–846, January 1998.